

---

Theses and Dissertations

---

2015

# Computational methods to model disease and genetic effects on optic nerve head structure

Mark Allen Christopher  
*University of Iowa*

Copyright 2015 Mark Allen Christopher

This dissertation is available at Iowa Research Online: <http://ir.uiowa.edu/etd/1959>

---

## Recommended Citation

Christopher, Mark Allen. "Computational methods to model disease and genetic effects on optic nerve head structure." PhD (Doctor of Philosophy) thesis, University of Iowa, 2015.  
<http://ir.uiowa.edu/etd/1959>.

---

Follow this and additional works at: <http://ir.uiowa.edu/etd>



Part of the [Biomedical Engineering and Bioengineering Commons](#)

COMPUTATIONAL METHODS TO MODEL DISEASE AND GENETIC EFFECTS  
ON OPTIC NERVE HEAD STRUCTURE

by  
Mark Allen Christopher

A thesis submitted in partial fulfillment  
of the requirements for the Doctor of  
Philosophy degree in Biomedical Engineering  
in the Graduate College of  
The University of Iowa

December 2015

Thesis Supervisors: Professor Michael D. Abramoff

Associate Professor Todd E. Scheetz

Copyright by  
MARK ALLEN CHRISTOPHER  
2015  
All Rights Reserved

Graduate College  
The University of Iowa  
Iowa City, Iowa

CERTIFICATE OF APPROVAL

---

PH.D. THESIS

---

This is to certify that the Ph.D. thesis of

Mark Allen Christopher

has been approved by the Examining Committee  
for the thesis requirement for the Doctor of Philosophy  
degree in Biomedical Engineering at the December 2015 graduation.

Thesis Committee: \_\_\_\_\_  
Michael D. Abramoff, Thesis Supervisor

\_\_\_\_\_  
Todd E. Scheetz, Thesis Supervisor

\_\_\_\_\_  
John H. Fingert

\_\_\_\_\_  
Mona K. Garvin

\_\_\_\_\_  
Joseph M. Reinhardt

## ACKNOWLEDGMENTS

I would first like to thank my advisors Dr. Todd Scheetz and Dr. Michael Abramoff for their mentorship throughout my time as an undergraduate and graduate student. I'd also like to thank everyone involved in the Scheetz Lab, WIVR, and CBCB for providing the environment I've needed to develop as a scientist. Finally, I'd like to thank Bhavna Antony. Her help in revising this thesis, discussions and suggestions for all of my projects, and the support she's provided over the years have been invaluable.

## ABSTRACT

Glaucoma is a leading cause of blindness throughout the world and is estimated to affect 80 million by 2020. This disease causes progressive loss of vision and, left untreated, can lead to complete blindness. With treatment, however, disease progression can be slowed dramatically. This makes early detection and intervention crucial in preserving the vision of affected individuals.

Onset and progression of glaucoma are associated with structural changes to an anatomical feature known as the optic nerve head (ONH). The ONH is the site of attachment between the retina and the optic nerve that carries all visual information to the brain. As glaucoma progresses, characteristic changes related to cell death and loss of vision can be observed in the three-dimensional structure of the ONH. A common modality used to observe these changes is stereo fundus imaging. This modality captures three-dimensional information via stereo imaging and is commonly used in clinical settings to diagnose and monitor glaucoma. A limitation of using stereo fundus images is the need for review by glaucoma specialists to identify disease related features of ONH structure. Further, even when expert evaluation is possible, the subjective nature of the process can lead due large discrepancies in the evaluations and resultant clinical decisions. The work presented here seeks address these concerns by providing automated, computational tools that can be used to characterize ONH structure.

Specifically, this thesis outlines the development of computational methods for inferring three-dimensional information from stereo fundus images and identifying objective, quantitative measurements of ONH structure. The resulting computational tools were applied to image and clinical data collected from a large cohort of individuals to identify hidden relationships between ONH structure, clinical measurements, and glaucoma. These tools were then applied to develop methods for estimating the impact of individual genetic factors on the ONH. Finally, using a longitudinal dataset collected over

more than a decade, computational analysis was used to investigate how ONH structure changes over time in response to aging, other disease-related factors, and glaucoma progression.

## PUBLIC ABSTRACT

Early detection is a crucial aspect of care in the treatment of glaucoma. This progressive disease causes irreversible loss of vision and can lead to complete blindness. However, with early intervention, disease progression can be dramatically slowed and vision can be retained. This work presents data-driven methods to identify structural changes associated with glaucoma and aid in early detection of the disease.

The focus of the methods presented here is to analyze the three-dimensional shape of an anatomical structure known as the optic nerve head (ONH). The ONH is the attachment site of the optic nerve to the retina with a characteristic shape that often undergoes changes during the development and progression of glaucoma. Observation of the ONH is a standard part of clinical assessments for glaucoma. By applying statistical and computational techniques to a large dataset of medical images and clinical measurements, biologically and clinically important features of ONH structure were identified.

Specifically, methods for quantifying ONH structure based on medical images were developed and the resulting measurements were found to significantly increase accuracy in predicting development of glaucoma. Further methods that incorporated genetic information were developed and used to identify significant relationships between ONH shape and genetics. Finally, longitudinal data captured over several years was analyzed to identify time-dependent ONH changes associated with disease.



## TABLE OF CONTENTS

LIST OF TABLES .....	viii
LIST OF FIGURES .....	ix
CHAPTER	
1. INTRODUCTION .....	1
2. BACKGROUND .....	4
Primary Open Angle Glaucoma.....	4
Optic Nerve Head Structure.....	6
Statistical Shape Modeling of Retinal Structure.....	10
Genetic Associations with POAG .....	14
3. FUNDUS IMAGE PROCESSING.....	18
Optic Nerve Head Localization .....	19
Algorithm Description.....	19
Algorithm Evaluation .....	22
Depth Inference .....	23
Algorithm Description.....	28
Algorithm Evaluation .....	31
Conclusion .....	34
4. ANALYSIS OF BASELINE ONH STRUCTURE .....	36
Dataset Description.....	36
Structural Endophenotype Identification.....	39
Fundus Processing .....	41
Depth Processing .....	42
Feature Identification.....	42
Structural Endophenotype Evaluation .....	45
Clinical Measurement Associations .....	45
Disease Prediction .....	47
Comparison to Expert ONH Review .....	50
Conclusion .....	52
5. DISCOVERY OF GENETIC ASSOCIATIONS WITH BASELINE ONH STRUCTURE .....	59
Dataset Description.....	60
Genetic Contributions of Known Glaucoma Polymorphisms .....	60
Known Glaucoma Polymorphism Identification.....	61
Structural Endophenotype Identification.....	63
Genetic Feature Estimation .....	63
Genetic Feature Evaluation .....	65
Genome-Wide Structural Endophenotype Associations .....	65
Preprocessing and Quality Control.....	68

Structural Endophenotype Association Testing .....	68
Conclusions.....	69
6.    LONGITUDINAL ANALYSIS OF ONH STRUCTURE .....	74
Dataset Description.....	75
Longitudinal Fundus Image Registration .....	76
Baseline Annotation and Image Preprocessing .....	76
Image Registration and Evaluation .....	77
Individual Depth Map Analysis.....	85
Depth Inference and Structural Endophenotype Identification .....	86
Clinical Measurement Prediction .....	86
Longitudinal Changes to Structural Endophenotypes .....	87
Longitudinal Measurement Preprocessing .....	89
Longitudinal Features in Disease Detection.....	90
Longitudinal Features in Disease Prediction.....	94
Conclusions.....	96
7.    CONCLUSION.....	98
REFERENCES .....	102

## LIST OF TABLES

### Table

4.1	Summary of baseline data and POAG outcomes for the OHTS cohort.....	39
4.2	Significant associations between OHTS baseline measurements and STEPs. ....	47
4.3	Summary of expert grading and comparisons to STEPs. ....	53
5.1	Set of SNPs previously associated with POAG.....	62
5.2	Significant associations between STEPs and SNPs from across the genome. ....	71
6.1	OHTS cohort demographics, longitudinal measurements, and disease status.....	75
6.2	The registration parameters and preprocessing steps that were evaluated. ....	80
6.3	Significant associations between longitudinal measurements and STEPs. ....	87

## LIST OF FIGURES

### Figure

2.1	<p><b>(A)</b> Cross-section of the human eye with the location of the ONH highlighted (inset). Illustration courtesy of National Eye Institute (<a href="https://nei.nih.gov/photo/">https://nei.nih.gov/photo/</a>). <b>(B)</b> The ONH as it appears in fundus images with the nasal (N), temporal (T), superior (S), and inferior (I) directions labeled. <b>(C)</b> A three-dimensional rendering of the ONH illustrating typical structure.....</p>	8
2.2	<p>Example of a healthy ONH and some common abnormalities. <b>(A)</b> A normal ONH region with the cup (blue circle) and disc (red circle) outlined. The ratio of the diameters of these circles corresponds to the CDR. <b>(B)</b> An ONH region exhibiting localized thinning (notching) in the superior quadrant (blue arrow). <b>(C)</b> An example of peripapillary atrophy altering the pigment around the ONH (red arrow).....</p>	9
3.1	<p>The segmented window overlaid onto an example fundus image. This window was used to compute features at each pixel location. Features were computed based on each quadrant (I – IV) individually as well as the entire window. ....</p>	20
3.2	<p>The set of PCA-derived filters that were used to augment optic disc predictive features. Each of these filters was applied at three different scales to compute features used to estimate ONH location. ....</p>	22
3.3	<p>An example input image is shown along with images illustrating the selected features used in the automated ONH localization method. The features are shown in the order that they were chosen in during greedy forward feature selection. ....</p>	24
3.4	<p>The effect varying the number of nearest neighbors, <math>k</math>, on model performance. The lowest observed error was achieved by setting <math>k</math> equal to 11. ....</p>	25
3.5	<p>The ONH localization model applied to example fundus images. The input images (left) are shown along model output (right). Final point estimations (blue) and human annotated truth (red) is also shown.....</p>	26
3.6	<p>In stereo photography, the disparity (the difference between the position of a point in each image) is inversely proportional to the points three-dimensional depth. The scene points <math>P_1</math> and <math>P_2</math> differ only in depth (<math>d_1 &gt; d_2</math>). Dashed lines indicate the projection of each point onto the images <math>I_1</math> and <math>I_2</math>. Their disparities are given by <math>x_1</math> and <math>x_2</math>. Note that as depth decreases from <math>d_1</math> to <math>d_2</math>, the corresponding disparity increases from <math>x_1</math> to <math>x_2</math>. ....</p>	27
3.7	<p>The depth inference algorithm uses a multi-scale image representation. In this representation, the scale dimension extends from coarse (down-sampled, Gaussian-blurred) to fine (full resolution, un-blurred) images.....</p>	29

3.8	Depth inference is performed iteratively using multi-scale fundus image pairs (left) to generate depth estimates (right) at each scale. Depth computed at each scale is used as a starting point for the subsequent scale. ....	31
3.9	Example depth maps inferred from stereo (top) and renderings of the corresponding ONH structure (bottom).....	32
3.10	Comparisons of ONH region depth inferred from stereo fundus images to depth measured via OCT. ....	33
4.1	Example baseline stereo fundus images from the OHTS dataset. The format differences between different pairs are a result of the different camera types that were used. Despite quality assurance several possible sources of error can be observed with the images. These include over/under illumination, the presence of bright glare artifacts, and differences in focus within an image pair. ....	40
4.2	Illustration of the fundus and depth processing procedure. (A) Input stereo images. (B) The extracted ONH region stereo pair. (C) The raw depth map, the edge-cropped map, and the smoothed map. (D) Renderings of the ONH structure corresponding to the depth map.....	43
4.3	Gray-scale representation of the ten PCA-based STEPs used to model ONH structure shown with the percent of variance in depth data explained by each. Collectively, these features accounted for 95% of the variance observed.....	46
4.4	STEP features estimating the contribution of demographic and clinical variables to ONH structure. ....	48
4.5	Area under receiver operating characteristic curves for incident POAG prediction using combinations of demographic (age, sex, ethnicity), clinical (HCDR, VCDR, IOP, CCT, PSD, refraction), and STEP features.....	49
4.6	Variations to ONH structure capture by STEPs. (A) Gray-scale representations of the first five STEPs. (B) Illustration of the change to ONH structure induced by increasing the contribution of a single STEP. The median structure (left) is shown along with the median altered to exhibit an extreme value of the STEP. (C) The same figure shown as heat maps to indicate depth.....	51
5.1	STEP features identified using PCA applied to the genotyped subset of the OHTS cohort (n = 1054).....	64
5.2	Gray-scale representations of the estimated effect of 19 POAG-related SNPs on ONH structure. Each is shown along with the gene in which the SNPs occur. The * indicates the relationship between the estimated effect and SNP genotype is significant. ....	66
5.3	Summary of the associations between genetic ONH structural features and POAG. (A) The full list of identified genetic features associated with POAG. (B) The effect on ONH structure for some of the most significantly associated features. The gray-scale feature is along with the effect on structure that results from increasing the influence of the feature.....	67

5.4	Manhattan plots summarizing the genome-wide significance of three STEPs. The blue and red lines indicate suggestive and significant associations, respectively. Significant results are also highlighted in green.....	70
6.1	Example ONH extraction from longitudinally collected images. Each column illustrates the process for images collected from a single participant including the manually extracted ONH from the baseline (far left) and the automatically extracted ONH regions from follow-up images. The rows contain the input images (top), the ONH localization either through manual extract or probability maps generated automatically (middle), and the final extracted ONH (bottom). Note the vertical and horizontal translations associated with automated results and the change in image format resulting from different fundus cameras. ....	78
6.2	The image channels evaluated for use in registration. These included standard color channels (red, green, blue), a gray-scale channel (luminance), an average filtered channel (low pass), and a Gabor-based estimate of vasculature (vessel estimate). ....	83
6.3	Effect of the evaluated parameters on registration quality. Providing an initial estimate using automated ONH detection made the single largest impact. The similarity metric, image channel, and application of a threshold-based mask had more modest impacts on performance. Using a multi-scale registration and performing histogram matching had little impact on final registration quality. ....	84
6.4	An outline of the process used to register follow-up to baseline images. (A) A flowchart of the major processing steps. (B) The baseline (left) and follow-up (right) after each step with the target ONH location highlighted in blue. (C) A magnified view of the ONH region after each step. ....	85
6.5	Gray-scale representation of the ten PCA-based STEPs identified by analysis of the entire set of 18,657 baseline and follow-up images collected over the course of the OHTS. Collectively, these features accounted for 93.4% of the variance observed in the depth maps. ....	88
6.6	Longitudinal data collected from the OHTS cohort. Each graph shows 10 years of clinical (HCDR, IOP) or STEP measurements measured using stereo images. Each gray line represents the measurements collected from a single participant, blue lines indicate average measurements for normal participants, and red lines indicate the average of participants diagnosed with POAG based on expert review of stereo photos. ....	91
6.7	An illustration of time series alignment using dynamic time warping. (A) Without alignment, quantifying the similarity across time series data relies only on the comparing points captured at the same point in time and can be confounded by shifting or stretching one series with respect to another. (B) Alignment accounts for these differences by identifying similar regions across the series regardless of their position in time. ....	93
6.8	ROC curves resulting from time-series data to (A) detect progression to POAG using all longitudinal data and (B) predict POAG using only data collected prior to diagnosis. ....	95

## CHAPTER 1

### INTRODUCTION

Glaucoma is a leading cause of blindness, both in the U.S. and around the world. It is associated with death of retinal ganglion cells, optic nerve damage, and progressive loss of vision.[1] The most common form, primary open angle glaucoma (POAG), is a complex disease with numerous genetic contributors. Over the last few decades, several POAG-related genes have been discovered.[2] Despite this progress, much of the genetic basis of POAG remains unknown.[3]

A relatively recent approach for studying POAG and other complex diseases is to investigate the genetics of disease-related quantitative traits. The goal of this approach is to use the additional information added by quantitative phenotype measurements to identify previously hidden genetic contributions to disease. In the case of POAG, genome-wide association studies (GWAS) of traits such as intraocular pressure, central corneal thickness, and optic nerve head (ONH) structural measurements have been used with some success.[4, 5] In particular, studies using ONH structural measurements have not only strengthened evidence for genes previously associated with POAG, but have also suggested new lines of research by uncovering novel genetic associations.[4]

Using stereo fundus images, previous work has presented computational methods for the identification of ONH structural features.[6] These computationally-identified structural endophenotypes (STEPs) have been shown to capture heritable components of ONH structure and associate with POAG-related demographic variables.[6, 7] In this thesis, the use of STEP as quantitative measurements to characterize the variation observed ONH structure, estimate the impact of genetics, and predict disease onset prior to loss of vision will be evaluated.

This work is organized into the following six chapters based on topic. Chapter 2 will provide necessary context for POAG and its relationship to the ONH. An overview

of methods commonly used to analyze structural data collected from the eye is also presented. Finally, a summary of research into the genetics of POAG is provided.

Chapter 3 summarizes two important fundus processing algorithms presented in previous publications that were adapted and implemented for the research described here. The first is an algorithm for locating the ONH region within a fundus image. The second is the depth inference algorithm used to extract depth information from stereo fundus images. This important algorithm is the tool used to extract the dense, quantitative maps of ONH structure that are used for all other analyses.

Chapter 4 describes the analysis of a large participant cohort at risk for developing POAG. Using depth inferred from stereo fundus images, features that describe the types of variation observed within ONH structure were identified computationally. These features were compared to commonly used clinical measurements and evaluated based on their ability to predict future development of POAG. These features were also compared to qualitative evaluations of stereo fundus images performed by glaucoma specialists.

Chapter 5 describes an analysis that compares computationally identified ONH structural features to genetic data. Standard genetic association approaches are used to detect significant relationships between genetic factors and ONH structure. In addition to the standard approaches, a novel method for estimating the impact of individual genetic factors on ONH structure is presented and evaluated.

Chapter 6 describes the longitudinal analysis of ONH structure that was performed to identify time-dependent structural changes and evaluate their use in predicting POAG. The methods developed in previous chapters were applied to images collected over the course of several years from a large participant cohort to measure ONH structural features and quantify the changes occurring over time. Alternative methodologies for detecting and predicting POAG using these longitudinal features were developed and evaluated.



Finally, Chapter 7 contains a brief summary of the work presented here and comments on the research described here. This work closes by suggesting possible directions for future research.

## CHAPTER 2

### BACKGROUND

#### Primary Open Angle Glaucoma

Glaucoma is a degenerative disease of nerve tissue in the eye that is characterized by the progressive loss of retinal cells and damage to the optic nerve. Left untreated, this damage leads to irreversible vision loss and, often, complete blindness.[1] Glaucoma is a leading cause of blindness both in the U.S. and worldwide. It was estimated to effect 60 million people globally in 2010, with the number of affected estimated to rise to 80 million by 2020[8]. Glaucoma occurs in several different forms that include both acute and chronic types. The most common form, and the focus of this work, is primary open angle glaucoma (POAG). This is an adult-onset, chronic form of glaucoma that lacks secondary cause of disease. Currently, treatment options for POAG can drastically slow disease progression, but this requires early intervention to prevent loss of vision.

POAG and other forms of glaucoma have long been associated with elevated levels of intra-ocular pressure (IOP). IOP is a measurement of the fluid pressure of the aqueous and vitreous humor contained within the anterior and posterior portions of the eye, respectively. IOP is largely controlled by anterior eye structures that govern the inflow and outflow of aqueous humor. Blockage or breakdown of these structures as well as an increase blood pressure can cause IOP to rise. In addition, POAG has been associated with central corneal thickness (CCT), in which lower thicknesses are associated with an increasing the risk of disease.[9] Demographics also have an effect on POAG risk. While the effect of sex seems to be low, ethnicity can greatly affect POAG risk. Studies have found an increased risk of POAG as well as reduced CCT in individuals with African American ancestry compared with those of European ancestry.[10] Risk of POAG in individuals with East Asian ancestry seems to lower,

though, more recent work suggests this difference may not be as large as previously thought.[11]

Traditional models of glaucoma suggest that increased IOP exerts pressure on the retina causing physical damage to retinal cells and connective tissues. The result of this damage is loss of cells that are critical to visual function, especially retinal ganglion cells. These cells serve to process the visual signals originating from photoreceptor cells and pass on this signal for further processing in the visual cortex via the optic nerve. As retinal cell death occurs, corresponding functional damage also progresses. This typically manifests as areas of lost acuity within an individual's visual field. Often, this functional loss is first apparent in the periphery and can progress for long periods of times unnoticed by affected individuals. Because this loss of visual function is irreversible, early detection and treatment is critical so that damage can be prevented.[12]

Clinical assessment of POAG is performed using evaluation of multiple features related to visual function and structure. IOP is regularly measured during clinical visits and is used as a screening measurement to determine individuals who are at risk for POAG development. Commonly, a threshold value of ~22 mmHg is used to distinguish between individuals within the normal range and those with ocular hypertension.[13] Though the association between IOP and POAG has been confirmed in multiple populations across many years, it is far from a perfect predictor of disease.[1] Some estimates have indicated that individuals with IOP within the normal range can account for up to 50% of observed POAG cases.[14, 15] Similarly, elevated IOP does significantly increase the risk of POAG, but longitudinal studies have shown that a majority of people exhibiting elevated IOP at baseline still do not develop the disease within several years of follow up.[9]

Functional assessment of POAG is performed using perimetry in which the visual function across a large area of the retina can be evaluated. In these tests, a stimulus is repeatedly presented across multiple locations corresponding to a pre-defined region of the visual field. Generalized loss of function as well as characteristic patterns of loss in

standardized visual field testing are associated with disease progression.[16] The ability of perimetry to detect loss of function after damage has occurred makes it important in monitoring progression in POAG patients, but a poor choice for use in screening programs to detect the disease before vision loss occurs.

Structural measurements are also commonly used in clinical settings to diagnose and monitor POAG. Most commonly, inspection of the optic nerve head (ONH) is used to assess glaucomatous progression. The ONH is the site where the optic nerve connects to the retina and also serves as the opening through which retinal vasculature passes. All visual information traveling to the visual cortex from the retina passes through the ONH. The ONH has a characteristic three-dimensional structure that is, in part, determined by the axons passing through it. While the direction of causality remains uncertain, the loss of retinal cells and corresponding axons is associated with changes in the structure of the ONH. This makes structural evaluation of the ONH an important tool in detecting and tracking POAG.

### Optic Nerve Head Structure

Normative ONH structure can be described with reference to the optic disc that encompasses the entire ONH region and its subdivisions, the neuroretinal rim and cup regions. The rim and cup are so-called because the cup forms a concave shape separated from the plane of the nearby retinal surface, while the rim surrounds the cup and fills the remainder of the optic disc area.[17] A standardized coordinate system is used to describe quadrants of the circular ONH region including the superior, inferior, nasal, and temporal quadrants. In normal eyes, the cup region usually has a somewhat ovoid shape with a larger horizontal than vertical diameter though variation away from this rule of thumb is common.[16] Clinicians can view the ONH region directly through the use of specialized tools such as an ophthalmoscope or slit lamp. Images of the retina and ONH region can be captured using specialized fundus cameras. This includes both singular images of the

ONH region and stereo photography in which stereo image pairs are captured (see Chapter 3 for a more detailed discussion of stereo photography). Figure 2.1 provides an illustration of overall eye structure and the appearance of a normal ONH region visualized using fundus photography.

Qualitative assessment of the ONH structure by clinicians is a standard practice in screening for and tracking POAG. In this assessment, clinicians search for changes from normal ONH structure in the neuroretinal rim, cup, and the region surrounding the optic disc. See Figure 2.2 for examples of some of these POAG-associated changes. Typical ONH changes associated that are evaluated by clinicians include the following:

- Thinning of the neuroretinal rim - Thinning of the rim is associated with glaucomatous damage. It can occur over the entire rim (diffuse) or only affect isolated regions (notching).[16]
- Increased depth of the cup – Deepening of the cup is associated with loss of the neuroretinal rim and progression of POAG.[18]
- Steepening of the cup slope – Increases in the steepness of the sides of the cup are associated with larger cups and glaucomatous damage.[19]
- Increased optic disc size/area – Overall size of the disc area varies among different ethnic populations and affects evaluation of other ONH structural parameters.[20]
- Peripapillary atrophy – Visible changes to pigment in the region surrounding the ONH are caused by degradation of the retinal pigmented epithelium and occur at higher rates in POAG cases. Categorized as into mild (zone alpha) and severe forms (zone beta).[16]
- Changes to optic disc vasculature – POAG-associated structural changes to the rim and cup regions can cause changes to the position or angle of retinal vasculature. In some cases, hemorrhaging can occur in the ONH region.[16]

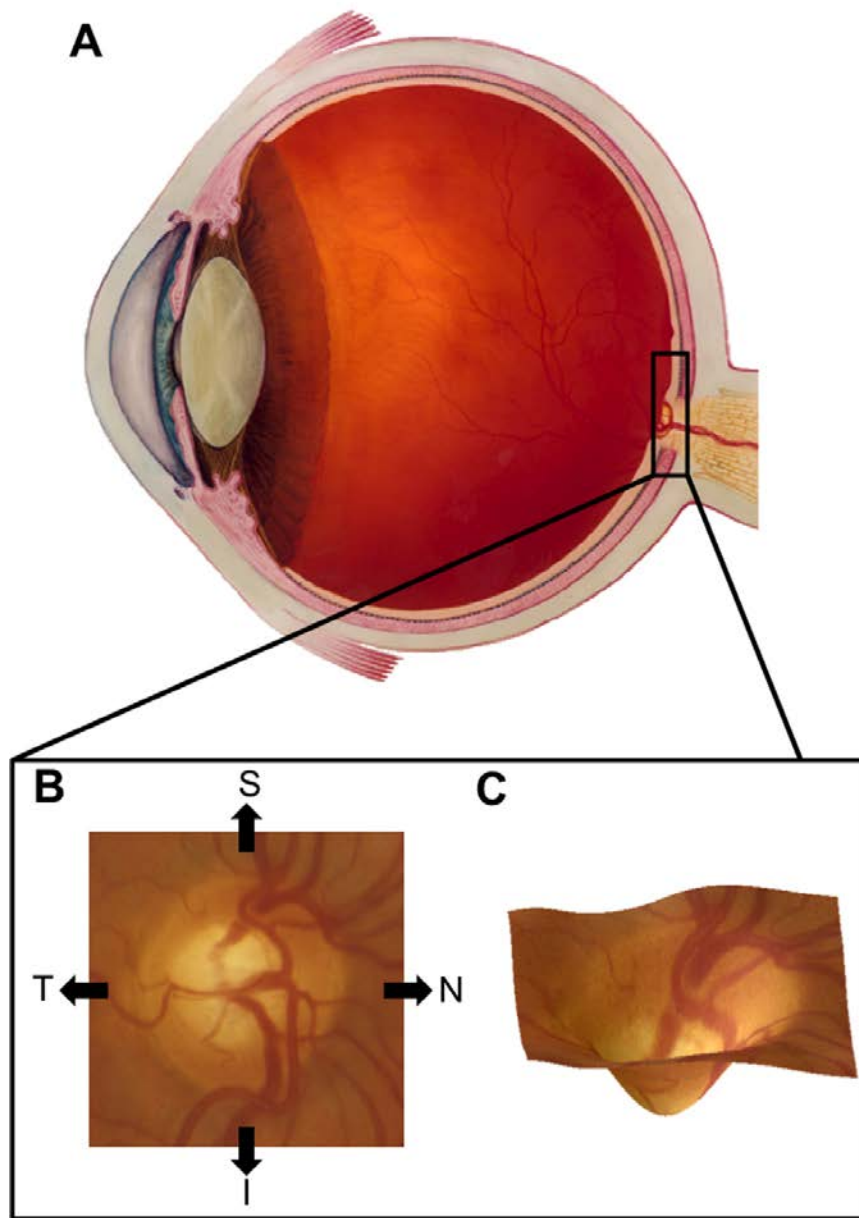


Figure 2.1: (A) Cross-section of the human eye with the location of the ONH highlighted (inset). Illustration courtesy of National Eye Institute (<https://nei.nih.gov/photo/>). (B) The ONH as it appears in fundus images with the nasal (N), temporal (T), superior (S), and inferior (I) directions labeled. (C) A three-dimensional rendering of the ONH illustrating typical structure.

ONH structure is also evaluated using quantitative structural parameters in clinical settings. Most commonly, cup-to-disc ratio (CDR) is used as the primary quantitative feature used to describe ONH structure. This measurement is the ratio of the cup diameter to the overall disc diameter. Its value rises when cup size increases and neuroretinal rim thinning occurs. Abundant evidence exists to show increases in CDR are associated with glaucomatous damage.[13, 21] CDR can be measured in the superior-inferior direction, termed vertical CDR (VCDR), or in the nasal-temporal direction, horizontal CDR (HCDR). Though several of the have shown significant associations with disease and are used in clinical evaluation of POAG, they are limited by measurement variability and the need for subjective evaluation. Determination of the presence/absence of disc features and the measured values of quantitative disc features can vary substantially between different observers and imaging set ups.[22-24]

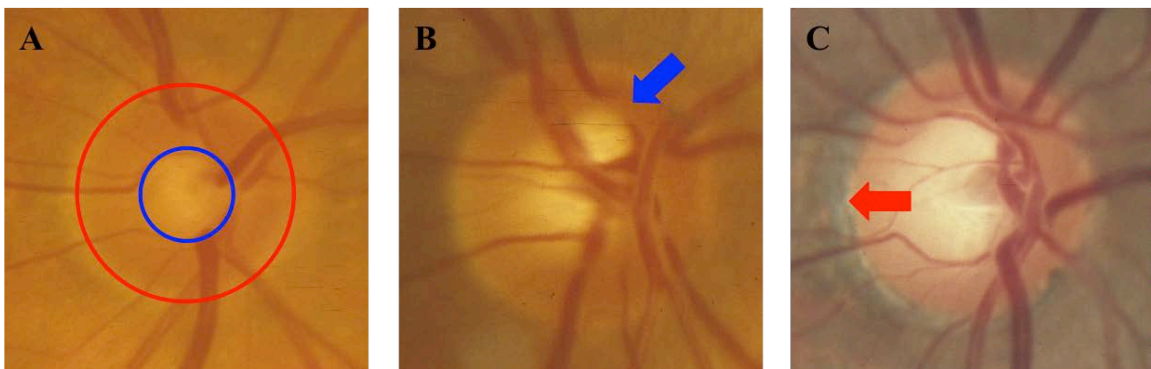


Figure 2.2: Example of a healthy ONH and some common abnormalities. (A) A normal ONH region with the cup (blue circle) and disc (red circle) outlined. The ratio of the diameters of these circles corresponds to the CDR. (B) An ONH region exhibiting localized thinning (notching) in the superior quadrant (blue arrow). (C) An example of peripapillary atrophy altering the pigment around the ONH (red arrow).

The ONH structural measurements mentioned above can be assessed either through direct observation of the retina or through examination of monocular and stereo

fundus images. One of the first technologies to allow direct depth measurement of the retinal surface was Heidelberg retinal tomography (HRT). This is an imaging technique based on a scanning laser that can be used to map the retinal surface structure. More recently, the imaging technology optical coherence tomography (OCT) has become an important tool in clinical and research settings. The rise of spectral-domain OCT within the past decade has allowed large amounts of structural image data to be captured from both normal and diseased individuals. Using this modality, both the retinal surface as well as deep structure of the retina can be interrogated. Of particular interest in glaucoma-related research is the ability of OCT to capture data from the retinal ganglion cell and nerve fiber layers and sub-surface structure of the ONH region. These deeper retinal structures are not available through traditional fundus imaging techniques. Measurements derived from OCT imaging and their use in aiding the detection and study of glaucoma have been widely published on.[25-28]

#### Statistical Shape Modeling of Retinal Structures

The analysis of biological forms has long been used by researchers to describe, evaluate, and classify organs and organisms. In traditional applications, this has involved the capture of physical measurements of biological forms. Depending on the structure under consideration, this has usually meant manual recording of length, area, or angle measurements. Reliance on a manual evaluation of structure has continued even with widespread use of high-resolution and three-dimensional imaging techniques. These techniques capture large amounts of structural data that can be lost by representing a complex structure using only a few manually measured parameters. For instance in the case of ONH structure, the commonly used metrics of CDR, cup depth, or disc area can easily fail to capture important structural markers of disease such as localized notching in the neuroretinal rim.



Within the field of ophthalmology, automated and semi-automated techniques have been developed to address the limitations of relying on manual evaluation of the ONH. Applied to fundus images, these computational techniques can be used to expedite and expand the process of capturing ONH parameters. This can include aiding or automating the process of segmenting the optic disc, rim, and cup. Once these regions are segmented, automated computation of total disc area, cup size, rim size, and CDR can be performed.[29-31] Other simple metrics such as measuring the similarity of the cup outline to a circle or oval been evaluated as well.[19, 32, 33]

While the data provided by OCT images provides the ability to describe deeper retinal structures, it is accompanied by increased complexity when visualizing and analyzing three-dimensional structural data. Numerous software tools have been developed to help both clinicians and researchers analyze retinal structure using OCT data. These include the proprietary software provided by the maker of OCT devices that produce reports highlighting areas of interest in the images and summary statistics describing structure. They also include tools developed by both clinical and computational researchers that can extract ONH structure from OCT images. Using the volumetric OCT scans, volumetric measurements of ONH structure such as rim and cup volume can be measured. Further, OCT allows examination of underlying anatomical structures and is commonly used to identify the boundaries between retinal layers and segment the retina into distinct layers related to biological function. The thicknesses of various layers identified using OCT have been evaluated and associated with several eye diseases.[34-36] One such layer, the retinal ganglion cell layer, has been used to produce estimates of the extent of ganglion cell loss. Overall thickness of this layer as well as localized thinning have been used to assess the extent of glaucomatous damage and evaluated as predictors for POAG.[37-39]

The relatively simple structural metrics that are currently used to measure ONH structure or ganglion cell layer thicknesses are associated with disease and have some

ability to predict conversion to POAG. These metrics are limited, though, because they reduce complex three-dimensional structures into a small set quantitative features meaning there is a substantial loss of structural information. Researchers have used these metrics not because they are particularly useful for representing the complex biological structures under consideration, but because these measurements can be interpreted based on prior knowledge. Many of these automated or semi-automated image-based metrics mimic standard clinical measurements (CDR, optic disc size, etc.) or at least seem to have a straightforward biological interpretation (e.g. thinning of the OCT layers indicating cell loss). While these metrics are certainly useful in detecting and, in some cases, predicting POAG, they can be limited in their ability to discover novel associations or motifs in the structures they measure.[40]

To address this limitation of the simple shape metrics, more sophisticated techniques inspired by mathematical and statistical modeling have been developed. One of the simplest techniques is to fit a curve to structural measurement data and to use the best-fit parameters represent shape. The general form of the curve (e.g. polynomial, spline, Gaussian) and number of parameters can be chosen based on the shapes and type of variability observed in the data. This technique requires human experts to decide on the type of curve that is used and, based on that choice, can lead to errors when observations vary greatly from the expected shape. Even so, this technique can be used to effectively represent shape even when applied to noisy data.[41] A more sophisticated class of techniques relies on the use of structural landmarks that indicate homologous points across the set observations. The location of each landmark in each observation is then determined (either through manual or automated detection). Differences between observations can be computed by comparing corresponding landmarks. The training of active shape models (ASM) rely on using landmarks in this way to iteratively estimate a template structure to which the observations are compared. After training, each observation is represented by its deviations from the template.[42] The final class of

techniques considered here makes use of frequency-based representations of structure. One example, elliptical Fourier analysis (EFA) fits a set of sinusoidal functions parameterized by frequency to structural observations. Similarly to standard Fourier analysis, each observation can be represented as a set of coefficients corresponding to contributions each frequency. The number of coefficients considered can be determined via reconstruction error or some application-specific metric.[40] Another commonly used frequency decomposition technique, the wavelet transform, has been applied to structural observations. Again in the wavelet case, frequency-dependent models are fit to observations to estimate the frequency contributions to structure. Additionally, spatial information is retained in the wavelet transform so that localized frequency contributions to structure can be quantified.[43]

Recently, researchers have applied these techniques to retinal and ONH structure and have typically evaluated model performance based on agreement with expert review of images or associations with disease. Sanfilippo *et al.*, for example, extracted shape measurements by manually tracing the rim and cup outlines from 30 individuals using stereoscopic fundus images.[44] Using landmarks sampled along these outlines, an ASM-like model was used to identify common modes of variation cup shape features were identified. The resulting features showed better accuracy in discriminating normal from POAG individuals than single measurements such as CDR. The requirement of manual fundus image evaluation by experts limited the sample sizes in this study, leaving the generalizability and power for early POAG prediction in question. Using the three-dimensional surface data provided by HRT, Zhu *et al.* learned the parameters needed to compute a shape score based on a wavelet representation of ONH structure.[45] This learned score outperformed standard clinical measurements in detecting POAG. Statistical shape modeling techniques are also being applied to deep retinal structure captured via OCT. Modeling of the overall structure of the retinal nerve fiber layer rather than relying solely on thickness measurements has increased in power to detect loss of

function in several studies.[46-48] Here, a common approach has been to model retinal nerve fibers as two-dimensional curves traveling across the retina. Features extracted from OCT data can be used to fit curve parameters which are then used to make predictions about structure or function. Shape modeling of the lamina cribrosa, a porous connective tissue structure underlying the ONH, has also revealed that EFA and other techniques can reveal features that may be associated with IOP and disease.[49-51] Application of statistical shape modeling techniques to retinal and ONH structure is relatively new within the literature, but has produced promising results. More conclusive results, though, may require analysis of larger participant cohorts for model training and longitudinal data to evaluate changes as POAG progresses within individuals.

#### Genetic Associations with POAG

The search for genetic contributors to POAG has been under investigation for several decades.[4, 52-56] Taken as a whole, this work indicates two important characteristics of POAG – it has a strong hereditary component and it is a genetically *complex* disease.[57] Studies comparing first-degree relatives (siblings, parents, children) of POAG-affected individuals to the general population estimate up to a 10-fold increase in the POAG risk.[58] Despite this strong heritability, only a small proportion of observed POAG prevalence can be explained by identified genetic contributions. This is a result of the genetic complexity of POAG. Genetically complex diseases are characterized by genetic heterogeneity, incomplete penetrance, and multifactor interactions. Basically, many genetic factors may act independently or in concert to increase disease risk or confer protective effects.[2] Effectively, this means that POAG is not a single disease explained by Mendelian inheritance of a single allele or a small number of alleles. Instead, it can be thought of as a group of diseases that present similarly enough in clinical settings that they have been traditionally classified as a single condition.

Despite this complexity, mutations in several genes have been found to act independently in causing POAG. Traditional Mendelian inheritance of these mutations can explain only a small subset of observed POAG.[59, 60] The first definitive disease-causing mutations were discovered in the gene *MYOC* by Stone *et al.* in a study comparing the pedigrees of families affected by an early onset form of POAG.[52] Subsequent work has estimated that related mutations in this gene may occur in 3-4% of observed POAG cases.[61] POAG-causing mutations in the gene *OPTN* were also discovered by examining large family pedigrees that displayed dominant inheritance of POAG.[54] The identified mutations seem to be primarily associated with the development of POAG in individuals with normal IOP.[62] Mutations in the region of the gene *WDR36* have been identified in some POAG pedigrees.[63] Subsequent work, though, has sometimes failed to replicate these results and the relationship between *WDR36* and POAG is less clear than in the cases *MYOC* and *OPTN*. [64, 65] Finally, copy number mutations of the *TBKI* have been identified as a cause of POAG. Specifically, duplications of the *TBKI* gene region seem to cause POAG especially in normal IOP cases.[66] Together, these disease-causing mutations are estimated to be associated with roughly 5% of observed POAG cases.[59, 60]

In order to explain a larger proportion of POAG, genome-wide association studies have been applied over the last decade to investigate contributions from more common genetic variants. In a typical study, POAG cases are compared to normal controls across a large number (~1,000,000) of genetic loci. Because of the genetic heterogeneity of POAG and the need to overcome multiple hypothesis testing issues, large cohorts of cases and controls are needed to obtain statistically significant results indicating a genetic association with disease. Nevertheless, a number of novel associations have been indicated via GWAS over the past several years. These include variants near the genes *CAVI* and *CAV2*[67, 68], *SIX1* and *SIX6*[69], *SRBD1*[70], *CDKN2B*[71], *TMCO1*[69, 71], and *ELOVL5*. [70] Although several of the results have been replicated in follow-up

cohorts, the effect sizes of these variants seem to be relatively small (much, much lower than *MYOC* or *OPTN*) and they explain only very small amounts of observed POAG.[3, 60]

To further address the genetic complexity of POAG, case-control GWAS work has been supplemented with the use of endophenotypes. Endophenotypes are quantitatively measured biological markers with two important characteristics: they are hereditary and are related to the disease of interest.[3] Each of these endophenotypes may serve as a less complex trait with identifiable genetic components that acts as only one aspect of the overall disease process. Also, because endophenotypes are quantitative traits, they can provide more information than the binary disease classification[2, 3, 72]. Endophenotypes have successfully been used identify genetic contributors to other complex diseases such as heart disease[73], diabetes[74], and psychiatric disorders.[75] In the case of POAG, both ONH structural measurements (CDR, rim area, cup area, and total disc area) and other risk factors (IOP, CCT) have been employed extensively as disease endophenotypes.[4, 68, 76-79] Significant genetic contributors to ONH structural measurements include *CDKN2B*[79], *SIX1/6*[77], *ATOH7*[4], *CDC7*[4], and *CHEK2*. [80] IOP has been linked to genetic factors near the genes *TMCO1*[81], *CAVI*[81], *CAV2*[82], *FNDC3B*[81], and *GAS7*. [83] Finally, CCT has been associated with *FOXO1*[84], *ZNF469*[85], *COL5A*[86], and *FNDC3B*. [86] Recent meta-analyses of large, combined cohorts have replicated many of these results and provided some evidence for additional genetic associations.[80, 87] This is not an exhaustive list of discovered associations, rather a subset of those that have been replicated multiple times are have been associated with multiple endophenotypes or POAG. As in the case of POAG, the endophenotypes (IOP, CCT, and ONH measurements) are strongly hereditary with estimates of genetic factors being responsible for >50% of the observed variability in these measurements.[88-90] Since the discovered factors fail to explain much of this

variability, there are likely many as-of-yet undiscovered genetic contributors to these endophenotypes.

Several of the genes associated with these endophenotypes (*TMCO1*, *CAVI2*, *SIX1/6*, *CDKN2B*) have been previously associated with POAG suggesting that, at least in part, disease risk is conferred by these factors via modulation of their corresponding endophenotypes. The remaining endophenotypic genetic factors suggest possible lines of inquiry for further discovery of POAG genes and molecular experiments to elucidate the biological processes underlying disease etiology.

The identification of novel POAG-related measurements that are both objective and quantitative could help not only in screening or disease detection settings, but could also serve as POAG endophenotypes. Endophenotypes that could help reveal more of the unknown genetic basis of POAG.

## CHAPTER 3

### FUNDUS IMAGE PROCESSING

Processing and analysis of fundus images has been a staple in both ophthalmic clinical and research settings for decades.[91] The eye provides unique imaging opportunities because the structure must allow light to reach the retina for proper functioning. This means that much of the vital anatomy of the eye can be imaged directly using specialized camera set-ups. The ease-of-imaging and usefulness in diagnostic applications has led to the collection of large-scale fundus image datasets which can be exploited to develop automated disease detection techniques.[13, 92] Researchers have done just that in developing a plethora of techniques to automate the process of analyzing and extracting clinically important information from these images.[93-96] This includes techniques meant to detect not only glaucoma, but other blinding diseases such as age-related macular degeneration and diabetic retinopathy as well.[97, 98] The imaging window provided by the eye also allows researchers to study systemic diseases. The clear view of vasculature and neural tissue has been especially useful for investigating cardiovascular disease and muscular dystrophy.[99, 100]

Before any of these important clinical applications can be performed, though, preprocessing steps must typically be applied to the raw fundus images. Preprocessing can serve to remove noise or artifacts, highlight image features of interest, identify specific anatomical features, or align images to one another. The following sections will detail two important preprocessing steps applied to fundus images for this work. These steps were required to (1) identify the ONH region and (2) extract three-dimensional information from the stereo images. In both cases, the methods were implemented in C++ using the Insight Toolkit (<http://www.itk.org/>).[101]



### Optic Nerve Head Localization

The analyzed fundus images were collected at multiple sites using differing cameras and imaging setups. The resulting images were not standardized in their framing of the ONH region or field of view. To perform comparisons across this set of images, the ONH region was identified in each image and a standardized region was extracted. While this is a straightforward task for human observers, the scale of the datasets considered here (10,000's of images) made manual annotation of ONH regions impractical. Instead, an automated approach for locating the ONH was implemented and applied to the fundus images. Localization of the ONH region in fundus images has been widely published on.[102-106] Rather than develop a brand new technique to a problem that has been so well studied, an existing approach was adapted, implemented, and evaluated for use on the dataset. The method described in the following sections was adapted from the pixel classification approach proposed by Niemeijer *et al.*[107]

#### Algorithm Description

The algorithm employed here took a pixel classification approach. This means that to identify the ONH location within an image, a trained classification model is applied to each pixel within the image. For each pixel, the model produces an estimate of the pixel's distance from the center of the optic disc. Selecting the pixel location estimated to be nearest to the optic disc center generates the final estimate of ONH location.

A standard  $k$  nearest neighbor classifier was used to produce these estimates. In this model, a prediction for a query is made by averaging the  $k$  most similar known examples. Specifically, each pixel is described by a set of  $d$  predictor features arranged into a feature vector. A trained model consists of a set of example  $d$ -dimensional feature vectors along with their corresponding true distances from the optic disc center (i.e. the training set). To apply the model to a new pixel, the feature vector for the new pixel is

computed and the set of  $k$  nearest neighbors is determined. The estimate of distance from optic disc center is the average distance of these  $k$  neighbors.

Selecting an informative set of predictor features is vitally important to producing accurate estimates of the ONH location. In the work by Niemeijer *et al.*, a segmented, circular window was used to compute features at each pixel location. The window was segmented into four equally sized quadrants corresponding to the superior, inferior, temporal, and nasal directions. The use of these segments aids in capturing information related to highly oriented structures, such as the vessels that extend from the optic disc. See Figure 3.1 for an illustration of the segmented window. The size of this window is a parameter to the method and is chosen so that the window is roughly the optic disc size. For this analysis, the window radius was selected at 75 pixels based and manual annotations of optic disc size.

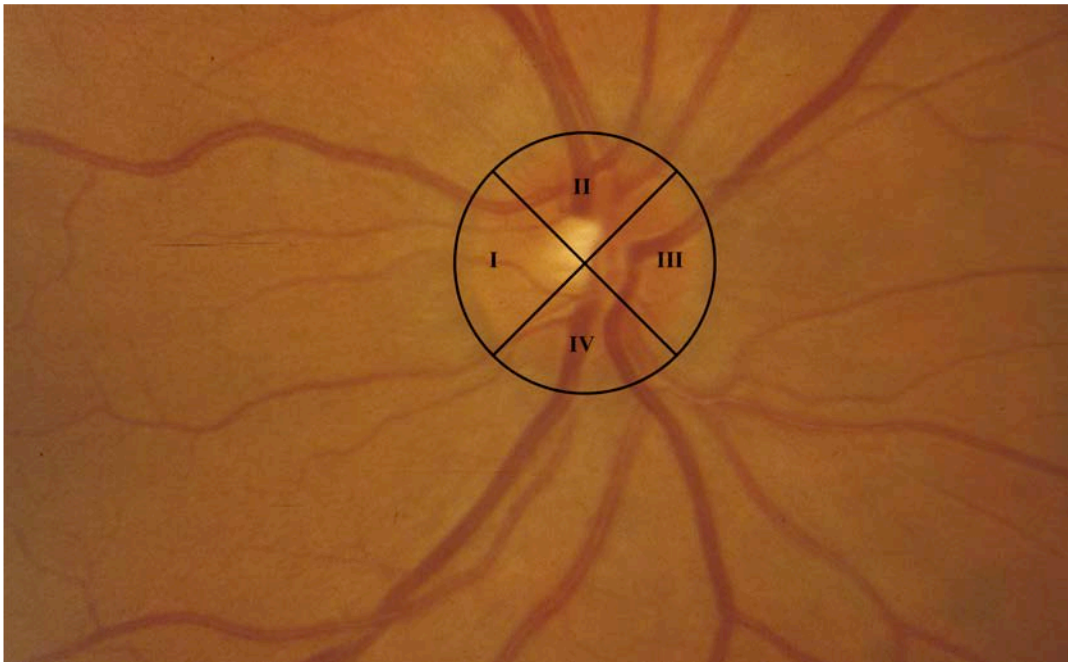


Figure 3.1: The segmented window overlaid onto an example fundus image. This window was used to compute features at each pixel location. Features were computed based on each quadrant (I – IV) individually as well as the entire window.

The original method used features based on both pixel intensity and vessel structure. In this version, the vessel features were excluded and replaced with a new set of features. These new features extracted information about location and circular patterns within the images. The list below details the features that were considered. In 1 – 3, features were computed for each window segment (I – IV) separately and the entire window (whole). In 4 – 6, the window was not needed. This generated a set of 18 total features:

1. Mean intensity of the green channel.
2. Variance of the green channel.
3. Average value of Hough circular transform of green channel.[108]
4. X coordinate of pixel location.
5. Y coordinate of pixel location.
6. Radial location of pixel (distance from image center).

Additionally, this set of features was augmented by the use of image filters. The filters were generated by applying principal component analysis (PCA) to a set of example image patches containing optic discs extracted from manually annotated fundus images. Briefly, applying PCA to optic disc image patches can reveal the average optic disc and the major modes in which their appearance varies. See Chapter 4 for an expanded discussion of PCA.[109] Five of these filters were generated and each was resampled to three different scales (128, 256, and 512 pixels) to help account for differing optic disc size. Each feature was applied to fundus images via a standard image correlation operation. See Figure 3.2 for an illustration of these filters. This brought the total number of features to 33. With the set of features in place, the  $k$  nearest neighbor model could be constructed and evaluated.

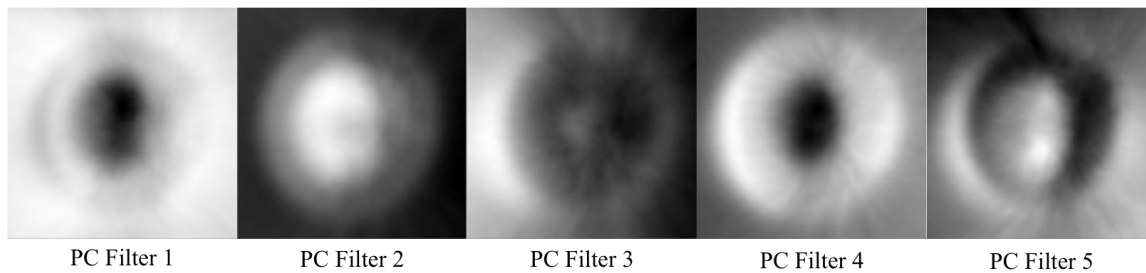


Figure 3.2: The set of PCA-derived filters that were used to augment optic disc predictive features. Each of these filters was applied at three different scales to compute features used to estimate ONH location.

### Algorithm Evaluation

Evaluation of the algorithm was performed using comparisons to manually annotated optic disc center locations. For this evaluation, a set of 3270 images was manually annotated for optic disc centers and a random subset of pixels ( $n = 100,000$ ) were chosen from across these images. These pixels were further divided into training and testing sets using an 80/20 percent split. The complete set of features was computed and feature vectors constructed for each of these pixels. This dataset was used for feature selection, parameter selection, and model evaluation.

Feature selection was performed because the complete set of 33 features may not provide the best feature space to perform prediction. In fact, choosing a high-performing subset of features may serve to both increase performance and efficiency by reducing the need to compute unhelpful features. Evaluating the exponential number of possible feature subsets, though, is impossible so a heuristic method was used. For this selection, a greedy, forward selection procedure was applied. Selection consisted of evaluating a model built with each feature individually. The best individual feature was chosen and added to the working feature set. At each subsequent step, models individually incorporating each remaining feature were evaluated to determine which would be added. This process was continued iteratively until performance of the overall model stopped

increasing by adding new features. The selected set consisted of 19 features: mean intensity (whole), intensity variance (I – IV, whole), x location, y location, radial location, PC Filter #1 (256, 512 pixels), PC Filter #2 (512 pixels), PC Filter #3 (128, 256, 512 pixels), PC Filter #4 (128, 256 pixels), and PC Filter #5 (256, 512 pixels). This selected set outperformed all others that were evaluated including the full set features. Figure 3.3 shows an example input image and the corresponding feature image for each of the selected features.

The model performance was further improved by optimizing the parameter  $k$ , which controls the number of nearest neighbors used by the model to estimates. This optimization was performed by building and evaluating models with varying values of  $k$ . Figure 3.4 illustrates the effect of varying values of  $k$  on the model error. Based on this evaluation, a value of 11 was chosen for  $k$ .

After feature and  $k$  selection, the model estimated the optic disc center with an average absolute error of 11.1 pixels corresponding to 7.8% of the average optic disc diameter. Figure 3.5 shows several example input images, predictions generated by the model, and comparisons to the human annotated truth.

### Depth Inference

The primary modality for capturing three-dimensional structural measurements of the ONH for this work was the use of stereo fundus photography. Development of algorithms to estimate three-dimensional information from stereo pair has been an active area of research for many years.[110-112] At the heart of this depth inference problem is the need to compute the correspondence of points within one image of the pair to points within the other image. The correspondence identifies the points in each image that represent the same point in the photographed scene. From the correspondence, the magnitude and direction of the offset between corresponding points in the images (disparity) can be computed. The depth at each point within the scene can be estimated

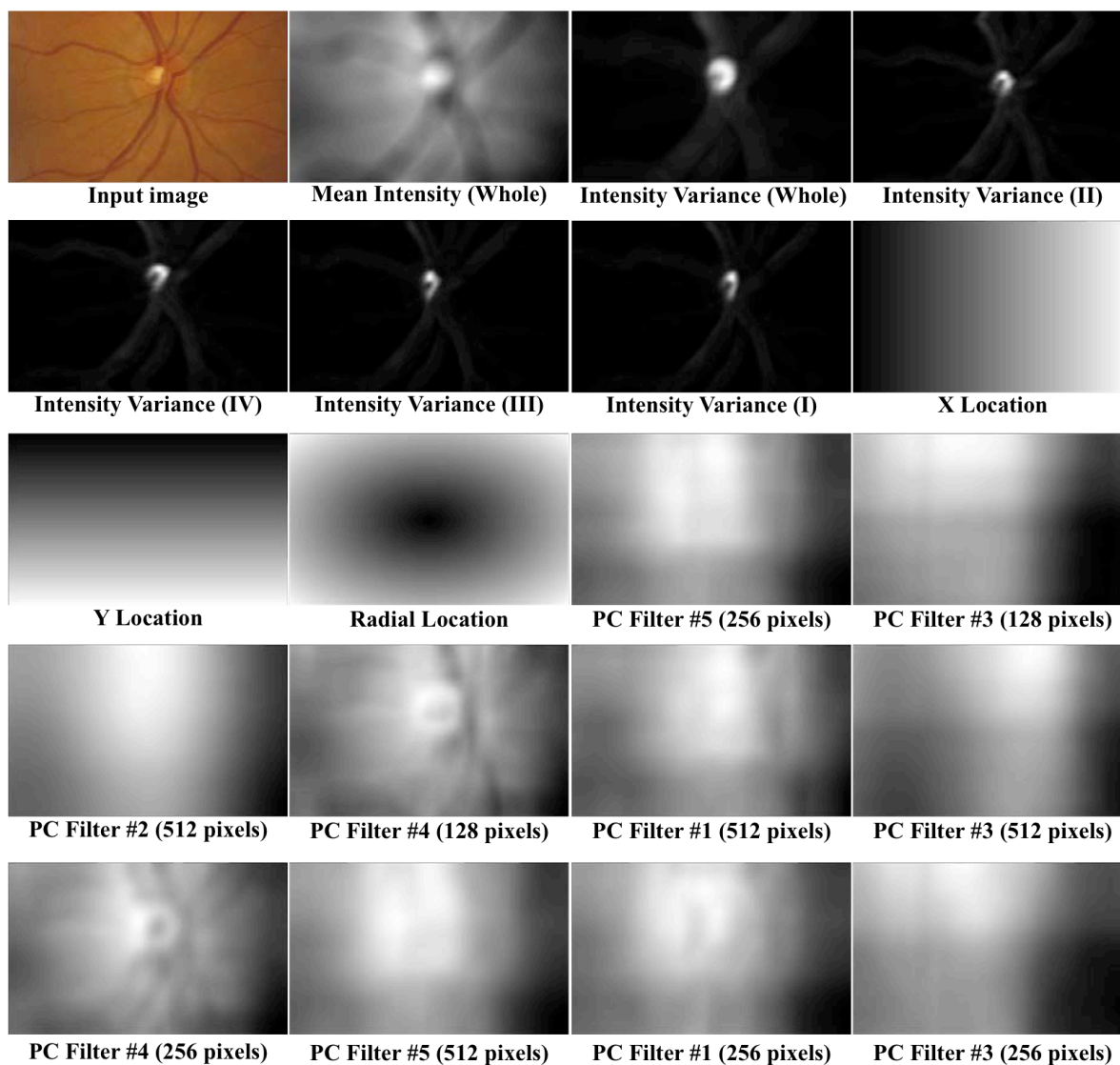


Figure 3.3: An example input image is shown along with images illustrating the selected features used in the automated ONH localization method. The features are shown in the order that they were chosen in during greedy forward feature selection.

### ONH Estimation Error vs. Number of Nearest Neighbors

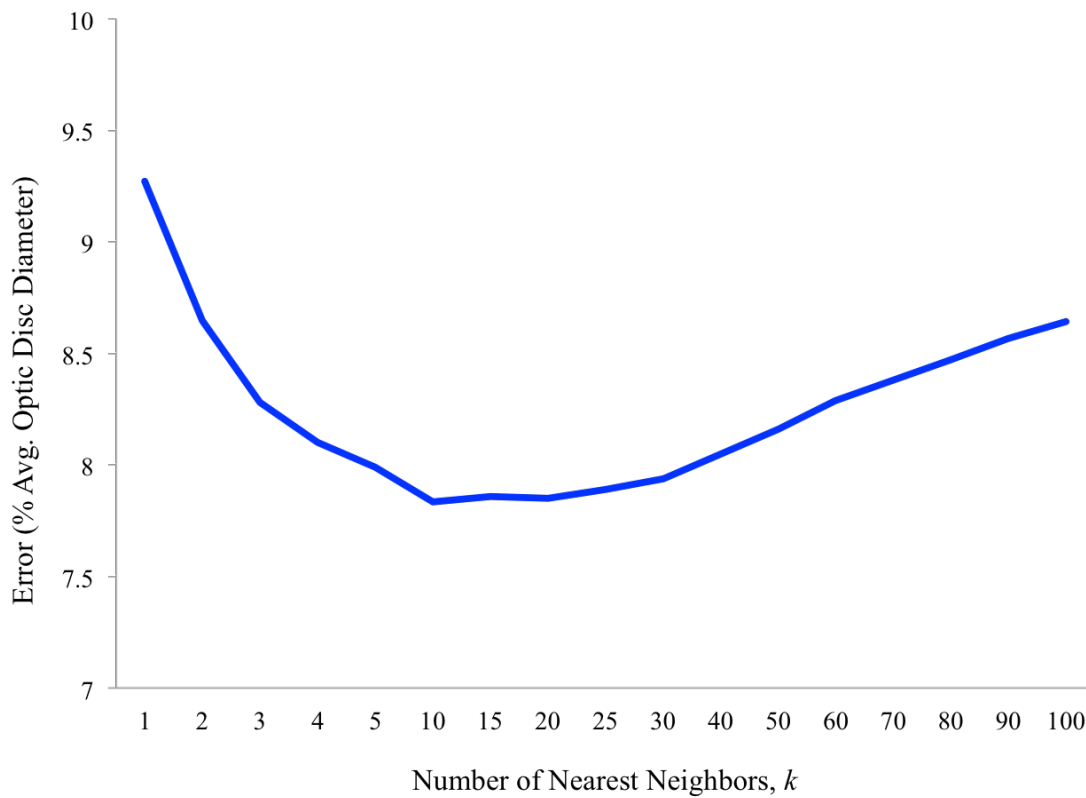


Figure 3.4: The effect varying the number of nearest neighbors,  $k$ , on model performance. The lowest observed error was achieved by setting  $k$  equal to 11.

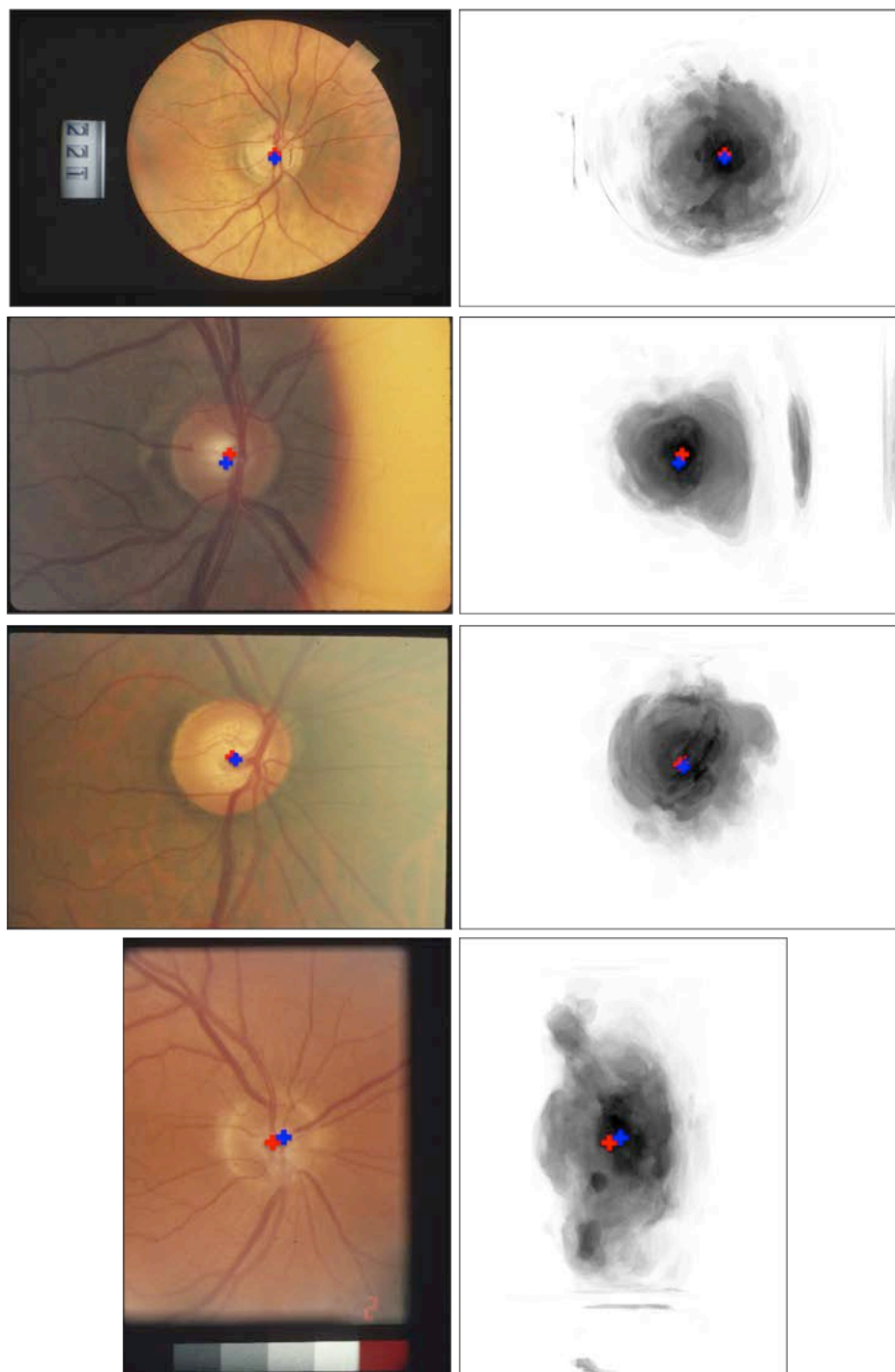


Figure 3.5: The ONH localization model applied to example fundus images. The input images (left) are shown along model output (right). Final point estimations (blue) and human annotated truth (red) is also shown.



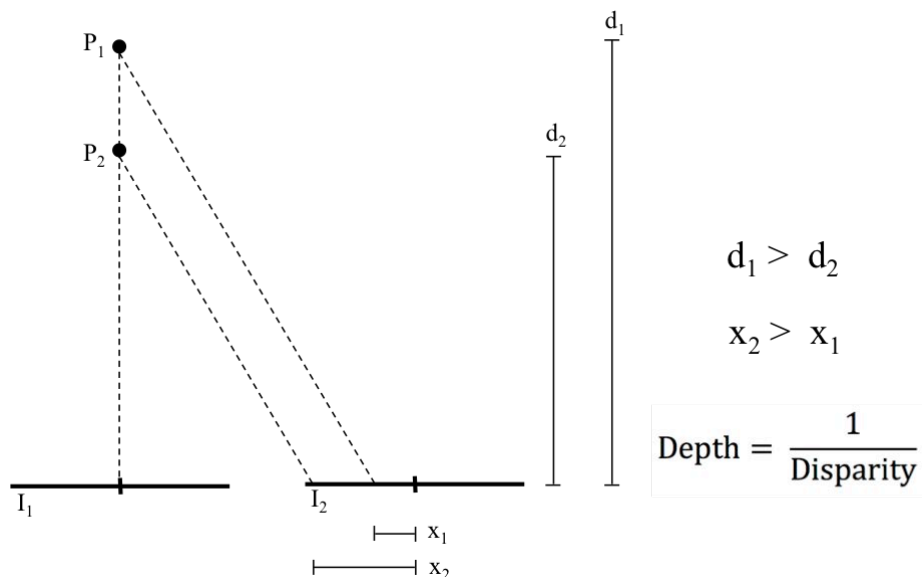


Figure 3.6: In stereo photography, the disparity (the difference between the position of a point in each image) is inversely proportional to the point's three-dimensional depth. The scene points  $P_1$  and  $P_2$  differ only in depth ( $d_1 > d_2$ ). Dashed lines indicate the projection of each point onto the images  $I_1$  and  $I_2$ . Their disparities are given by  $x_1$  and  $x_2$ . Note that as depth decreases from  $d_1$  to  $d_2$ , the corresponding disparity increases from  $x_1$  to  $x_2$ .

directly from these disparity values.[113] See Figure 3.6 for an illustration of the relationship between disparity and depth.

Broadly, the depth inference algorithms must generate some estimate of point correspondences, compute a cost associated with the correspondence, and then refine the estimated solution.[110] Algorithms have applied a variety of approaches in performing these tasks including the use of both local and global cost functions, multi-scale image representations, iterative disparity refinement, smoothness constraints, object segmentation, and many other techniques.[114-117] Regardless of the specific techniques employed, estimation of point correspondences is made more difficult by image pair differences caused by the imaging setup and imaging artifacts such as differences in

illumination, surface reflectance, and focus.[118, 119] Additionally, different viewing angles induce a perspective change leading to changes in apparent shape or occlusions.[115] An algorithm for determining the correspondence mappings must be robust for these issues. Standardized datasets (such as the Middlebury dataset) have been generated so that algorithm performance can be compared directly and reports of top performing algorithms have been released periodically.[110, 120]

The problem of inferring depth from fundus images is made more difficult by limitations on illumination and imaging geometries related to patient safety/comfort that are specific to stereo fundus imaging. The resulting images have low contrast, limited spatial spectrum, and more noise than regular stereo pairs typically evaluated with standard stereo correspondence algorithms.[121] Because these limitations, many generalized depth inference algorithms, even those with the highest performance on the Middlebury dataset, fail to correctly estimate depth from fundus images.[121] Therefore, the algorithm developed by Li *et al.* used to infer ONH structure from stereo in this work has been optimized for handling the particular challenges of stereo fundus images.[121]

Because OCT data provides more direct measurements of depth, algorithm performance was evaluated by comparing inferred depth to OCT-derived depth values.

### Algorithm Description

The algorithm employed here uses a multi-scale image representation and a localized search window to find correspondence at each image point. Following a standard scale space approach, the coarser scales are generated by convolution with a Gaussian kernel followed by subsampling of pixel intensities.[122] This generates a pyramidal image representation with the highest resolution version of the image at the base and each subsequent level corresponding to a coarser representation of the image. See Figure 3.7 for a visualization of the pyramidal image representation.

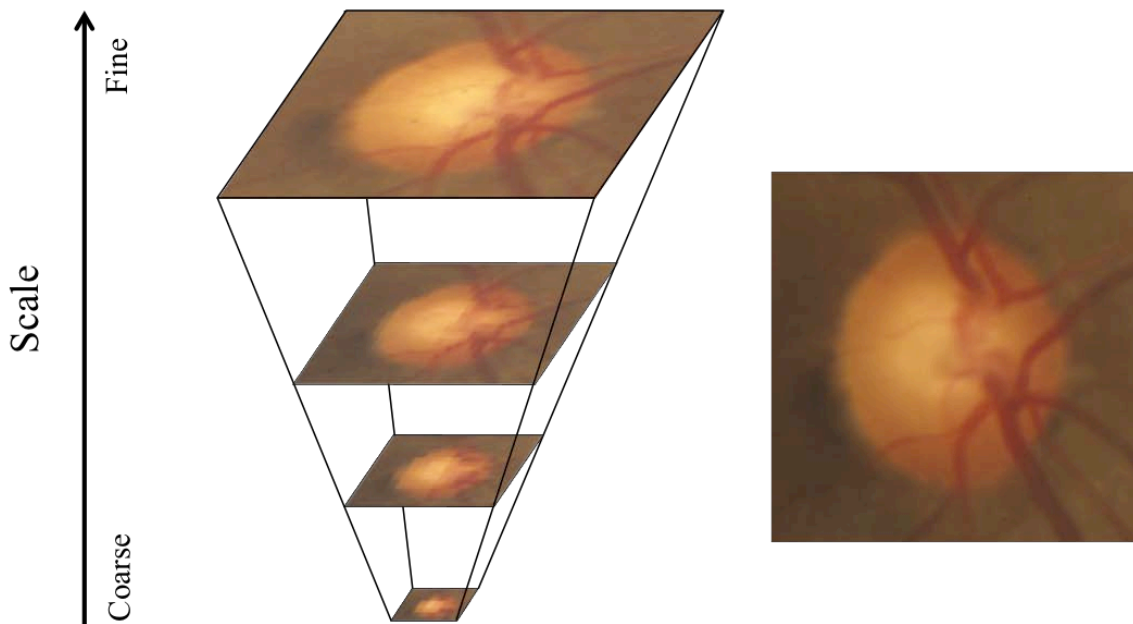


Figure 3.7: The depth inference algorithm uses a multi-scale image representation. In this representation, the scale dimension extends from coarse (down-sampled, Gaussian-blurred) to fine (full resolution, un-blurred) images.

Using this representation, locations in each image of the pair (image  $I_1$  and  $I_2$ ) are given by the pixel location  $(x, y)$  and a scale value,  $s$ , specifying the location with the scale pyramid. The goal of the algorithm is generate a correspondence mapping,  $D(x, y, s)$ , that maps out disparity (and depth) at each location and scale.

In addition to this multi-scale representation, a pixel descriptor function is used to extract useful features from an image location. The features are then compared across the stereo pair to determine similarities between pixel locations in the images. The descriptor function chosen here uses both pixel intensity values and gradient information sampled from a defined window surrounding the pixel (neighborhood  $N$ ) to generate a feature vector describing the local neighborhood. Specifically, the intensity portion of the descriptor,  $F_I$ , at point pixel location  $(x, y)$  and scale  $s$  is given by Eq. 3.1:

$$F_I = \{I(x - n_x, y - n_y, s) \forall n_x, n_y \in N\} \quad (3.1)$$

In this equation,  $I(x - n_x, y - n_y, s)$  is the image intensity at the specified location. The values  $n_x$  and  $n_y$  serve as offsets for each pixel in the neighborhood  $N$ . Basically, this portion extracts the intensity values around the target pixel. The gradient portion of the descriptor,  $F_G$ , is given by Eq. 3.2:

$$F_G = \{G_D(x - n_x, y - n_y, s) * G_D(x - n_x, y - n_y, s) \forall n_x, n_y \in N\} \quad (3.2)$$

Here,  $G_M(x - n_x, y - n_y, s)$  and  $G_D(x - n_x, y - n_y, s)$  give the gradient magnitude and direction of the image at the corresponding location, respectively. This portion of the descriptor is the product of the image gradient magnitude and direction in the neighborhood  $N$ . The final descriptor is obtained by concatenating  $F_I$  and  $F_G$ .

Given the pixel descriptor vector, the matching score is defined so that maximizing this score for each pixel provides an estimation of correspondence and, therefore, depth. In this case, normalized correlation was used as the matching score.

With these pieces in place, the algorithm proceeds by iterating through each scale, going from the coarsest to the finest. Within each scale, a correspondence map is built by comparing every pixel location in  $I_1$  to pixel locations within its corresponding neighborhood in  $I_2$ . For each pixel, the location with the maximum matching score is chosen as the corresponding pixel. After determining correspondence for each pixel at scale  $s$ , a disparity map indicating the  $x$  and  $y$  offsets that map pixels in  $I_1$  to  $I_2$  is constructed. At scale  $s + 1$ , the correspondence search is offset by the scale  $s$  disparity estimate. In this way, correspondence estimates at coarser scales serve as initial estimates for finer scales. The disparity map constructed at the finest scale is used to compute the final depth map indicating ONH structure.[121] The resulting depth maps are represented as gray-scale images with pixel values indicating depth. Figure 3.8 shows an example input image along with the depth maps estimated at each scale. Figure 3.9 shows some example final depth maps and renderings of the ONH structure represented by each map.

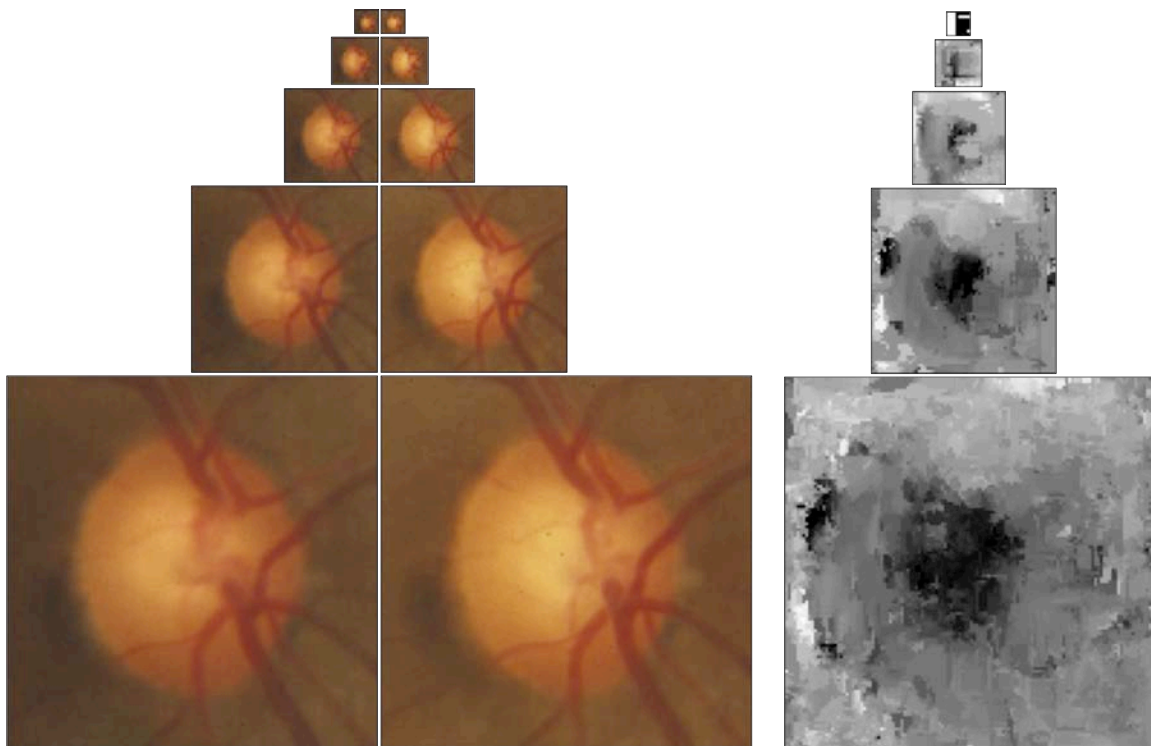


Figure 3.8: Depth inference is performed iteratively using multi-scale fundus image pairs (left) to generate depth estimates (right) at each scale. Depth computed at each scale is used as a starting point for the subsequent scale.

### Algorithm Evaluation

The algorithm was evaluated by comparing depth inferred from stereo fundus to depth measurements captured via OCT. The more direct measurements of retinal structure depth capture by OCT allow a reference standard to be constructed from these images.

The evaluation dataset consisted of images captured from 10 normal individuals. Both stereo fundus images and an ONH-centered OCT scans were collected from each participant on the same day. OCT data were acquired using a Cirrus HD-OCT scanner (Carl Zeiss Meditec, Dublin, CA). To derive a reference standard, layer segmentation

performed on the volumetric OCT images and the surface depth of the most anterior retinal layer (inner limiting membrane) was converted to a gray-scale image similar to the

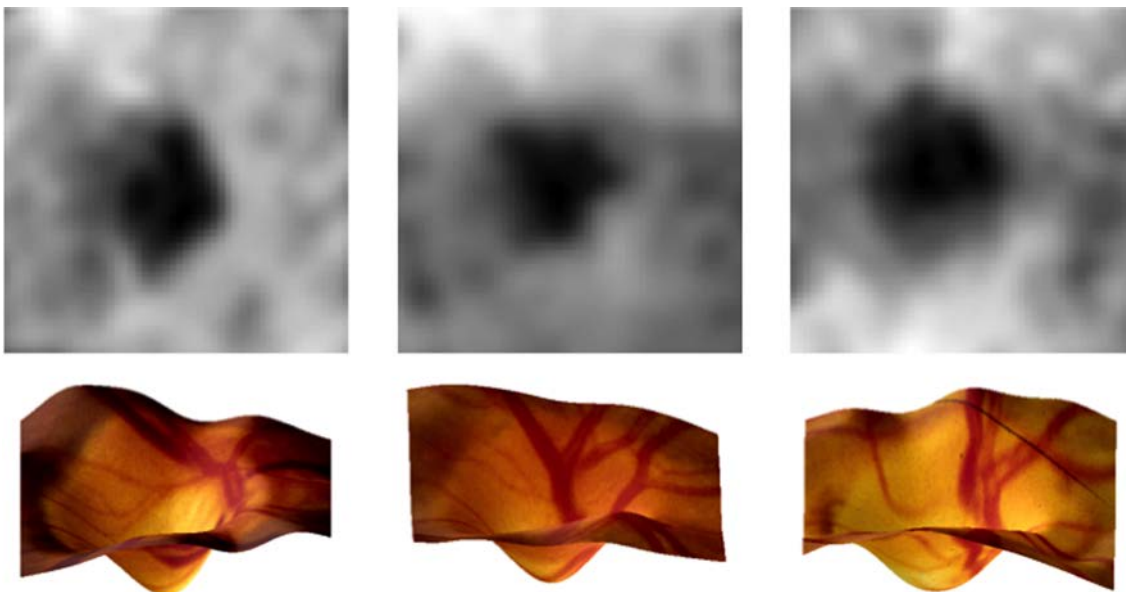


Figure 3.9: Example depth maps inferred from stereo (top) and renderings of the corresponding ONH structure (bottom).

depth map format.[38, 123] Stereo inferred depth maps were generated using the algorithm described above. Prior to evaluation, a Gaussian smoothing filter was applied to reduce noise in the depth maps.

For comparison across image types, the ONH regions from both the OCT-derived and stereo inferred depth maps were extracted. The fundus image pairs and stereo depth maps were manually registered to the OCT images. Once registered, the inferred and OCT-derived depth maps were compared to one another using Pearson's correlation coefficient as a metric. Combining data from all 10 images, a correlation of 0.646 (95% CI: 0.641 – 0.650) was achieved. Figure 3.10 shows the stereo fundus, inferred depth, and OCT depth used for this comparison.

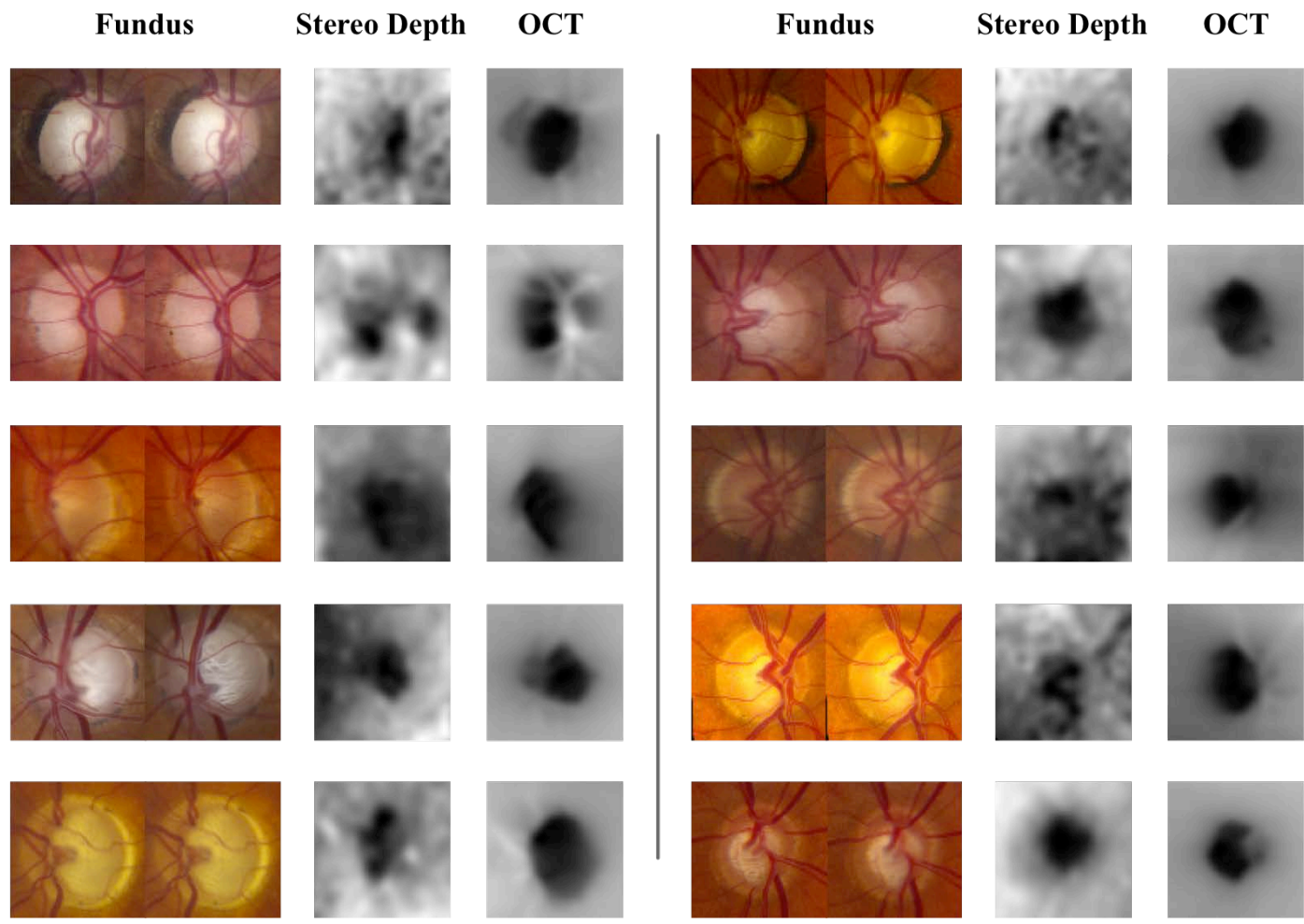


Figure 3.10: Comparisons of ONH region depth inferred from stereo fundus images to depth measured via OCT.

### Conclusion

The methods described here can be used to identify important anatomical features and extract quantitative measurements from fundus images. Identifying these features is often a necessary preprocessing step before biologically important measurements or disease status information can be extracted from fundus images. This makes methods like those described here useful tools in both research and clinical applications.

The ONH localization algorithm uses a pixel classification approach in which features are computed using an anatomically inspired window. The resulting model estimated the center of the optic disc with an average error equal to 7.8% of the optic disc diameter. This accuracy was computed using annotations of the disc center made by a human observer. A limitation of this approach is that the optic disc center is not a precisely defined anatomical point, rather, an estimate of the center point of the approximately circular disc area. Differences between human observers annotating disc centers can affect the training of automated methods and the ability to evaluate the accuracy of these methods. However, even given this imprecision, the level of accuracy achieved here did result in the ONH being localized correctly (within 1.0 optic disc diameter) in >95% of cases.

To accomplish depth inference from the stereo fundus images, an existing algorithm was adapted, implemented, and evaluated. This algorithm produces dense, quantitative depth measurements that map out ONH structure. Comparisons to direct measurements of depth via OCT achieved a correlation of 0.646 indicating a high level of agreement between these methods. This result indicates that depth inference algorithm captures the majority of variance observed in OCT measurements of ONH surface structure. Large errors in depth inference occurred most often in cases where pronounced differences between images within a stereo pair. Differences in focus, illumination, and artifacts are the most common sources of these large errors.



With these automated methods established, analysis of fundus image datasets can be undertaken without the need for costly and time-consuming human annotation. This allows for the use of datasets that are orders of magnitude greater in size. Use of these large-scale datasets does more than just incrementally improve existing models, it allows for the application of data-driven techniques to build entirely new models of ONH structure. These techniques can also exploit the power granted by large sample sizes to perform a more complete characterization of the variation observed within ONH structure. Finally, these large-scale analyses increase power and aid in the discovery of novel associations between ONH structure, clinical measurements, genetics, and disease.

## CHAPTER 4

### BASELINE ANALYSIS OF ONH STRUCTURE

Assessment of ONH structure is crucial to diagnosis of POAG and tracking disease progression. The use of standard structural measurements (e.g. CDR) is complicated by the large variability observed of these measurements in both normal and glaucomatous individuals.[124] In addition to the biological variability, measurement variability is also introduced by the subjective nature of ONH evaluation performed by clinicians.[22] The result of these complications is that, despite extensive work identifying associations between ONH structural measurements and disease, the sensitivity and specificity of these measurements in predicting future development of POAG is limited.[125, 126] This suggests that objective, quantitative measurements of ONH structure may help avoid these limitations and increase accuracy in predicting future development of POAG. To address this need, a data-driven approach to computationally identify ONH structural features is presented and evaluated based on associations with POAG-related clinical measurements and the ability to predict disease outcomes.

This chapter will first describe the computational methods developed to extract three-dimensional information and identify building blocks of ONH structure using a large set of stereo fundus images. Evaluation of the computational features was performed by comparing them to standard clinical measurements used to monitor POAG and to qualitative, expert assessments of ONH structure. Finally, the results of using clinical measurements and ONH structure to predict future development of POAG are presented.[127]

#### Dataset Description

The Ocular Hypertension Treatment Study (OHTS) was a longitudinal, multi-center study conducted to study the development and progression of POAG in a large

cohort of participants. This study considered a set of participants with increased risk of POAG development based on elevated IOP. The set of inclusion criteria required that each participant meet the following criteria at enrollment:[13]

- IOP  $\geq$ 24 mm Hg in one eye and IOP  $\geq$ 21 in the other
- Aged between 40 and 80 years
- Normal ONH in both eyes based on clinical evaluation
- Normal Humphrey 30-2 visual field in both eyes based on clinical evaluation
- Best corrected visual acuity better than 20/40
- No secondary causes of IOP elevation such as anterior chamber damage or IOP-elevating medication
- No previous intraocular surgeries
- No other diseases causing visual field loss or changes to the ONH
- No life-threatening diseases or pregnancy

Using these criteria, 1636 participants were recruited at 22 study sites. Each of these participants was at an increased risk of developing POAG, but was not diagnosed with the disease and displayed no evidence of glaucomatous damage. At enrollment baseline data that included demographic information (age, sex, self-reported ethnicity), clinical measurements (IOP, CCT, CDR, spherical equivalent), visual field testing, and stereo fundus images was collected from all participants. HCDR and VCDR were assessed using stereo photos by two independent, trained technicians and the average assessment was recorded.[13]

The OHTS cohort was followed for up to 14 years (10.7 years follow-up on average) that included semi-annual clinical evaluations and data collection. Data collected at these follow-up included IOP, CDR, POAG evaluation, and (in some cases) stereo fundus images and visual field testing. OHTS defined a specific procedure for determining if and when a participant developed POAG. Specifically, conversion to POAG could be determined either through the use of visual field testing, ONH

evaluation, or both. For visual field testing, two consecutive abnormal visual field test results had to be obtained. If this criterion were met, a final retest was performed and, if also abnormal, the participant was considered to have progressive visual field damage. For ONH evaluation, graders evaluated baseline and follow-up stereo images for hallmarks of POAG damage. Graders were masked to the order of the images (baseline vs. follow-up) and were required to correctly order them for a determination of progressive ONH damage to be made. In both cases, the determination had to be confirmed by two independent graders. Upon confirmation, the case was referred to a committee of clinician for final determination of POAG status. For the purposes of this work, the term “incident POAG” will be used to describe POAG developed by participants during the course of OHTS follow-up.[12, 13, 22]

Capture of stereo fundus photographs was performed with several different imaging systems including specialized cameras that allowed simultaneous capture of a stereo pair and more standard fundus cameras that required sequential capture with the camera/participant adjusting position during pair acquisition. In all cases, the quality of captured images was evaluated based on two criteria: clarity and stereo quality. Clarity referred to overall image quality, illumination, focus, and presence of obscuring artifacts. Stereo quality was determined by the ability of the trained graders to visualize three-dimensional ONH structure using the stereo photos. If the graders disagreed on either quality metric, a third grader was used to make the final determination. Any images that failed to meet minimum quality standards were excluded and the participant was re-imaged. Digitization was performed at the OHTS Optic Disc Reading Center at Bascom Palmer by digital scanning of 35 mm film slides resulting in high-resolution (~6000x4000 pixels) TIFF images. Figure 4.1 illustrates the diversity of stereo fundus images considered here.[22]

A combined dataset of participant demographics, baseline clinical measurements, and disease outcomes from 1635 participants were considered alongside quantitative

ONH structural measurements for all analyses described in this chapter. In the case of visual field test results, a single summary score, pattern standard deviation (PSD), was considered. Table 4.1 provides a summary the non-image baseline data for all participants.

Table 4.1: Summary of baseline data and POAG outcomes for the OHTS cohort.

Measurement	Distribution	Description
Age	$55.9 \pm 9.3$ years	Age at baseline measurements
HCDR	$0.36 \pm 0.19$	Horizontal cup-to-disc ratio
VCDR	$0.38 \pm 0.21$	Vertical cup-to-disc ratio
CCT	$573 \pm 38$ $\mu\text{m}$	Central corneal thickness
Refraction	$-0.65 \pm 2.3$ diopters	Refractive index of best corrected visual acuity
IOP	$25.0 \pm 3.1$ mmHg	Intraocular pressure
PSD	$1.95 \pm 0.30$ dB	Average pattern standard deviation of visual field testing
Sex	56.4 % female	-
Ethnicity	71.2% white, 23.5% African American, 5.3% other	Self-reported participant ethnicity
POAG	83.0 % Non-POAG	Determination of incident POAG

### Structural Endophenotype Identification

With such a large participant cohort to analyze, a methodology to learn the building blocks of ONH structure from the data was applied. The resulting features are referred to as structural endophenotypes (STEPS). The ONH structure for each individual was then represented using this set of objective, quantitative STEPs rather than the small number currently employed clinical features (CDR, disc size, etc.) or the full, high-dimensional depth maps. In order for the stereo fundus images to be analyzed, though, preprocessing of these images was required to allow direct comparisons between participants.

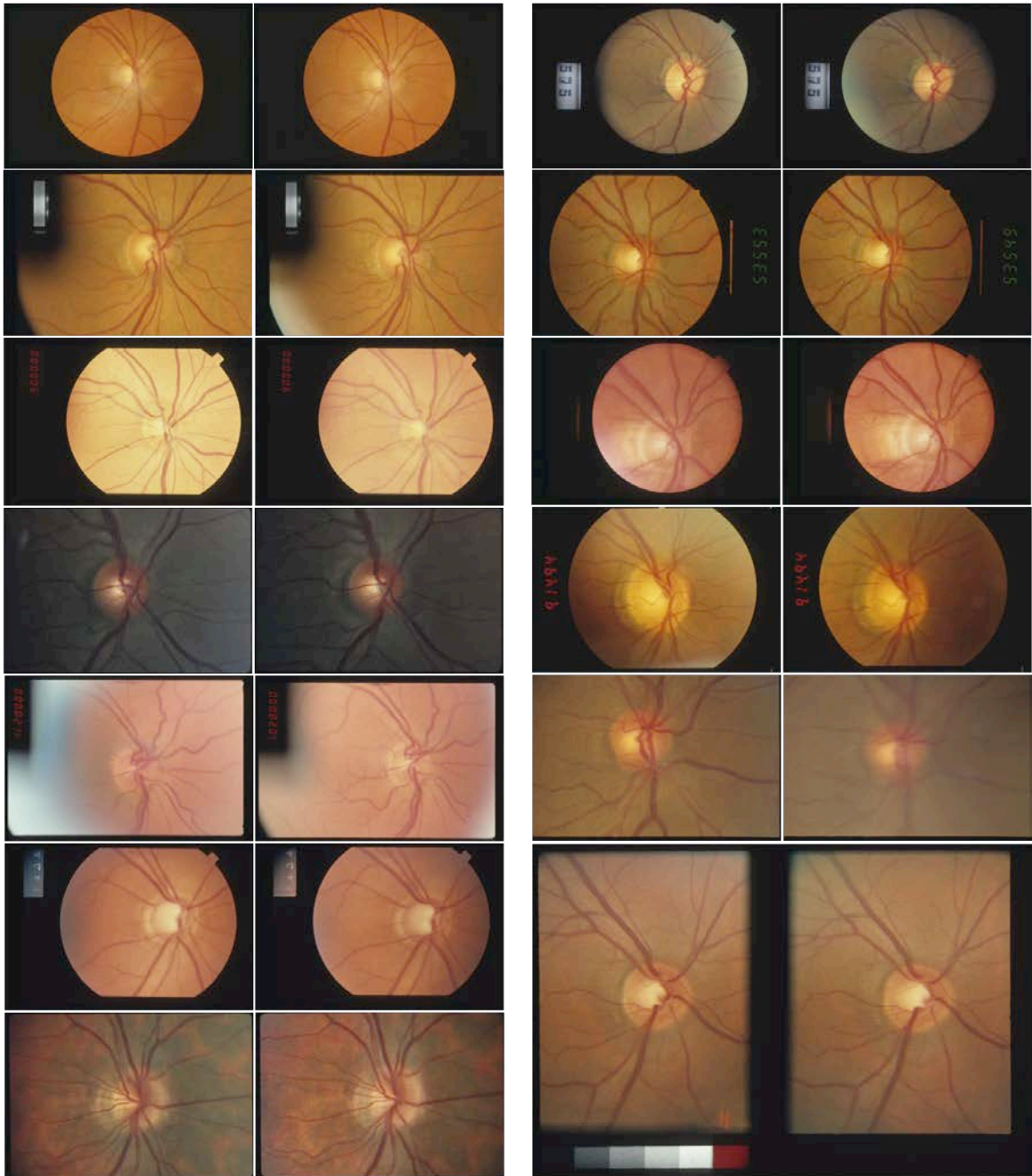


Figure 4.1: Example baseline stereo fundus images from the OHTS dataset. The format differences between different pairs are a result of the different camera types that were used. Despite quality assurance several possible sources of error can be observed with the images. These include over/under illumination, the presence of bright glare artifacts, and differences in focus within an image pair.

## Fundus Processing

Although there was a standard imaging protocol for the study, the different imaging set-ups used at the OHTS study sites resulted in inconsistencies across images collected at different sites. The resulting fundus images did not have a standard field of view, imaging mask, or ONH location. This meant that the ONH region had to be identified and extracted individually for each image. To estimate ONH center, the automated method described in Chapter 3 was used. To ensure accurate extraction from the baseline images, output from this method was manually reviewed and updated when necessary.

The different fundus camera also produced images at different levels of magnification. The large differences in apparent ONH size would prevent direct comparisons across participants and greatly hamper any attempt to derive descriptive ONH structural features. To account for these size differences without affecting relevant ONH structure, images were manually reviewed and, based on appearance, grouped by camera type used to capture them. Optic disc diameter was manually annotated for each image and the mean diameter for each group was computed. Images were then scaled in size so that all groups had equal mean optic disc diameters. These two steps (ONH localization and camera scaling) essentially acted as a semi-automated registration procedure that brought all ONH images into a standard format.

ONH regions were then extracted from all baseline images. In order to ensure that the entire ONH region was captured from each image, a square region with a width of 1.5 \* mean optic diameters centered on the ONH was extracted from each image. This parameter value was varied and 1.5 was chosen based on empirical results (see Appendix A for details). Finally, all extracted ONH regions were down-sampled to a size of 512x512 pixels.

## Depth Processing

The standard-sized, ONH centered stereo pairs resulting from the fundus preprocessing steps were used directly as input to the depth inference methodology described in Chapter 3. The result for each stereo pair was a single gray-scale depth map of size 512x512 with each pixel indicating relative depth at the corresponding ONH location.

Noise reduction procedures were applied to the raw depth output in order to increase the signal-to-noise ratio. Errors in depth tend to occur near the edges of the depth map where there is no overlap in the image pair fields of view. To remove these errors, a standard border of 25 pixels along each edge was cropped out of the depth maps. Errors in the correspondence computation can also occur in areas of the image with little texture or structure where exact pixel correspondence is unclear. This can lead to random noise in the resulting depth estimates. This noise was addressed by applying a Gaussian smoothing filter and down-sampling the depth maps to a size of 50x50. The down-sampling also served to reduce the dimensionality of the depth maps, making computation of STEPs more efficient.

Figure 4.2 illustrates the preprocessing procedures applied to the raw fundus and depth data.

## Feature Identification

Once depth maps were computed and preprocessed as described above, the entire set of maps was used to identify STEPs. The depth map inferred from each stereo pair was vectorized by mapping each pixel location to a corresponding vector component. Using this representation, each depth map consisted of a 2500 (50x50) component vector. Finally, because pixel disparities (and depth) computed on different participants with differing imaging set-ups did not all have the same range of values, a normalization procedure was applied. Specifically, the depth values were adjusted by first computing



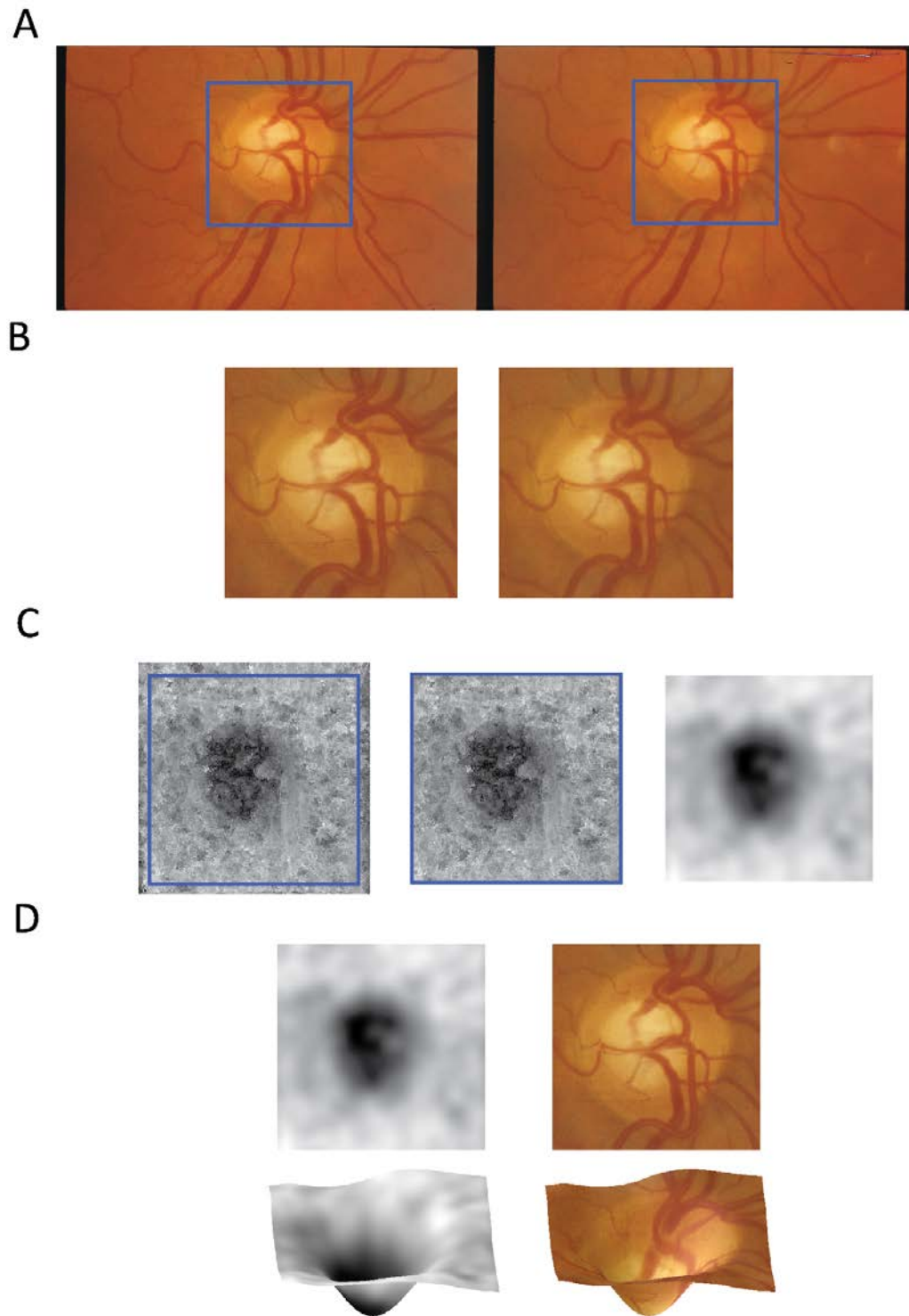


Figure 4.2: Illustration of the fundus and depth processing procedure. (A) Input stereo images. (B) The extracted ONH region stereo pair. (C) The raw depth map, the edge-cropped map, and the smoothed map. (D) Renderings of the ONH structure corresponding to the depth map.

the mean and variance at each pixel location. Standardization was performed so that inferred depth had a zero mean and unit variance across all participants.

STEPS were identified by applying principal component analysis (PCA) to the depth maps. PCA is a technique commonly used to reduce the dimensionality of high dimensional data sets. In general, PCA can greatly reduce the number of dimensions needed to represent a dataset by taking advantage of relationships between input dimensions of the data. This results in a linear transformation onto smaller set of dimensions that explain the majority of the variance observed in the data. The new set of dimensions also possess a natural ordering based on how much of the variance that each explains - the first explains the greatest amount of variance and each subsequent feature explains a smaller amount. By applying this technique to the depth measurements, dimensions (STEPS) that correspond to the common types of variation to ONH structure were identified. In addition, the amount of variance explained each STEP could be estimated. The STEPs provided a new representation for the depths maps in which each was a weighted sum of STEPs. For a single map, the weight associated with each STEP indicates the amount that the corresponding STEP contributes to ONH structure.

Beyond characterizing the major types of variation, the STEPs were used to explicitly model the relationship between ONH and other variables related to POAG. Participant demographics (age, sex, ethnicity), clinical measurements (VCDR, HCDR, IOP, CCT, PSD, refraction), and disease outcome were included in joint models along with STEPs computed from stereo. The relationships between STEPs and other variables were modeled using linear regression and linear discriminant analysis (LDA) based approaches. These differing approaches were applied to account for the different types of phenotypic variables. In the case of binary or categorical measurements (gender, ethnicity, incident POAG), LDA was used to model the relationship between the variable and ONH structure. LDA is an approach that can be applied to high dimensional data in order to estimate relationships between the dimensions and a categorical variable that

assigns a class to each data point. Specifically, LDA finds the linear combination of dimensions that provides the greatest separation between data points of different classes.[128] In the case of quantitative measurements (age, IOP, CCT, HCDR, VCDR, PSD, refraction), multiple linear regression models were used to model the relationship. This type of linear model is well understood and common statistics can be used to evaluate their suitability for modeling a given relationship. In both cases, the STEP representation of depth maps was used to model each variable of interest. In this approach, the relationship between each variable and the STEPs estimated the contribution of that variable to ONH structure.

#### Structural Endophenotype Evaluation

The STEPs identified via PCA applied to the baseline depth maps are shown in Figure 4.3. The first ten STEPs are shown here and they explained >95% of the variance observed in the depth maps.

The STEPs were evaluated based on the strength of statistical association with the demographics, clinical measurements, and disease outcomes. The STEPs were also used to build machine learning models that predicted incident POAG from baseline stereo photos. In addition to this quantitative evaluation, a more qualitative characterization of the STEPs was performed by comparing them to comprehensive examinations of ONH structure performed by clinical glaucoma experts.

#### Clinical Measurement Associations

The STEPs were first evaluated based on statistical associations with OHTS baseline measurements. To test for significant associations, one-way analysis of variance (categorical measurements) and student's *t*-tests (quantitative measurements) were used.

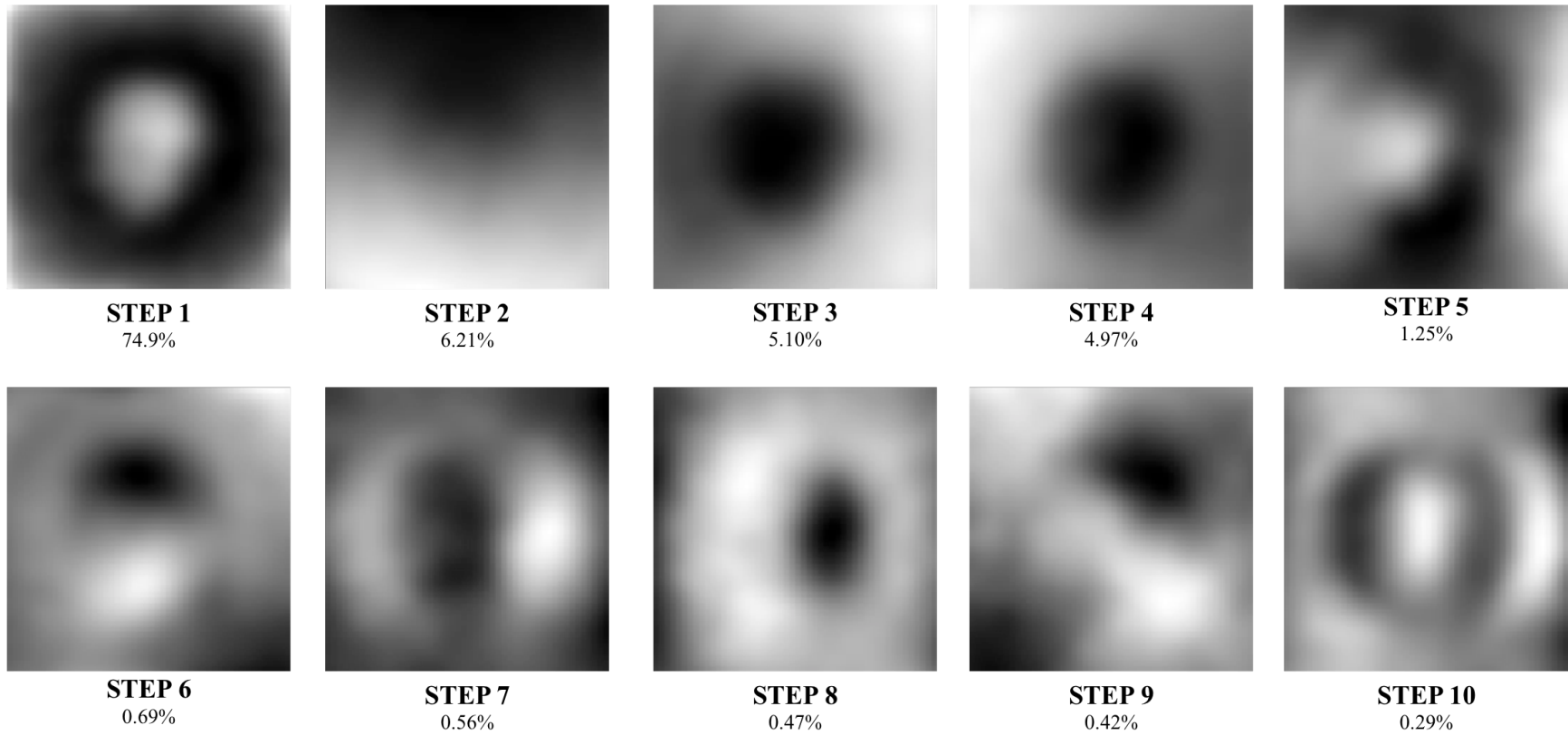


Figure 4.3: Gray-scale representation of the ten PCA-based STEPs used to model ONH structure shown with the percent of variance in depth data explained by each. Collectively, these features accounted for 95% of the variance observed.

Bonferroni correction with an adjusted p-value cutoff of 0.05 was used to account for multiple hypothesis testing issues.

Significant associations were discovered between STEPs and several of the OHTS variables. These include significant associations with age, ethnicity, CCT, refraction, and both HCDR and VCDR. The associations with IOP and PSD were not significant. In the case of the HCDR and VCDR, the resulting phenotype-based STEPs explained roughly 60% of the observed variance in HCDR and VCDR ( $r^2 = 0.62$  and  $0.59$ , respectively). Table 4.2 details the results of this association testing. Each association here was significant after multiple hypothesis correction. These relationships between each variable and ONH structure were also modeled using LDA and linear regression. Figure 4.4 illustrates the estimated contribution of each variable to ONH structure.

Table 4.2: Significant associations between OHTS baseline measurements and STEPs.

Measurement	Significant STEP associations
Age	3
HCDR	1, 2, 3, 4, 5, 6, 7, 8
VCDR	1, 2, 3, 4, 5, 7
CCT	4
Refraction	3, 4
Ethnicity	3, 4, 8, 10
POAG	4, 5

### Disease Prediction

The STEPs were further evaluated based on their utility in building predictive models for incident POAG. For this evaluation, a baseline set of features consisting of only demographic information (age, gender, and ethnicity) was used. This baseline set of

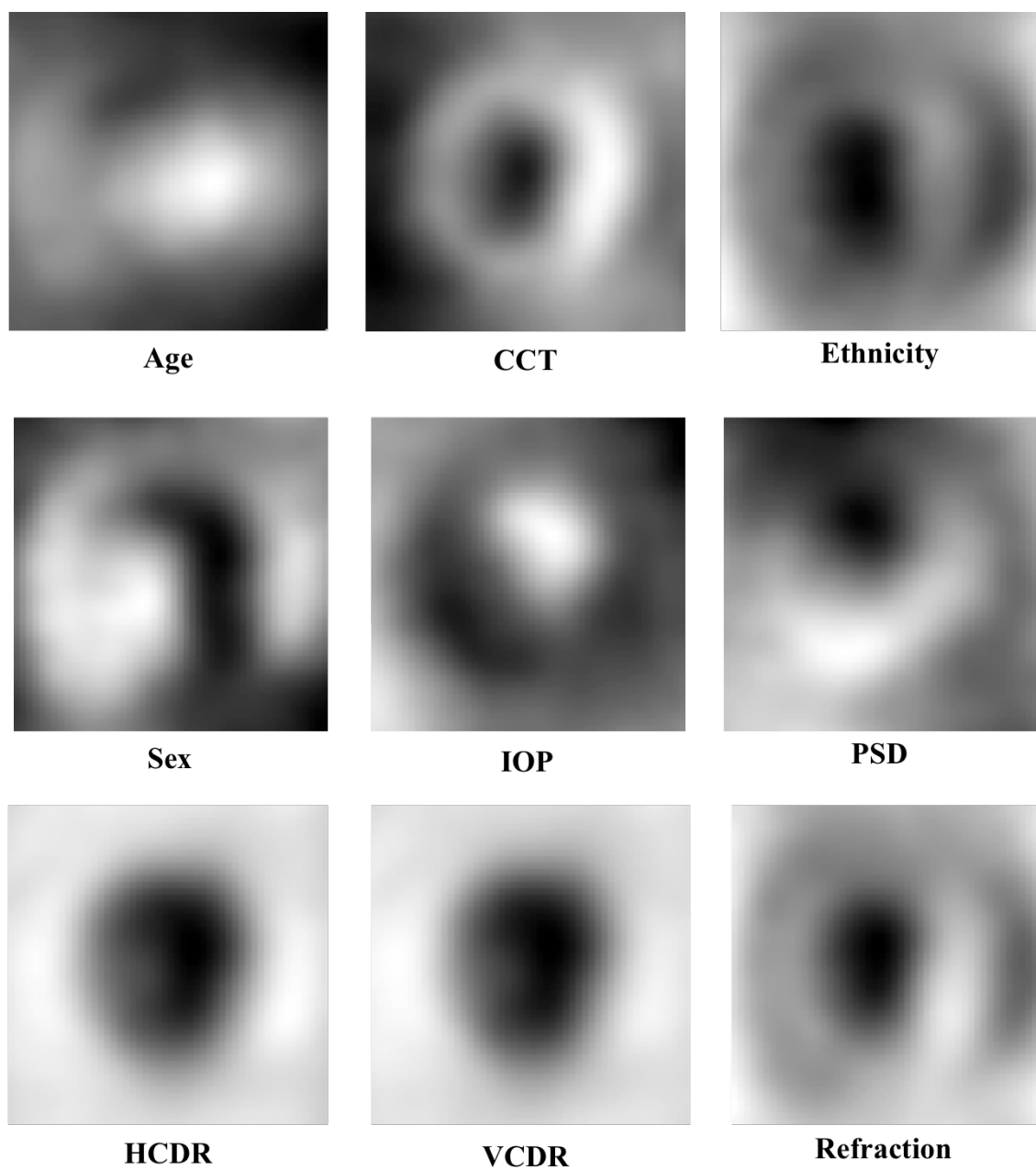


Figure 4.4: STEP features estimating the contribution of demographic and clinical variables to ONH structure.

features was augmented first by adding in the remainder of the OHTS features (see Table 4.1 for the list of features) and then additionally augmented by adding the STEP features. The target in all cases was to discriminate between participants that developed incident POAG and those that did not.

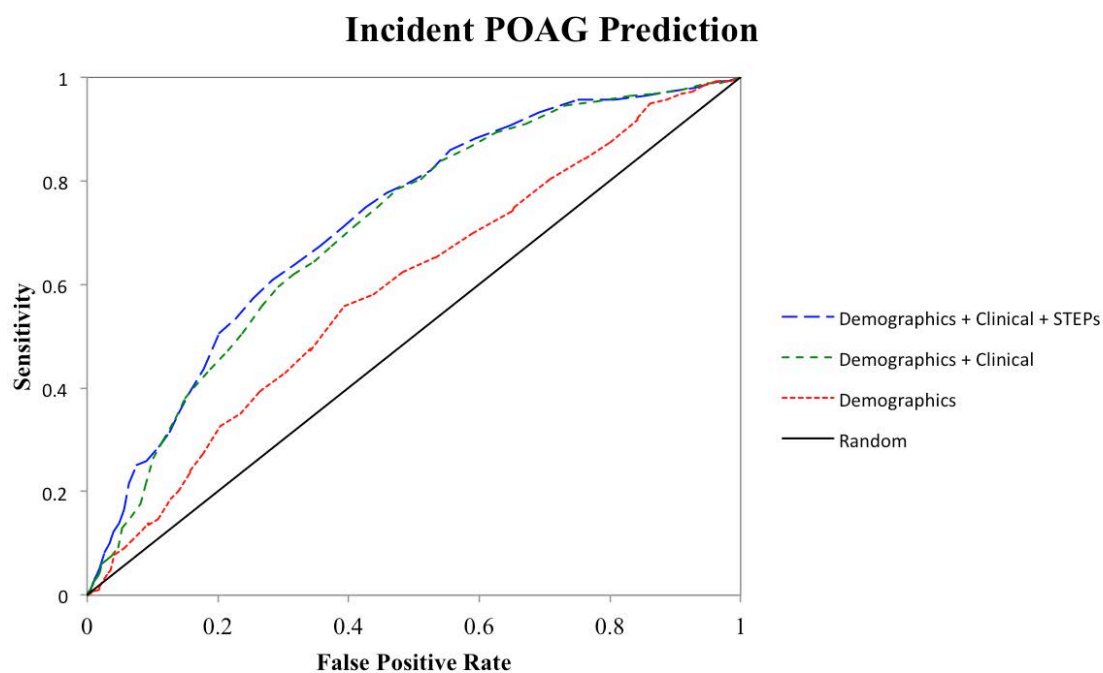


Figure 4.5: Area under receiver operating characteristic curves for incident POAG prediction using combinations of demographic (age, sex, ethnicity), clinical (HCDR, VCDR, IOP, CCT, PSD, refraction), and STEP features.

Based on empirical testing, the predictive model used for this evaluation was a  $k$ -nearest neighbor classifier. See Appendix B for a summary of alternative machine learning models that were evaluated. Area under the receiver operating characteristic curves (AUC) was computed for each feature set. The performance of the features were compared internally to each other as well as to previously published results predicting

POAG in the OHTS dataset. Some previously published results built and evaluated POAG predictive models using the entire OHTS dataset.[129, 130] To allow direct comparisons in these cases, AUC of STEP-based models were evaluated on the training data. Because these estimates tend to overestimate performance, a 10-fold cross validation approach was also used to estimate performance on unseen data.

The set of OHTS measurements and STEP features were evaluated based on their ability to predict which OHTS participants would develop POAG. Using only the baseline (demographic) features resulted in an AUC of 0.720. Adding the remainder of the OHTS measurements led to an AUC of 0.793. Finally, incorporating STEP features boosted AUC to 0.806. The cross validation approach to estimate performance of STEP features on unseen data resulted in an AUC of 0.722 compared to 0.701 using the OHTS measurements and 0.599 using only demographic features. Figure 4.5 shows AUC curves for the different feature sets.

The variations in ONH structure associated with the STEPs were visualized by generating the median ONH structure and then altering it by increasing the individual contribution of a single STEP. The changes to ONH structure induced using this technique are shown in Figure 4.5.

#### Comparison to Expert ONH Review

An extensive review of the stereo fundus images was performed to grade the images for several additional clinically-relevant image and structural characteristics. A subset of the baseline images ( $n = 1053$ ) were independently evaluated by two glaucoma experts for a set 16 different characteristics that describe image quality, rim/cup appearance, pigment loss, and vascular abnormalities. All of these characteristics were encoded as binary grades (present or absent) by each expert. The two sets of grades were combined by into a single numeric grade by encoding expert agreement on absence of a characteristic as 0, disagreement as 0.5, and agreement on presence as 1.0. The agreement



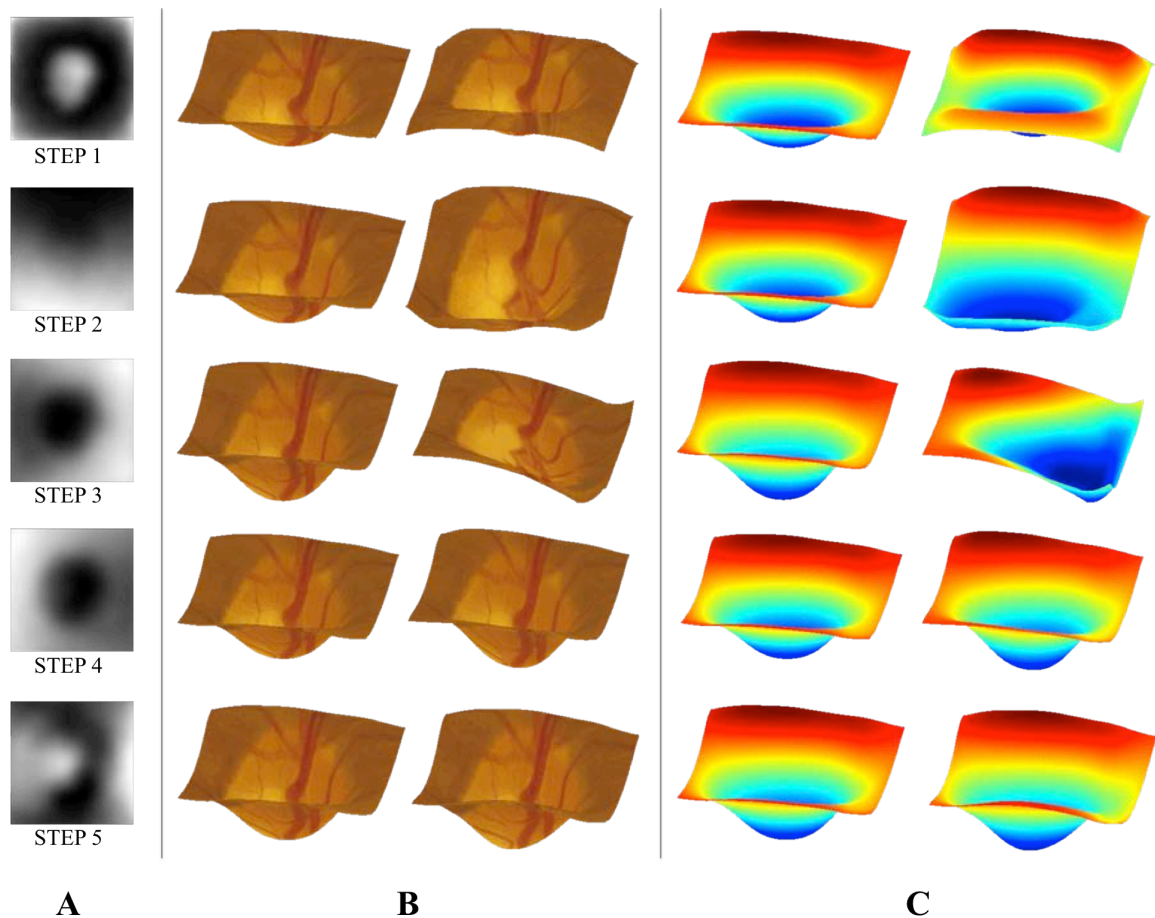


Figure 4.6: Variations to ONH structure capture by STEPs. (A) Gray-scale representations of the first five STEPs. (B) Illustration of the change to ONH structure induced by increasing the contribution of a single STEP. The median structure (left) is shown along with the median altered to exhibit an extreme value of the STEP. (C) The same figure shown as heat maps to indicate depth.

between graders was evaluated using the  $\kappa$  statistic. This statistic is bound to the range of -1.0 (complete disagreement) to 1.0 (complete agreement) with a value of 0 indicating no correlation between graders.[131]

The relationships between STEP features and the graded characteristics were evaluated using one-way analysis of variance (ANOVA) testing to compare the contributions of STEPs to participants at each grade level. This test was applied for each STEP-characteristic pair to determine those with significant associations. A Bonferroni

corrected p-value of 0.05 was used to determine significance. STEPs were found to be significantly associated with stereo image quality, presence of an unusually deep cup, cup tilting, and rim notching in the superior and temporal quadrants. Table 4.3 summarizes the characteristics considered, the resulting grades, and significant associations.

### Conclusion

Computational methods for identifying three-dimensional structural features of the ONH were applied to a large cohort of participants at risk for developing POAG. These methods simultaneously incorporate both imaging and demographic/phenotypic variables to model ONH structure. The identified STEPs serve as objective, quantitative predictive features for POAG and as endophenotypes that can be used to investigate contributors to ONH structure and disease.

Extensive work has been published regarding both diagnosis and early prediction of POAG. This includes methods that that rely on a variety of clinical and imaging-based measurements. In particular, POAG predictive models incorporating age, IOP, CCT, CDR, and PSD have been built and evaluated using data from the OHTS cohort. These models achieved AUCs ranging from 0.74 to 0.77 in predicting future conversion to POAG, depending on the parameters used construct the models.[129, 130] This can be compared to the AUC of 0.806 achieved when incorporating STEPs to predict conversion to POAG in the OHTS dataset. External validation of these models on independent datasets led to AUCs ranging from 0.69 to 0.83, with a median performance across all surveyed cohorts of 0.71.[132] These can be compared to the AUC of 0.722 achieved in cross validation testing of models incorporating STEP features. Although STEP-based prediction fell short of the highest reported AUCs when applying existing models to independent datasets, STEPs did increase AUC when included in models predicting POAG in the OHTS cohort. Incorporation of STEPs into prediction of these independent

Table 4.3: Summary of expert grading and comparisons to STEPs.

Image/Structural Feature	Grade Distribution			Expert Agreement	Significant STEP Associations
	0	0.5	1	$\kappa$	
Image Quality					
Unacceptable clarity	1031	20	2	0.16	
Unacceptable stereo	1049	4	0	0.30	4, 8
Unacceptable scaling	1042	9	2	0.0	
Rim/Cup Appearance					
Deep cup	648	192	202	0.55	3, 4, 5, 6, 8, 9, 10
Pit-like cup	1039	2	0	0.00	
Sloping margin	922	111	8	0.10	
Tilted disc	986	47	8	0.24	4
Vertical elongation of the	959	74	8	0.15	
Peripapillary Atrophy					
Zone Alpha	21	266	737	0.09	
Zone Beta	924	85	18	0.26	
Vascular Abnormality					
Cilioretinal abnormality	948	94	0	0.00	
Radial abnormality	1039	2	0	0.00	
Notching					
Inferior	1003	39	0	-0.02	
Nasal	1030	12	0	-0.01	
Superior	907	122	13	0.13	4, 10
Temporal	983	53	4	0.11	4, 6, 10

datasets is needed to determine if STEPs can likewise aid in POAG prediction in those cohorts.

Recently, more attention has been focused on using ONH structural features measured using several imaging modalities to describe and diagnose POAG. More traditional measurements of ONH structure such as CDR, rim width, optic disc and rim area, and localized rim notching measured using stereo fundus or HRT images have been augmented by internal structural measurements from OCT, especially retinal nerve fiber layer thickness. The resulting diagnostic models have shown higher performance in distinguishing between normal and glaucomatous individuals than previous attempts that fail to incorporate any ONH structure.[25, 133, 134] Work by Sanfilippo *et al.* took a more sophisticated approach to modeling shape and, using methods similar to our STEP methodology, identified optic cup shape features by examining manual tracings of the optic disc and cup from fundus images.[44] Their resulting features achieved high accuracy in discriminating normal and glaucomatous subjects. Though not focused on glaucoma, similar techniques have been applied to retinal pigmented epithelium shape measured using OCT and identified significant associations with disease.[135, 136] The work described here attempts to apply shape modeling techniques to the large OHTS dataset in order to identify features helpful in POAG prediction. This work is limited, though, in that only surface ONH structure could be observed using the available stereo photos and none of the internal structure captured by OCT is available. Ideally, similar methods would be applied to OCT data to computationally identify informative features of internal structure, especially glaucoma-related structures such as the retinal nerve fiber layer. We have considered only stereo-based measurements of ONH surface structure because large-scale, longitudinal datasets (such as OHTS) that include OCT imaging are not currently available.

Using the graphical representations and illustrations of changes associated with the STEPs (Figure 4.6) can allow for some qualitative assessment of these features. For

instance STEP 1 seems to capture structural aspects related to overall size of the cup and rim. STEP 2, on the other hand, demonstrates slope in the vertical (superior-inferior) direction, while STEP 3 captures a similar slope in the horizontal (nasal-temporal) direction. A portion of these observed slopes may be capturing biological variation in cup tilt and retinal surface angle, but some may also be caused by variations in the orientation of the camera with respect to the optic disc. These STEPs help illustrate a limitation of the proposed methodology – the identified STEPs depend on the quality of the input stereo fundus images. Poor imaging conditions or camera orientation could lead to poor quality stereo images and resulting depth maps. The OHTS images used here were screened for overall image and stereo quality so further experiments are needed to determine the robustness of this methodology to image quality.

Several of the other STEPs encode structural features that are plausibly relevant to POAG progression. STEP 4 appears to encode a feature modulating the depth of the cup, whereas STEPs 5, 6 and 8 appear to encode features denoting notching of the neuro-retinal rim at specific positions (inferonasal, superior, and nasal respectively). Other STEPs that were identified by our approach are not easily related to such characteristic ONH features recognized by clinicians. A rim feature that seems to be missing is thinning in the inferotemporal region. Previous work has shown thinning in this region to be an early hallmark of glaucomatous damage.[137-139] The lack of inferotemporal thinning features may be due to the population considered here. Because inferotemporal thinning is considered a hallmark of glaucomatous damage, individuals exhibiting this thinning may have been excluded from the OHTS cohort based on the criterion that participants exhibited no POAG at baseline. The missing inferotemporal thinning is only one example - there could be additional informative features that were not identified because of the characteristics of the OHTS cohort used here. Further study is needed to apply these methods to cohorts drawn from other populations (normal, glaucomatous, etc.) to discover differences and similarities in identified STEPs. Further ONH structural

modeling including longitudinal evaluation of the STEPs, relevant phenotypes, and comparisons to expert evaluations of ONH shape may reveal additional informative relationships.

The aspects of ONH structure represented by each STEP were also evaluated using comparisons to expert grading of the images. The grades provided by the experts in several of the categories (stereo quality, vascular abnormalities, pit-like cup appearance, nasal notching) had only a small number of observed occurrences, which limited the ability to estimate expert agreement and associations with STEPs. For the remainder, expert agreement was generally low. The highest observed value ( $\kappa = 0.55$ ) indicated moderate agreement between experts when grading for an abnormally deep cup. Other values clustered around 0 (no correlation between experts) or in the range of 0.10 – 0.30 (slight agreement). This overall low level of agreement between experts suggests that evaluation of fundus images for POAG-related features is substantially subjective. The comparisons to STEP features also seemed result in significant associations preferentially in cases of high observer agreement. This suggests the analysis was limited by the low agreement further underscores the need for objective measurements of ONH structure to use in both clinical and research settings.

Significant associations between STEP features and the following characteristics were identified: stereo quality, abnormally deep cup, tilted disc, and notching in the superior and temporal quadrants. Despite the statistically significant result, the small number of images categorized as having unacceptable stereo quality limits confidence in its association with any of the STEPs. The other significant cases were not so limited by the number of observations. Of particular note is STEP 4, which exhibited significant associations with having a deep cup, tilted disc, and notching. This feature was also associated with development of incident POAG. These results indicate that STEP 4 may capture some of the early markers of POAG that clinicians look for during evaluation of stereo fundus images.

Previous publications on the use of computational methods for modeling ONH structure found that the methods described here can be used to identify features with significant heritable components and associations with POAG risk factors in smaller cohorts.[6, 7, 140] The results here support and extend those preliminary findings. Using the STEP structural modeling methods, the basic building blocks of ONH structure can be estimated. Evaluation of the resulting STEPs revealed that a small number (10) explained the majority (>95%) of observed variance in ONH structure and significant associations with clinical measurements as well as with POAG. Significant associations of ONH structure with CCT and (as expected) both HCDR and VCDR should be noted, in particular. Given that these have been successfully used as quantitative endophenotypes to investigate genetic contributions to POAG, the results indicate that STEPs can also be used as a tool to investigate POAG and its genetic risk factors.[3, 5] Many of the STEPs showed multiple associations with several different clinical measurements. The presence of so many multiple associations could indicate that some standard clinical measurements may actually be a superposition of basic ONH structural building blocks. Accurate estimates of these structural building blocks will yield new ways to measure ONH structure in both normal and disease cases. Further ONH structural modeling based on large datasets needs to be performed to improve and validate the estimates.

The results presented here showed that incorporation of STEPs led to significant increases in predictive power for future development of POAG over the use of demographic and commonly-used clinical measurements (IOP, CCT, and refraction). Additionally, using STEPs increase predictive power to the level achieved when clinical measurements that require expensive, specialized equipment (PSD) or training (HCDR, VCDR) are used. The speed, low cost, and ease of application make the computational STEP measurements an attractive option for large-scale screening programs because they can be easily and quickly applied to captured images to extract POAG-related features.

Confounding the study and development of treatments for POAG is the fact that it is a genetically *complex* disease. Some cases of glaucoma are caused primarily by defects in a single gene, while others cases are caused by the combined actions of many genetic and environmental risk factors.[60] Family-based studies have identified at least several genes that are capable of causing POAG at elevated IOP (myocilin[141]) and at normal IOP (*OPTN* and *TBK1*).[54, 66] Population-based genome-wide association studies (GWAS) have detected some of the genetic risk factors that contribute to more complex forms of POAG.[2, 71, 142-144] Despite these discoveries, most of the observed heritability of POAG remains unexplained.[2, 3] Untangling the complexity requires examining genotypic and phenotypic data using new methodologies. In recent years, the use of quantitative endophenotypes to study genetically complex disease, including POAG, has become popular.[2, 145] Many population-based studies have searched for and discovered risk factors for quantitative endophenotypes of glaucoma (IOP, CCT, and CDR).[4, 76, 80, 146-148] Further study of additional quantitative endophenotypes (i.e. ONH STEPs) has the potential to identify more genetic contributors to ONH structure and risk factors for POAG.

In conclusion, the STEP methodology was shown to be a powerful tool for investigating POAG and related clinical variables. These methods can extract informative, disease-related ONH structural features from a commonly used and non-invasive imaging modality (stereo fundus). The objective nature and clinically relevant associations of STEPS indicate that they can serve to expand and augment the biomarkers currently used to study POAG.



## CHAPTER 5

### DISCOVERY OF GENETIC ASSOCIATIONS WITH BASELINE ONH STRUCTURE

As a means to better understand the biological processes underlying the ganglion cell death and loss of vision that resulting from POAG, the genetics of not only the disease, but also related structural changes have been investigated. As outlined in Chapter 2, measurements of ONH structure such as CDR, cup area, and overall disc size have been used as endophenotypes in an attempt to reveal the genetic basis for ONH structural features that may affect susceptibility to and progression of POAG. While these studies have been successful in identifying a number of genes that are associated with ONH structural changes, they have not managed to explain all of the observed heredity in ONH structure. The STEP features presented here provide more comprehensive measurements of ONH structure and may be useful in uncovering additional genetic influences.

Previous work has revealed a strong hereditary component to STEP-like measurements derived from stereo fundus images.[149] To uncover the specific genetic factors that account for the hereditary aspects of ONH structure, a combined analysis including both STEP features and genetic data was performed. Two primary approaches were adopted to reveal these relationships. First, genetic loci known to be associated POAG were analyzed to characterize their impact on ONH structure. Second, a broad search that considered loci from across the genome was performed to identify novel genetic associations with ONH structure.

This chapter will detail the methods and results of estimating the impact of individual genetic factors as well as those interrogating the entire genome for genes that influence ONH structure.

### Dataset Description

For the analysis described in this chapter, both phenotypic and genotypic information collected from the OHTS cohort was considered. The phenotypic data of interest consisted of baseline stereo photos and POAG outcome status determined through a series of follow-up visits for the entire OHTS cohort (n = 1635). The stereo photos were the source of quantitative ONH structural measurements. The POAG status of each participant at the end of the study was encoded as a binary variable and used for evaluation purposes. In this cohort, 19.7% of the participants developed POAG by the end of the study.

Genotyping data was only collected for a subset of the participants (n = 1054). The genotyping was performed by the Center for Inherited Disease Research using the array-based Illumina 1M genotyping platform. This platform captured genetic status at nearly a million different loci across the genome for each participant. The full set of 1054 OHTS participants for which both phenotypic and genotypic information was available were used for all analyses described below.

### Genetic Contributions of Known Glaucoma

#### Polymorphisms

To begin characterizing the effect of genetic factors on ONH structure, an approach that directly modeled the relationship between structure and participant genotype was adopted. The goal of this approach was to estimate the individual impact of each genetic factor on ONH structure using STEP features measured from OHTS baseline stereo photos. A problem with this approach, though, is that only a small number of the roughly 1,000,000 assayed genetic factors are likely to have a measurable impact on ONH structure. To help address this issue, a limited set of genetic loci previously reported to have POAG associations were identified and only these were considered when modeling genetic impact on the ONH. The loci were selected based on the strength

of published evidence for associations with POAG or commonly used POAG endophenotypes (IOP, CCT, CDR, etc.) evaluated through review of related literature. Based on the published evidence, these were considered more likely to have an impact on ONH structure that could be identified using STEP features.

### Known Glaucoma Polymorphism Identification

Research into the genetic basis of POAG has yielded numerous discoveries over the last several decades. Overall, the results of this body of work indicate that POAG is a hereditary and genetically complex disease. This means that while development of POAG is largely governed by genetic factors, the observed prevalence of POAG is the result of many different genes contributing to the risk of disease. This complexity makes it difficult to untangle the various genetic factors contributing to POAG.[150]

In recent years, development of GWAS platforms has made large-scale, high-throughput experiments possible. In these experiments, hundreds of thousands of genetic loci known as single nucleotide polymorphisms (SNPs) are simultaneously evaluated. These SNPs are variations in base pair sequence at (typically) a single position within the genome. The different bases observed at one of these locations are known as the alleles of the SNP and an individual's genotype describes the alleles carried by that person. Because each person carries two copies of their genome, that person's genotype for a SNP with alleles *A* and *B* can have one of three states: homozygous *A* (*AA*), heterozygous (*AB*), or homozygous *B* (*BB*). Genetic influence can be identified by testing the genotype for association with a disease or other phenotypic measurements of interest. A significant association can indicate that either the tested SNP or a genetic factor in the nearby genomic region influences the phenotype. In a GWAS approach, a large number of SNPs from across the genome are tested to help identify as many of the genomic regions of influence as possible. This large number of hypothesis tests, though, can limit the ability of GWAS methodologies to identify significant associations. With so many

tests, stringent multiple hypothesis correction needs to be applied to limit the number of false positives. However, with sufficiently large cohorts, statistically significant associations between specific SNPs and POAG can be discovered.

Application of GWAS techniques to POAG has revealed numerous SNPs associated with the disease. These POAG risk SNPs can be found across the genome within numerous different genes. A sampling of POAG risk SNPs and the genes in which they occur can be found in Table 5.1.[4, 67, 71, 76-79, 143, 144] This is a list of SNPs for which there is strong published evidence of association with POAG and not an exhaustive list of all POAG risk SNPs since many of the genetic factors influencing POAG remain undiscovered.[3]

Table 5.1: Set of SNPs previously associated with POAG.

<b>Gene(s)</b>	<b>SNP Identifier</b>
ATOH7	rs7916697
CAV1, CAV2	rs2024211
CDC7, TGFBR3	rs1192419
CDKN2B	rs1063192, rs4977756, SNP9-22023366
CHEK2	rs1547014
DCLK1	rs9575267
ELOV5	rs735860
chr8q22 region*	rs284489
SALL1	rs1345467
SCYL1, LTBP3	rs17146964
SIX1, SIX6	rs10483727
SRBD1	rs17033801
TLR4	rs1554973, rs1927911, rs10759930, rs1360094
TMCO1	rs4656461

\*: There are no known genes near the SNPs in this region

### Structural Endophenotype Identification

In order to model the effect of POAG risk SNPs, ONH structure was represented using STEP features. Briefly, STEPs were identified using baseline stereo fundus images taken of the right (OD) eye for each genotyped OHTS participant. The ONH region was extracted from each stereo image and images were scaled in size to account for differences in magnification across different fundus cameras. The resulting images were a standard 512x512 view centered on the ONH. A custom depth inference algorithm was applied to all image pairs to compute depth maps that describe ONH surface structure. The PCA-based STEP identification methodology was applied to compute the STEP representation of each ONH structure. Figure 5.1 displays gray-scale representations of the resulting STEPs. See Chapter 4 for a more detailed discussion of the depth inference and STEP identification methodologies that were applied.

### Genetic Feature Estimation

The STEP identification process computes features that are optimal in terms of capturing variance observed in ONH structure, these do not necessarily capture the most biologically relevant information. In particular, the computation of STEPs does not consider any information regarding disease state, clinical measurements, or genetics. To address this limitation, linear discriminant analysis (LDA) was used to build models incorporating both STEP features and genotypes. LDA is a technique that can be applied to high-dimensional data that includes class labels associated with each data point. This technique identifies a linear combination of the predictive features that generates a new dimension along which the classes are maximally separable assuming a Gaussian distribution for each group.[128]

In the application of LDA to estimate the effect on ONH structure from each SNP, genotype was mapped to a class variable while STEPs computed from the depth maps were used as the predictive features. Genotypes were mapped to class labels using

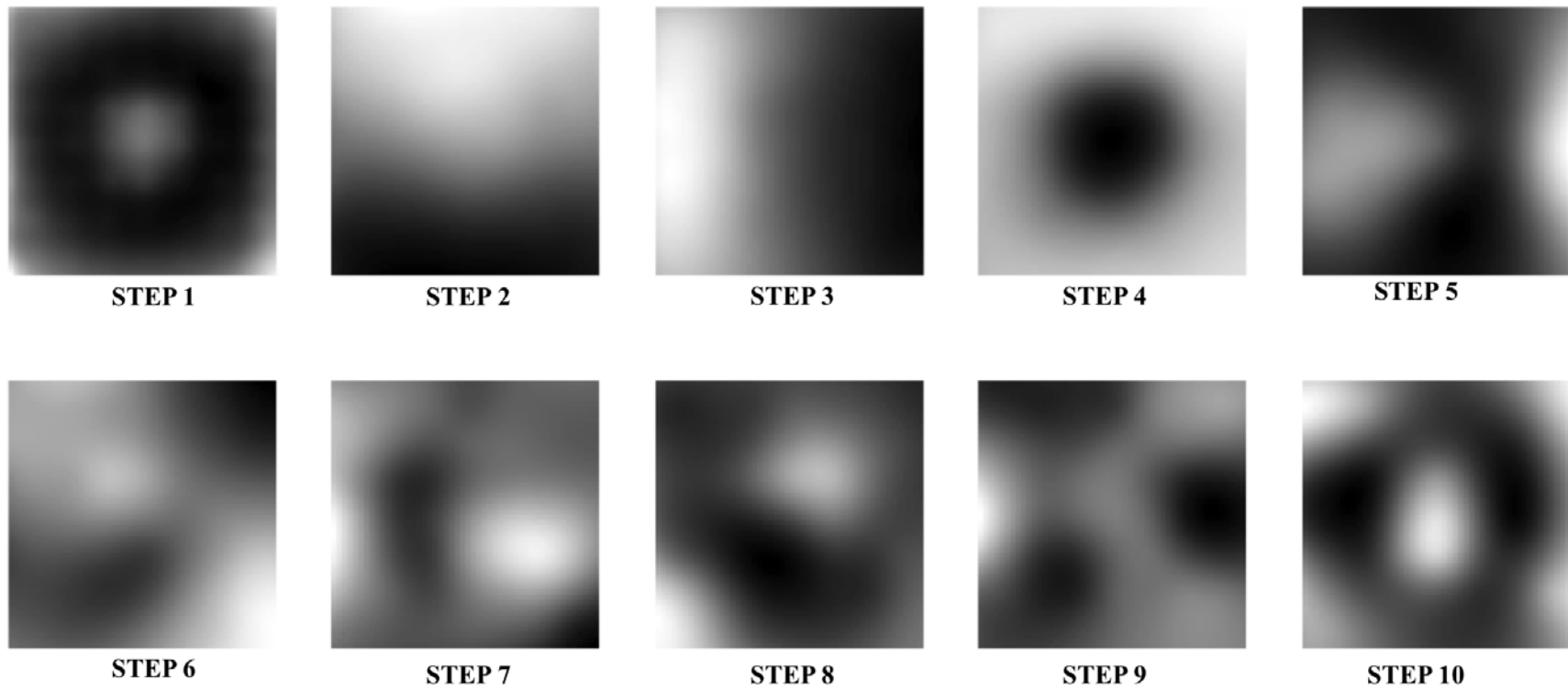


Figure 5.1: STEP features identified using PCA applied to the genotyped subset of the OHTS cohort ( $n = 1054$ ).

an additive genetic model. That is, for a SNP with two alleles ( $A$  and  $B$ ), the class was determined by counting the number of  $B$  alleles observed for each participant. This resulted in three possible classes for each participant at each SNP: class 0 –  $AA$ , class 1 –  $AB$ , and class 2 –  $BB$ . An independent application of LDA was performed for each of POAG risk SNPs. In each case, LDA was used to estimate a feature that provided maximum separability of the participants based on their genotypes. Figure 5.2 illustrates the features resulting from the LDA-based procedure.

### Genetic Feature Evaluation

The genetic features that were learned based on POAG risk SNPs were first evaluated based on associations with their corresponding SNP genotypes. In 17 of the 19 cases, the learned feature exhibited a significant association with genotype. Figure 5.2 shows the resulting features and indicates the p-values of the STEP-SNP associations. Further evaluation was performed to determine if these genetic features were useful in predicting POAG. Of the 19 features evaluated, 12 exhibited significant associations with later development of POAG. Figure 5.3 summarizes these results and illustrates the effect on ONH structure for a few of these features. Finally, the genetic features were incorporated into a nearest neighbor classification model that also included STEPs features and baseline clinical measurements (see Chapter 4 for more details of this model). Adding the genetic features did not significantly change the model performance as measured by AUC.

### Genome-Wide Structural Endophenotype Associations

Further investigation into genetic factors influencing ONH structure was performed using more traditional techniques. Specifically, a GWAS approach was applied to identify associations between STEPs that measure ONH structure and SNP genotypes from across the genome. In this analysis, the STEPs served as quantitative traits and standard GWAS techniques to identify genetic associations were applied. Once

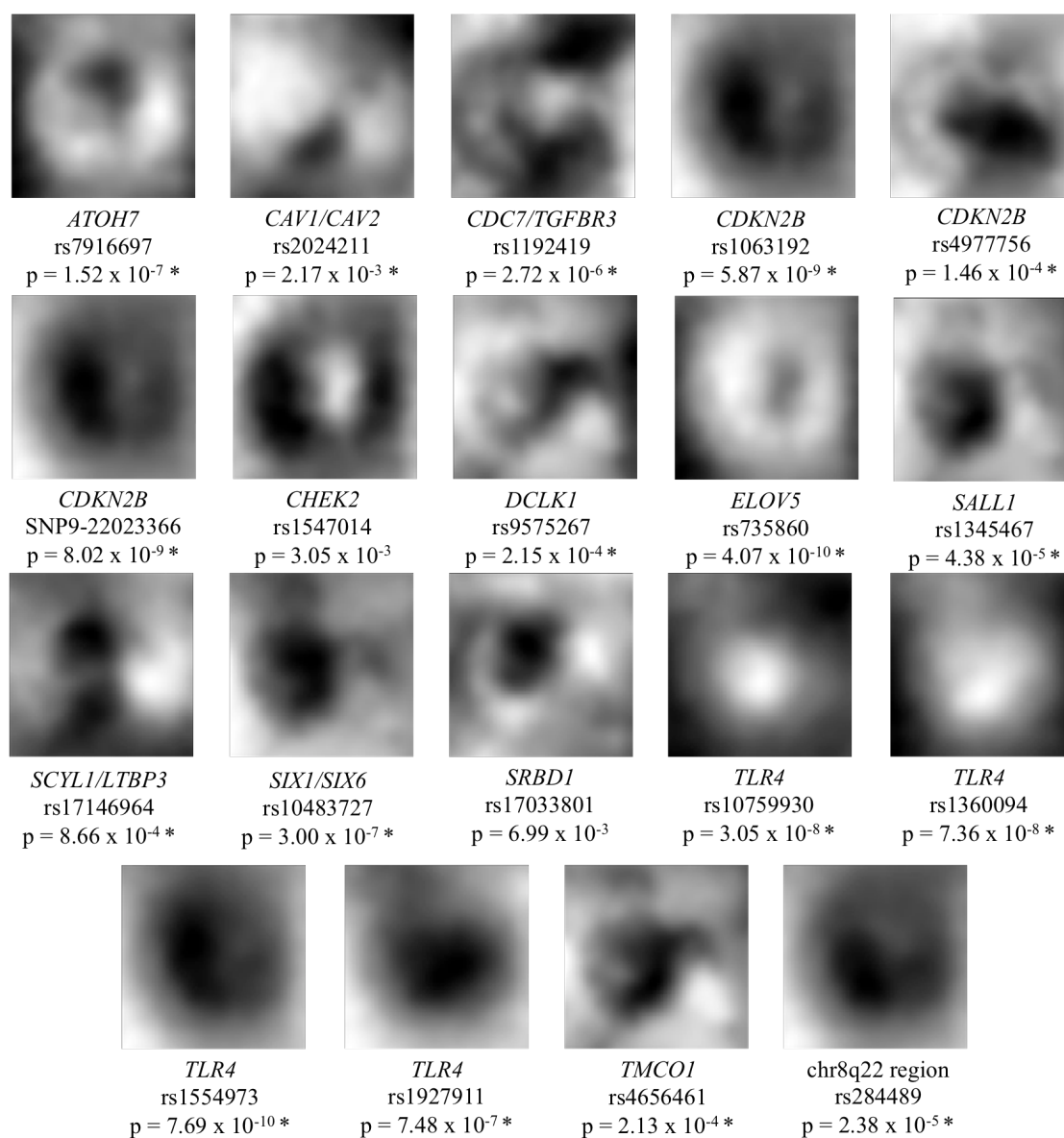


Figure 5.2: Gray-scale representations of the estimated effect of 19 POAG-related SNPs on ONH structure. Each is shown along with the gene in which the SNPs occur. The \* indicates the relationship between the estimated effect and SNP genotype is significant.



**A**

Gene (SNP)	POAG P-value	Gene (SNP)	POAG P-value	Gene (SNP)	POAG P-value
TLR4 (rs1360094)	$2.51 \times 10^{-8}$	CDKN2B (rs1063192)	$2.43 \times 10^{-6}$	TMC01 (rs4656461)	$1.75 \times 10^{-5}$
TLR4 (rs1554973)	$2.72 \times 10^{-7}$	chr8q22 (rs284489)	$3.17 \times 10^{-6}$	ELOVL5 (rs735860)	$1.23 \times 10^{-4}$
TLR4 (rs1927911)	$3.13 \times 10^{-7}$	SIX1/SIX6 (rs10483727)	$3.18 \times 10^{-6}$	SCYL1/LTBP3 (rs17146964)	$4.29 \times 10^{-4}$
CDKN2B (SNP9-22023366)	$1.80 \times 10^{-6}$	TLR4 (rs10759930)	$6.32 \times 10^{-6}$	CDKN2B (rs4977756)	$7.68 \times 10^{-4}$

**B**



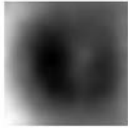


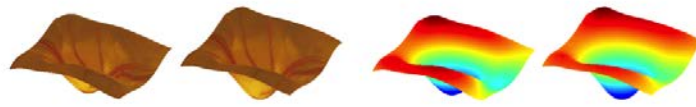
Gene/SNP	ONH Feature	Effect on ONH Structure
<i>TLR4</i> (rs1360094)		
<i>CDKN2B</i> (rs1063192)		
<i>SIX1 / SIX6</i> (rs10483727)		

Figure 5.3: Summary of the associations between genetic ONH structural features and POAG. (A) The full list of identified genetic features associated with POAG. (B) The effect on ONH structure for some of the most significantly associated features. The gray-scale feature is along with the effect on structure that results from increasing the influence of the feature.

identified, SNPs with significant associations to ONH structure were annotated to determine nearby protein-coding genes, known gene function, and previously published associations. These results serve to provide potential target genes for further research into the genetic contributors to ONH structure and POAG.

### Preprocessing and Quality Control

The raw genotyping data consisted of genotypes 905,636 SNPs collected for 1054 individuals using the Illumina 1M platform. Prior to any analysis, suggested best practices for quality control and data screening procedures were applied.[151] This included removing data from low quality SNPs and participant samples. SNPs were judged to be of low quality, and therefore removed from further analysis if they exhibited a genotyping rate of less than 98%. In addition, SNPs with a minor allele frequency of less than 5% in the genotyped OHTS cohort were also filtered out. A filter to exclude participants with low genotyping rates (<98%) was also applied, however, no participants were excluded based on this criterion. All participants also passed quality control filters that excluded those with a mismatch between annotated and genotyped sex, those falling outside of the reported ethnic groups, and those related to another participant. After this preprocessing, a set of 778,246 SNPs and 1054 participants remained. The quality control filtration and screening procedures were performed using the software PLINK.[152]

### Structural Endophenotype Association Testing

The first 10 STEPs that explained >95% of ONH structural variance were tested for association with each of the remaining SNPs. These associations were detected using ANOVA tests comparing STEPs to genotypes coded using an additive genetic model. For this analysis, ethnicity was controlled for by inclusion in the ANOVA test models.

Multiple hypothesis correction was applied to help filter out spurious associations. In addition to the standard GWAS issues with multiple hypothesis testing, the multiple phenotypic measurements (STEPS) under consideration further increased the number of tested hypotheses. Bonferroni correction is particularly conservative and can often lead to an unacceptable false negative rate in cases where the number of tests is extremely large. Instead, the commonly used false discovery rate (FDR) approach was employed to determine significance of associations between SNPs and STEPs.[153, 154] Under this

approach, significance is not determined with a p-value threshold intended to control the false positive rate, but by thresholding the q-value, the expected proportion of loci reported as significant that are truly unassociated (i.e. the FDR). For this analysis, the q-value threshold was set at 0.05, a level comparable those used in recent similar works.[155, 156]

Significant associations were identified with three of the STEPs (4, 6, and 8). Figure 5.4 illustrates the genome-wide significance of associations with these three STEPs. For STEP 4, significant results were observed at genomic regions near the SNPs rs6039368 ( $p = 5.99 \times 10^{-9}$ ), rs13261938 ( $p = 3.10 \times 10^{-8}$ ), rs765556 ( $p = 3.75 \times 10^{-8}$ ) and rs4974155 ( $p = 3.88 \times 10^{-8}$ ). Significant regions for STEP 6 were observed around the SNPs rs3181362 ( $p = 2.48 \times 10^{-9}$ ), rs10512474 ( $p = 8.27 \times 10^{-9}$ ), rs9518555 ( $p = 1.04 \times 10^{-8}$ ), rs2068621 ( $p = 2.76 \times 10^{-8}$ ), rs3774146 ( $p = 3.15 \times 10^{-8}$ ), rs955868 ( $p = 3.35 \times 10^{-8}$ ), rs2130628 ( $p = 3.88 \times 10^{-8}$ ), and rs7005971 ( $p = 4.63 \times 10^{-8}$ ). Finally, STEP 8 exhibited significant associations with regions near rs12323080 ( $p = 3.71 \times 10^{-9}$ ) and rs627530 ( $p = 4.77 \times 10^{-9}$ ). Table 5.2 lists the full set of significantly associated SNPs and nearby genes.

### Conclusions

The influence of genetic factors on ONH structure was investigated using two different approaches. The approaches included both directly modeling the impact of a small set of SNPs on the ONH as well as standard GWAS techniques. Applying both approaches helped provide depth to characterize specific changes in ONH structure imparted by individual loci and the breadth needed to discover associations from across the genome.

The use of STEP features and LDA-based modeling of genotype influence was able to identify a significant impact on ONH structure in 17 of the 19 SNPs considered here. The enrichment of these SNPs for associations with ONH structure is not surprising

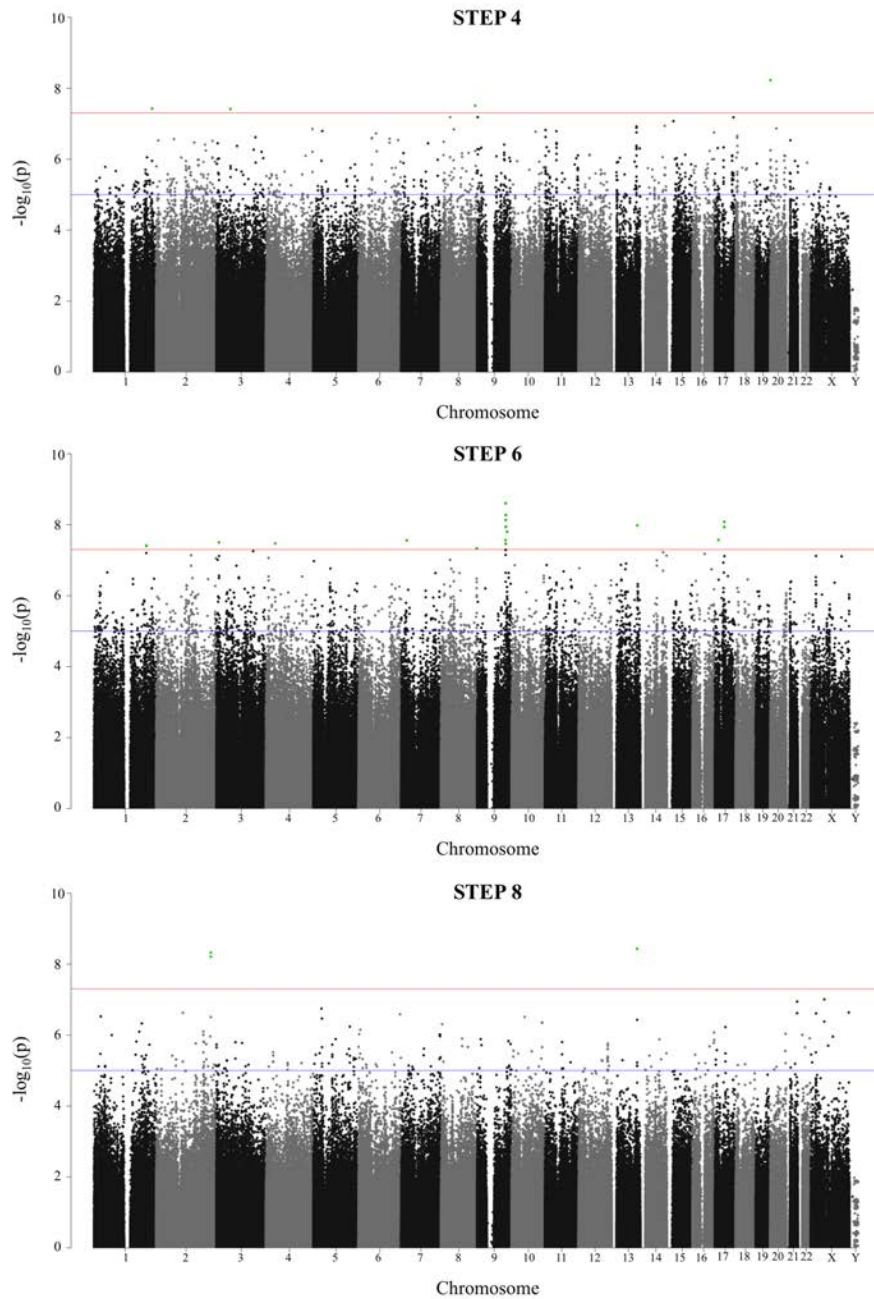


Figure 5.4: Manhattan plots summarizing the genome-wide significance of three STEPs. The blue and red lines indicate suggestive and significant associations, respectively. Significant results are also highlighted in green.

Table 5.2: Significant associations between STEPs and SNPs from across the genome.

<b>STEP – SNP Association</b>	<b>Chr</b>	<b>Position</b>	<b>P value</b>	<b>Gene</b>
<b>STEP 4</b>				
rs765556	1	232,874,306	3.75 x 10 <sup>-8</sup>	-
rs4974155	3	55,978,949	3.88 x 10 <sup>-8</sup>	<i>ERC2</i>
rs13261938	8	137,313,032	3.10 x 10 <sup>-8</sup>	-
rs6039368	20	977,236	5.99 x 10 <sup>-9</sup>	<i>RSPO4</i>
<b>STEP 6</b>				
rs2130628	1	210,118,130	3.88 x 10 <sup>-8</sup>	<i>SYT14</i>
rs10127635	1	210,121,138	3.94 x 10 <sup>-8</sup>	<i>SYT14</i>
rs3774146	3	10,419,478	3.15 x 10 <sup>-8</sup>	<i>ATP2B2</i>
rs955868	4	37,788,636	3.35 x 10 <sup>-8</sup>	-
rs2068621	7	23,114,681	2.76 x 10 <sup>-8</sup>	<i>KLHL7</i>
rs7005971	8	144,047,401	4.63 x 10 <sup>-8</sup>	<i>SMPD5</i>
rs1265891	9	114,347,831	2.72 x 10 <sup>-8</sup>	<i>TNFSF8</i>
rs3181362	9	114,905,162	2.48 x 10 <sup>-9</sup>	<i>TNFSF8</i>
rs3789882	9	114,907,418	5.36 x 10 <sup>-9</sup>	<i>TNFSF8</i>
rs7028089	9	114,915,544	1.14 x 10 <sup>-8</sup>	<i>TNFSF8</i>
rs3181360	9	114,929,277	7.32 x 10 <sup>-9</sup>	<i>TNFSF8</i>
rs3181192	9	114,932,813	3.45 x 10 <sup>-8</sup>	<i>TNFSF8</i>
rs846826	9	120,343,695	1.58 x 10 <sup>-8</sup>	-
rs9518555	13	101,796,939	1.04 x 10 <sup>-8</sup>	<i>FGF14</i>
rs6502352	17	14,402,972	2.68 x 10 <sup>-8</sup>	-
rs6607303	17	37,848,767	1.15 x 10 <sup>-8</sup>	-
rs10512474	17	37,863,708	8.27 x 10 <sup>-9</sup>	-
<b>STEP 8</b>				
rs681747	2	219,597,917	6.17 x 10 <sup>-9</sup>	<i>STK11IP</i>
rs627530	2	219,611,720	4.77 x 10 <sup>-9</sup>	<i>STK11IP</i>
rs12323080	13	101,391,223	3.71 x 10 <sup>-9</sup>	-

given that they have all exhibited strong evidence of association with POAG risk in previously published works. Importantly, though, the associations with POAG and any of these SNPs were not reproduced in the OHTS cohort, with only one (rs4656461 in the gene *TMCO1*) nearing the level of significance. Even lacking these SNP-POAG associations within the dataset, the structural features learned from the SNPs were associated with POAG in 12 of 19 cases. This is especially useful because, once trained, these features can be measured directly using only stereo fundus images. With only these image-derived measurements, information about both disease and the underlying genetics can be determined.

Modeling the impact of individual genetic loci has the potential to aid POAG research and treatment in several important ways. First, it allows the magnitude and type of structural impact of each locus to be determined, helping to characterize the expected genetic variation in structure. Second, with this impact identified, the structural effects of individual genetic loci could be controlled for to help eliminate confounding factors in researching environmental and disease-related changes to ONH structure. Finally, the loci that cause large or disease-related changes to the ONH potential may serve as therapeutic targets for POAG treatments.

Applying standard GWAS procedures to determine genetic associations to stereo fundus derived STEPs resulted in a number of significant results, the most convincing of which was an association between STEP 6 and SNPs near the gene *TNFSF8*. This gene codes for a membrane protein that plays an important role in the apoptosis (programmed cell death) pathway and has previously implicated in multiple cancer types. Expression experiments indicate that this gene is expressed in many ocular tissues including the optic nerve, however, its presence in any specific retinal cell type and its function therein remains unclear. Significant associations with *TNFSF8* and the other genes provide potential future gene targets for POAG research, evaluation in independent cohorts is needed to confirm these results.

Incorporation of additional cohorts may also help to reveal still hidden STEP-SNP associations. The significant results observed here did not overlap with previously published SNPs affecting POAG risk or ONH structural measurements. Suggestive (not significant) associations did exist in some of these cases, though, including STEP associations with *ATOH7* (rs7916697), *TLR4* (rs1360094), *SIX1/SIX6* (rs10483727), and *CDKN2B* (rs1063192). The relatively small size of the OHTS cohort relative to other GWAS experiments, which often incorporate more than 10,000 participants, may limit the ability to detect these associations at a statistically significant level.

While the techniques applied here were able to detect significant genetic effects on ONH structure, they were limited in that they only considered structural measurements derived from images taken at a single point in time. The ONH, of course, is not a static structure. It changes not only as a result of disease progression, but also as a function of age and possibly other as-of-yet undiscovered influences. Incorporating longitudinal measurements that capture this change over time may help to improve not only POAG prediction, but also reveal how genetic factor influence the effect of aging and disease progression on the ONH.

## CHAPTER 6

### LONGITUDINAL ANALYSIS OF ONH STRUCTURE

The analyses described up to this point have focused on clinical measurements and images collected at a single time point. These approaches are useful in identifying the types of variation observed with ONH structure and helped uncover associations with clinical measurements, genetic factors, and POAG. However, they lack the ability to capture time-dependent changes to ONH structure. In clinical settings, these changes are extremely important. A typical evaluation by a physician often includes comparisons of current ONH structure to previous measurements to identify any progressive changes indicating POAG. Computational analysis of these progressive changes could help uncover additional latent relationships between ONH structure and disease.

The OHTS dataset under consideration here contains an extensive longitudinal component that includes image collected at regular intervals as well as expert determinations of conversion to disease. This provides a unique opportunity to measure time-dependent changes in ONH structure and characterize those changes that are associated with POAG. This data can also be utilized to build and evaluate early prediction models to identify likely POAG cases before the onset of disease. Because early detection is crucial to preserving vision, these prediction models have the potential to make a large translational impact.

This chapter first describes the image processing and registration techniques that were needed to standardize a large image dataset collected over the course of more than a decade. Next, the methods and results for predicting the onset of disease and characterizing POAG-related changes based on longitudinal measurements of ONH structure are summarized.



### Dataset Description

The data used to investigate longitudinal changes to ONH structure were collected during the OHTS baseline and follow-up visits. Briefly, all participants exhibited elevated IOP, but were judged non-glaucomatous at baseline. Clinical measurements (IOP, CDR), stereo fundus images, and visual field tests were collected at regular follow-up visits. Incident POAG (conversion to POAG) was determined at follow-up visits based on ONH progression, visual field progression, or both. This OHTS cohort contained 1635 participants with imaging occurring at an average of 11.4 follow-up visits over 10.7 years. Table 6.1 summarizes the data considered during the analyses described in this channel. For a complete description of inclusion criteria, data collection, and POAG diagnosis procedures for OHTS, see Chapter 4.

Table 6.1: OHTS cohort demographics, longitudinal measurements, and disease status.

Measurement	Distribution	Description
Age	$62.0 \pm 10.1$ years	Age at imaging
Sex	56.4 % female	-
Ethnicity	71.2% white, 23.5% African American, 5.3% other	Self-reported participant ethnicity
HCDR	$0.41 \pm 0.21$	Horizontal cup-to-disc ratio
IOP	$20.35 \pm 4.59$ mmHg	Intraocular pressure
POAG	93.9 % Non-POAG	Diagnosed with POAG at time of imaging
POAG Modality	44.0 % ONH, 21.2 % visual field, 34.8 % both	The method used to diagnose POAG

An important challenge of analyzing this large fundus image dataset was the lack of a standardized imaging protocol. A variety of different cameras including those that capture stereo images simultaneously and those that capture them sequentially are

represented within the dataset. Generally, the fundus camera used to collect images was determined by the study center. Because participants tended to return to the same study center for all of their follow-up visits, all images for a single participant were collected using the same type of fundus camera in most cases. However, this was not the case for some participants and differences across fundus cameras needed to be addressed. The issues with camera type combined with differences in image quality, illumination, and ONH framing necessitated substantial pre-processing before ONH structural features could be identified.

### Longitudinal Fundus Image Registration

Before any analysis of the follow-up images could be performed, significant preprocessing was needed to ensure that equivalent measurements of ONH were being captured from each stereo image pair. Without these steps, useful comparisons of ONH structure within or across participants would be impossible. The following section will detail these steps that included a combination human annotation, automated processing, image registration.

### Baseline Annotation and Image Preprocessing

The baseline images for each of the 1635 OHTS participants were used as a reference to which later images could be aligned and compared. To this end, the right eye baseline image for each participant was manually annotated for ONH location. In addition to ONH annotation, the camera type used to capture each baseline image was recorded. These different camera types were identified by noting the shape of the mask used during capture and the overall image appearance. Review of the images resulted in identification of 11 distinct camera types represented in the dataset. For use during processing of the follow-up images, each participant was assigned a camera type using their baseline image. To help account for magnification differences in images captured using different cameras, the mean optic disc diameter was determined for each camera

type based on human annotations of disc diameter. These means were used to determine image scaling factors that were applied during later processing to ensure that images from each camera type had an equal mean optic disc diameter.

With the baseline images annotated and ready for use as a reference, processing of the follow-up images could be performed. The first step in this process was automated localization of ONH. Using the methods described in Chapter 3, a machine learning model for locating the optic disc was built and applied. The entire set baseline images and human annotations of ONH location were used a training set and the resulting model was applied to all follow-up images. Figure 6.1 shows an example application of the automated ONH localization to longitudinal images. While a region containing the ONH was extracted in the majority of cases, the ONH regions were not perfectly aligned. Errors in the ONH localization introduced noticeable translational errors across images from the same participant as well as across participants. Beyond horizontal and vertical translations, rotational and scaling differences also existed between these images. Differences in rotation could have been introduced by endo- or exorotation of the participant, variation in positioning of the camera, or positioning of the film slide during digitization. The magnification levels of the different cameras introduced scaling differences even within a single participant when the same camera type was not used for all follow-up images. Simple extraction of the ONH region could not account for these substantial differences between the images. To address these issues, a more sophisticated image registration approach was applied to bring the images into a standard format.

### Image Registration and Evaluation

Image registration is a wide and widely studied topic that is used in virtually every domain in which image data is analyzed. Broadly, image registration is a process in which different images of the same (or similar) scene(s) are compared to determine the

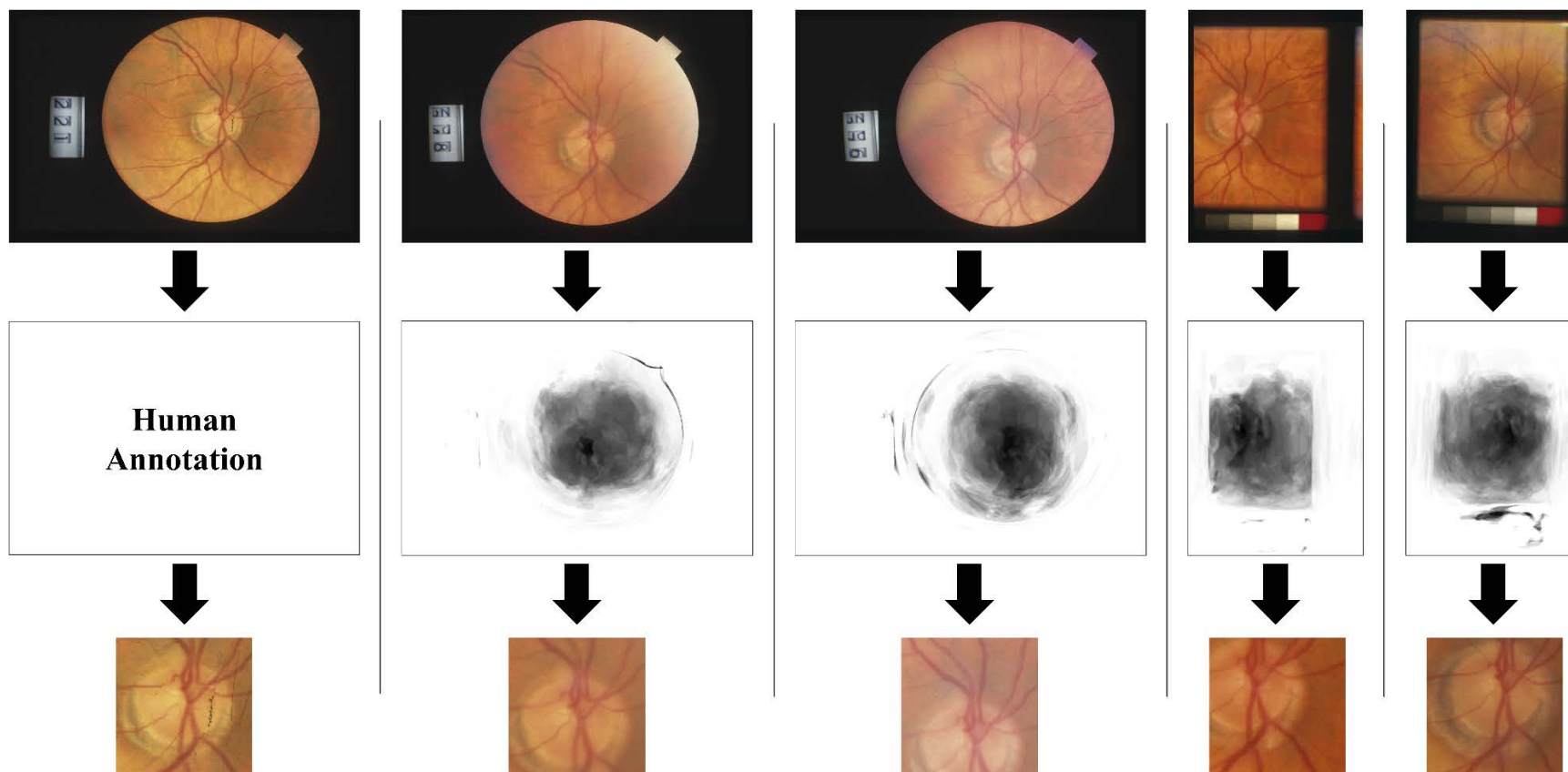


Figure 6.1: Example ONH extraction from longitudinally collected images. Each column illustrates the process for images collected from a single participant including the manually extracted ONH from the baseline (far left) and the automatically extracted ONH regions from follow-up images. The rows contain the input images (top), the ONH localization either through manual extract or probability maps generated automatically (middle), and the final extracted ONH (bottom). Note the vertical and horizontal translations associated with automated results and the change in image format resulting from different fundus cameras.

function by which points in one image can be mapped to points in another image given that those points correspond to the same position in the scene. There are a number of different approaches employed to address the task of image registration depending on the types of images considered and the image processing goals.[157] For the analysis described here, rigid image registration can be thought of as a generalized optimization procedure that searches through many different possible functions (transformations) that globally map one image onto another and attempts to identify the one that maximizes a similarity function comparing the two images. This high-level description leaves considerable room for customization and parameter selection so that the methods may be adapted to best fit the problem under consideration.

Registration of the OHTS images was performed by aligning images on a per participant basis. The baseline image for each participant was used as a reference to which each follow-up image was registered. The registration was performed in two steps. First, registration that allowed translational and rotational transformations was performed to align the ONH regions. Second, registration that allowed scaling transformations was applied to help account for differences between camera types. This two-step process was selected based on initial results on a few test cases. When a single-step registration that included scaling was used, the results contained large errors in aligning ONH regions.

Because it is difficult to predict exactly what type of registration methods and parameters will work best for a particular problem, a variety of different parameters and preprocessing steps were evaluated to determine those that worked best for the OHTS dataset. Table 6.2 summarizes the parameters and preprocessing steps that were evaluated.

The first evaluated parameter controlled the optimization step in the registration process by determining the similarity function used to compare images. Three possible similarity metrics including mean square difference, normalized correlation, and mutual information were evaluated.[158, 159] The mean square difference metric is computed by

averaging the squared differences between pixel values in the images being registered. This average difference value can be negated to indicate similarity (rather than distance) between two images. Normalized correlation is computed by calculating the Pearson's correlation coefficient between pixel values in the images. Finally, mutual information is a measure of statistical dependence between the pixel values of the two images. Similar images exhibited high statistical dependence (high mutual information) while dissimilar images are more statistically independent (low mutual information).

Table 6.2: The registration parameters and preprocessing steps that were evaluated.

<b>Parameter</b>	<b>Tested Values</b>	<b>Description</b>
Similarity Metric	Mean square differences, Normalized correlation, Mutual information	The image similarity function that is optimized during registration
Multi-scale Levels	1, 2, 3, 4	The number of scales in the multi-scale image representation. A value of 1 indicates only the original image is considered.
ONH Initialization	Yes, No	Indicates whether automated ONH estimation is used as initial registration estimate.
Threshold Masking	Yes, No	Indicates whether threshold mask is used to exclude image regions during registration.
Histogram Matching	Yes, No	Indicates whether histogram matching is used as a preprocessing step.
Channel	Red, Green, Blue, Luminance, Low-pass, Vessel Estimation	The image channel used to perform registration.

The second parameter helped guide the search for the optimal similarity metric values. Specifically, it determined if a multi-scale image representation was used to perform the registration. Briefly, a multi-scale representation adds an additional dimension to the image used to generate smoothed, rescaled versions of the image. This

can be useful because it allows the registration process to consider image structures of vastly different sizes (e.g. the optic disc vs. small vessels) separately. See Chapter 3 for more details regarding multi-scale image representations.

The automated ONH detection was also incorporated as a preprocessing step in the registration. First, an estimate of ONH location was computed for the follow-up image using the automated method described in Chapter 3. The horizontal and vertical differences between the annotated baseline ONH location and the estimated follow-up ONH location were used to compute a translational transform. This translation was then used as an initial transformation estimate for the registration process. Both registration schemes that included this initial estimate and those that did not were evaluated.

Several other possible registration preprocessing steps were also considered. The first determined whether a binary image mask was applied to help exclude areas outside of the fundus region prior further processing and registration. The mask was computed by applying an Otsu threshold to the image to determine which pixels fall outside the fundus region of the image. After thresholding, a morphological erosion operation was applied to the binary mask to help exclude fundus edge pixels and small non-fundus areas missed by thresholding. This final binary mask was used to exclude non-fundus areas from consideration during registration. Second, the use of histogram matching in which the pixel values of the follow-up image are transformed so that their distribution more closely matches that of the baseline image pixels was evaluated. This step was applied to help address differences in illumination and contrast between images. In both of these cases, both inclusion and exclusion of the preprocessing step was evaluated.

The final possible preprocessing steps determined the image channel that was used during registration. For this evaluation, an image channel referred not only to one of the standard red, green, or blue (RGB) color channels, but also the results of averaging or applying filters to the standard color channels. The additional channels considered included a luminance channel indicating overall brightness computed as a weighted

average of the RGB channels. Also included was a low pass channel that was computed by applying an averaging filter to the green channel. Finally, a vessel estimate channel was included. This channel was computed using a bank of Gabor filters to identify strong edges and ridge-like structures in the images. Specifically, a number of Gabor filters at several different scales and orientations were applied to the green channel of the image. At each pixel location, the maximum response across all scales and orientations was determined and used as the pixel value in the resulting image. This process emphasizes the strong edges associated with vasculature and suppresses flatter areas of the image. Figure 6.2 provides examples of each of these channels. Registration using each of these channels independently was evaluated to determine the one most suited for fundus registration.

Evaluation of parameter values and preprocessing steps was performed on a randomly selected subset of participants. This evaluation dataset consisted of 20 baseline and 215 follow-up stereo image pairs from 20 randomly selected participants along with human annotations of ONH location and optic disc diameter. Each possible set of parameters was used to perform registration on this evaluation set. The performance of each combination of parameters was determined by computing the average difference (in pixels) between the ONH center location and diameter across each participant. The combination resulting in the lowest average error was selected and used to align the full set of images. Figure 6.3 illustrates the effect of the tested parameters on the resulting registration quality. Based on these evaluations, the final methodology used the normalized correlation metric and a single level multi-scale representation during registration. Both automated ONH estimation and threshold masking were used as preprocessing steps. Finally, the vessel estimate channel was used for the registration. Figure 6.4 outlines the preprocessing and registration methods. The final registration scheme achieved a mean error corresponding to 4.1% of the average optic disc diameter



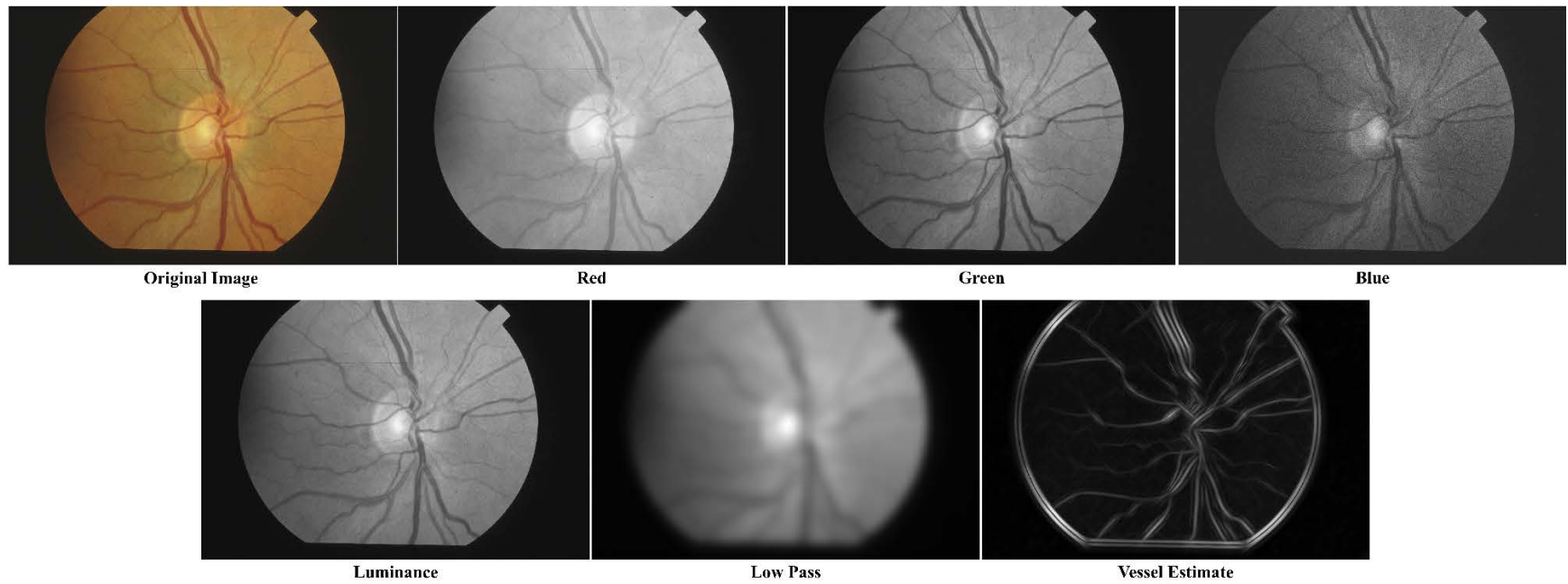


Figure 6.2: The image channels evaluated for use in registration. These included standard color channels (red, green, blue), a gray-scale channel (luminance), an average filtered channel (low pass), and a Gabor-based estimate of vasculature (vessel estimate).

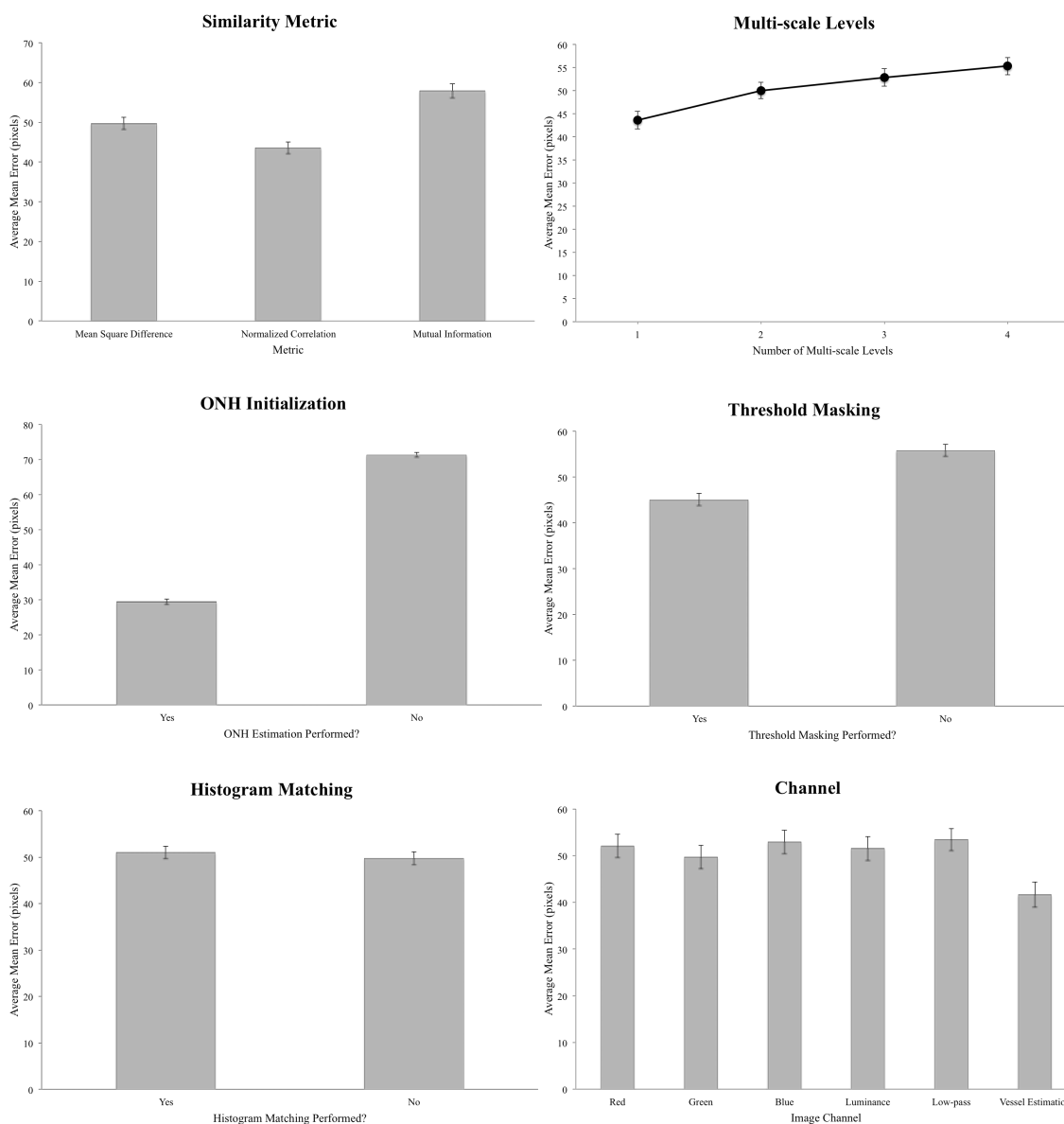


Figure 6.3: Effect of the evaluated parameters on registration quality. Providing an initial estimate using automated ONH detection made the single largest impact. The similarity metric, image channel, and application of a threshold-based mask had more modest impacts on performance. Using a multi-scale registration and performing histogram matching had little impact on final registration quality.

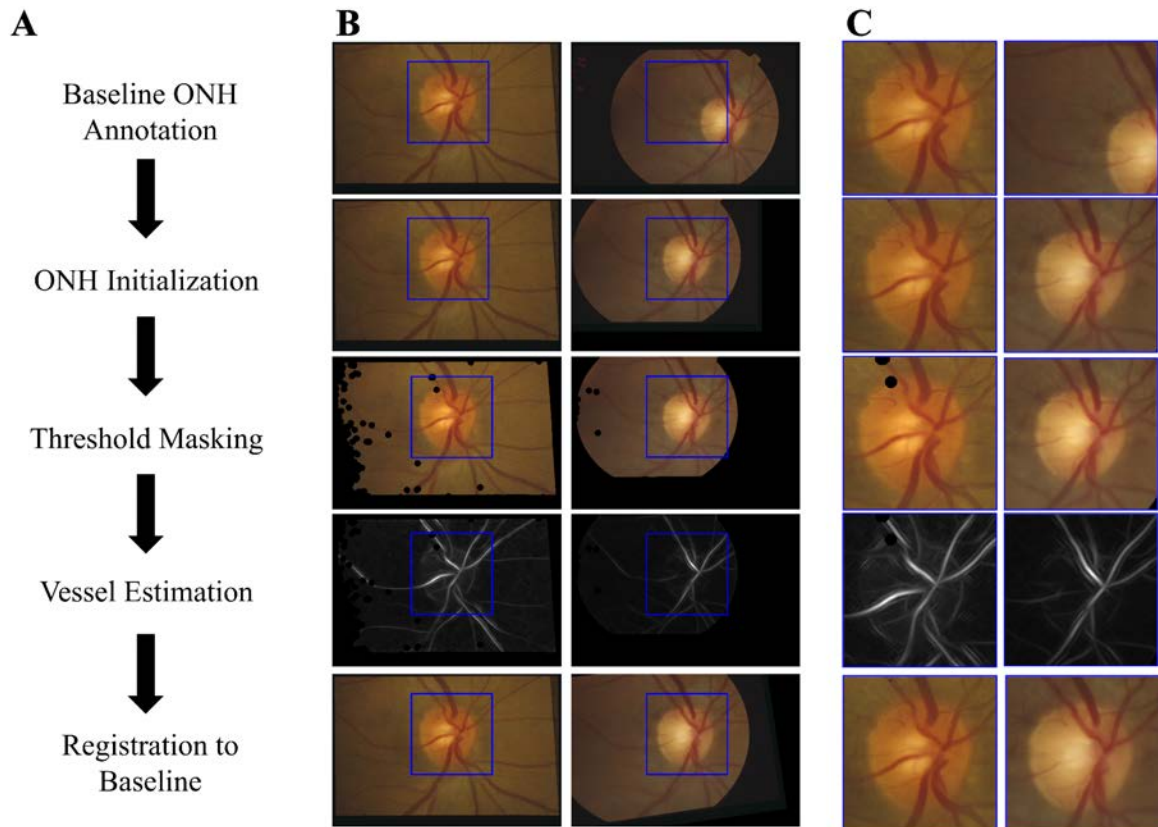


Figure 6.4: An outline of the process used to register follow-up to baseline images. (A) A flowchart of the major processing steps. (B) The baseline (left) and follow-up (right) after each step with the target ONH location highlighted in blue. (C) A magnified view of the ONH region after each step.

when aligning the follow-up fundus images to the baseline. The parameter evaluation and registration methods were implemented in C++ using the Insight Toolkit libraries.[101]

#### Individual Depth Map Analysis

With follow-up images registered to their corresponding baseline image, ONH structural measurements were computed for the entire OHTS dataset. Using the methods developed and evaluated in previous chapters, analyses were expanded to include this much larger dataset. The increased power of this sample and allows for previous results

to be confirmed and for novel relationships between ONH structure and POAG to be identified.

### Depth Inference and Structural Endophenotype Identification

Final input images to the depth inference algorithm were generated by extracting the ONH regions from all baseline and registered follow-up images using the annotated baseline ONH locations and camera types. This resulted in a set of 18,657 extracted ONH stereo pairs for the 1635 participants. All of these images were scaled to a common size (512 x 512 pixels) and had depth inference applied.

STEP identification was performed using the PCA-based methods described in Chapter 4. Briefly, each baseline depth map was preprocessed to reduce noise by applying Gaussian smoothing filter, cropping out a 25 pixel wide border to remove edge effects, and down-sampling to a size of 50 x 50 pixels. Normalization was performed by standardizing pixels values across the depth maps to have a zero mean and unit variance. Finally, PCA was applied to the entire set of depth maps to identify STEPs. The STEPs corresponding to the first 10 principal components are shown in Figure 6.5. The entire set of 18,657 depth maps were then projected onto this set of STEPs for further analyses.

### Clinical Measurement Prediction

The identified STEPs were evaluated based on associations with demographic variables (age, sex, ethnicity), clinical measurements (HCDR, IOP), and disease (POAG status at time of imaging). VCDR was not included because this measurement is only available for the baseline images. To perform association testing, STEP features were measured at all imaging time points (baseline and follow-up) for all participants. These STEP measurements were compared to all other measurements collected at the time of imaging. Tests for statistically significant associations were performed using linear regression in the case of quantitative measurements (age, HCDR, IOP) and ANOVA for

categorical measurements (sex, ethnicity, POAG status). Bonferroni correction was used to account for multiple hypothesis issues. Table 6.3 summarizes the significant results. As in the analysis of baseline features, significant associations were discovered between STEPs and age, ethnicity, and HCDR. Unlike the baseline analysis, significant associations were also detected between STEPs and IOP. Finally, several STEPs were also found to be associated with POAG status at the time of imaging.

Table 6.3: Significant associations between longitudinal measurements and STEPs.

Measurement	Significant STEP associations
Age	3, 4, 7, 8, 10
HCDR	2, 3, 4, 5, 6, 7, 8
IOP	3, 8
Ethnicity	3, 4, 7, 8
POAG	1, 4, 5, 10

### Longitudinal Changes to Structural Endophenotypes

The previous chapters and sections have considered only clinical or stereo-based STEP measurements captured at a single point in time. Of course, the ONH is not a static structure, but a dynamic one that changes based on aging, environment, and disease progression. Quantifying these time-dependent structural changes allows individuals to be characterized not by instantaneous measurements, but by the progressive changes to ONH structure observed over time. Given that clinicians often rely on structural changes, rather than individual observations, to diagnosis POAG, analyzing longitudinal measurements is key in identifying progressive changes associated with glaucomatous damage. The following sections will detail the methodologies employed to extract, analyze, and evaluate longitudinal structural features.

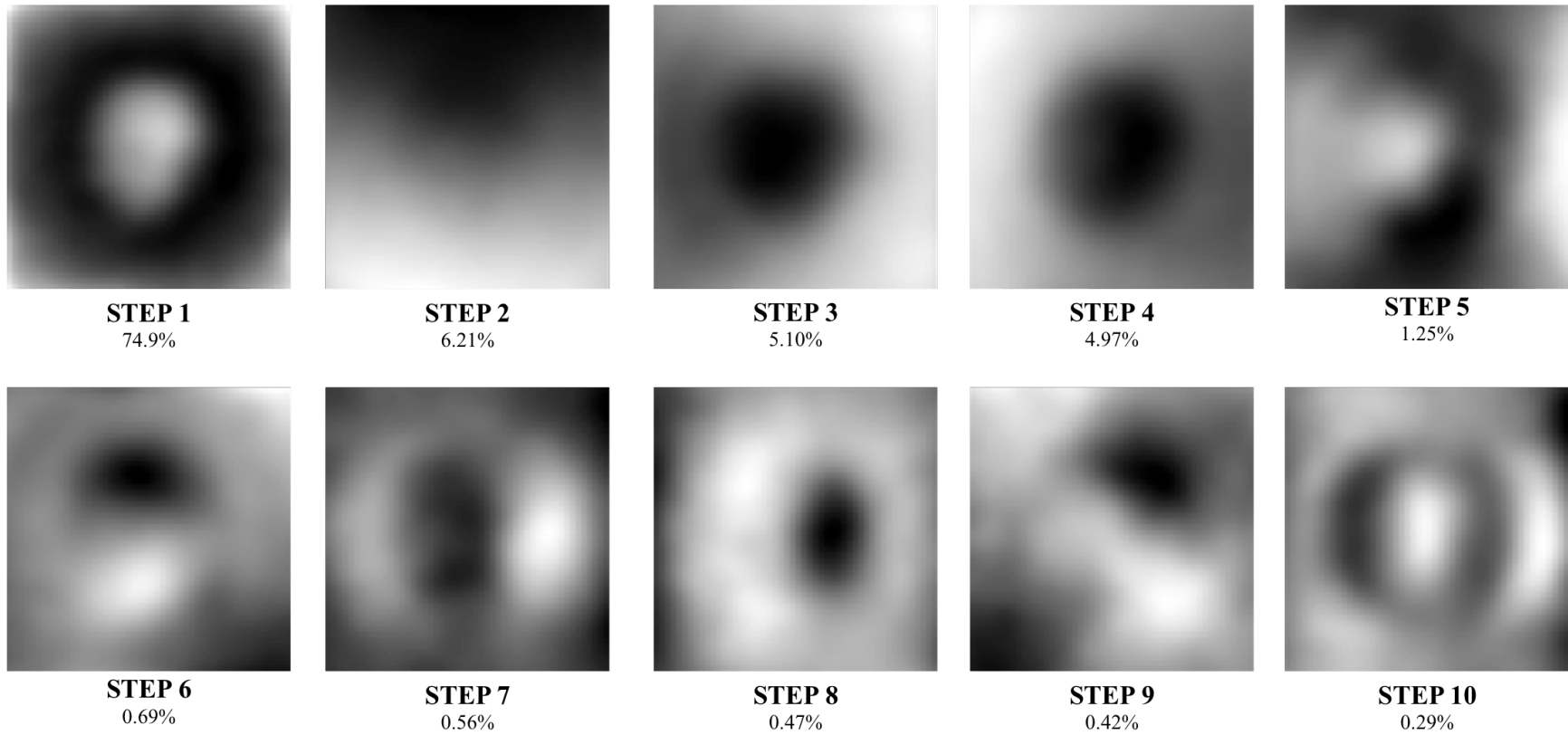


Figure 6.5: Gray-scale representation of the ten PCA-based STEPs identified using baseline data and applied in the analysis of the entire set of 18,657 baseline and follow-up images collected over the course of the OHTS.

### Longitudinal Measurement Preprocessing

For the analyses described here, the clinical measurements under consideration consisted of age, IOP, and HCDR each captured at baseline and follow-up visits for all participants. Stereo images captured at baseline and follow-up visits were also used to extract STEP measurements of ONH structure. Here, the measurements of a single clinical variable or STEP feature collected at all visits for a single participant will be referred to as a time series. The dataset consisted of time series for all clinical and STEP measurements for each participant.

Prior to analysis of the time series data, preprocessing was required to extract a standard set of measurements from each participant. While the OHTS data collection protocol did call for annual imaging and clinical evaluation, this collection did not control for participant age and consistent annual visits were not possible for much of the cohort. Participant availability, scheduling issues, and other practical concerns caused many annual visits to be delayed for months or missed altogether. Additionally, not all individuals continued to participate throughout the entire length of the study. These issues meant that the time series for both the clinical and STEP measurements were not consistently sampled regular intervals and covered varying lengths of time.

To account for these inconsistencies, a methodology for extracting data at regular intervals over a predetermined length of time was developed. First, an exclusion criterion was applied to ensure that data was available across the entire time period for all considered participants. Specifically, participants were required to have follow-up measurements and images for at least 10 years after baseline. After applying the criteria, 1246 participants remained under consideration. Second, to address the inconsistent sampling intervals, an interpolation and smoothing procedure was applied to estimate clinical and STEP measurements at a consistent set of time points. The interpolation scheme applied here was the LOESS method.[160] This interpolation fit a local linear regression model that estimated interpolated values by considering the closest observed

values. Using this interpolation method, the value of each clinical and STEP measurement was estimated at time zero (baseline) and at each one year interval for 10 years in all participants. This resulted in time series data for 1246 participants that were sampled at consistent one-year intervals for 10 years. These series included measurements of HCDR, IOP, and STEPs 1 through 10.

With preprocessing of the time series data accomplished, the use of longitudinal measurements of ONH structure to capture disease-related changes could be explored. To determine if structural changes associated with POAG could be captured using longitudinal STEP measurements, the time series data were used to predict disease outcomes. In these analyses, POAG modality (see Table 6.1) was mapped to a class variable indicating whether each participant was diagnosed with POAG based on expert evaluation of the ONH. A total of 101 out of 1246 participants exhibited these POAG-associated changes to ONH structure. Figure 6.6 illustrates average time series of normal and POAG individuals considered here.

#### Longitudinal Features in Disease Detection

The longitudinal clinical and STEP feature were first evaluated based on their ability to detect individuals that converted to POAG during the 10-year period covered by the time series measurements. To perform this evaluation, time series measurements of HCDR, IOP, and STEPs 1 through 10 were mapped to feature vectors that contained the measurements at baseline and follow-up visits for 10 years. The time series features were augmented with the demographic features of age, sex, and ethnicity leading to a total of 135 predictive features. This set of annually-sampled features were evaluated based on ability to detect individuals that converted to POAG based on expert ONH evaluation during 10 years of follow-up visits.



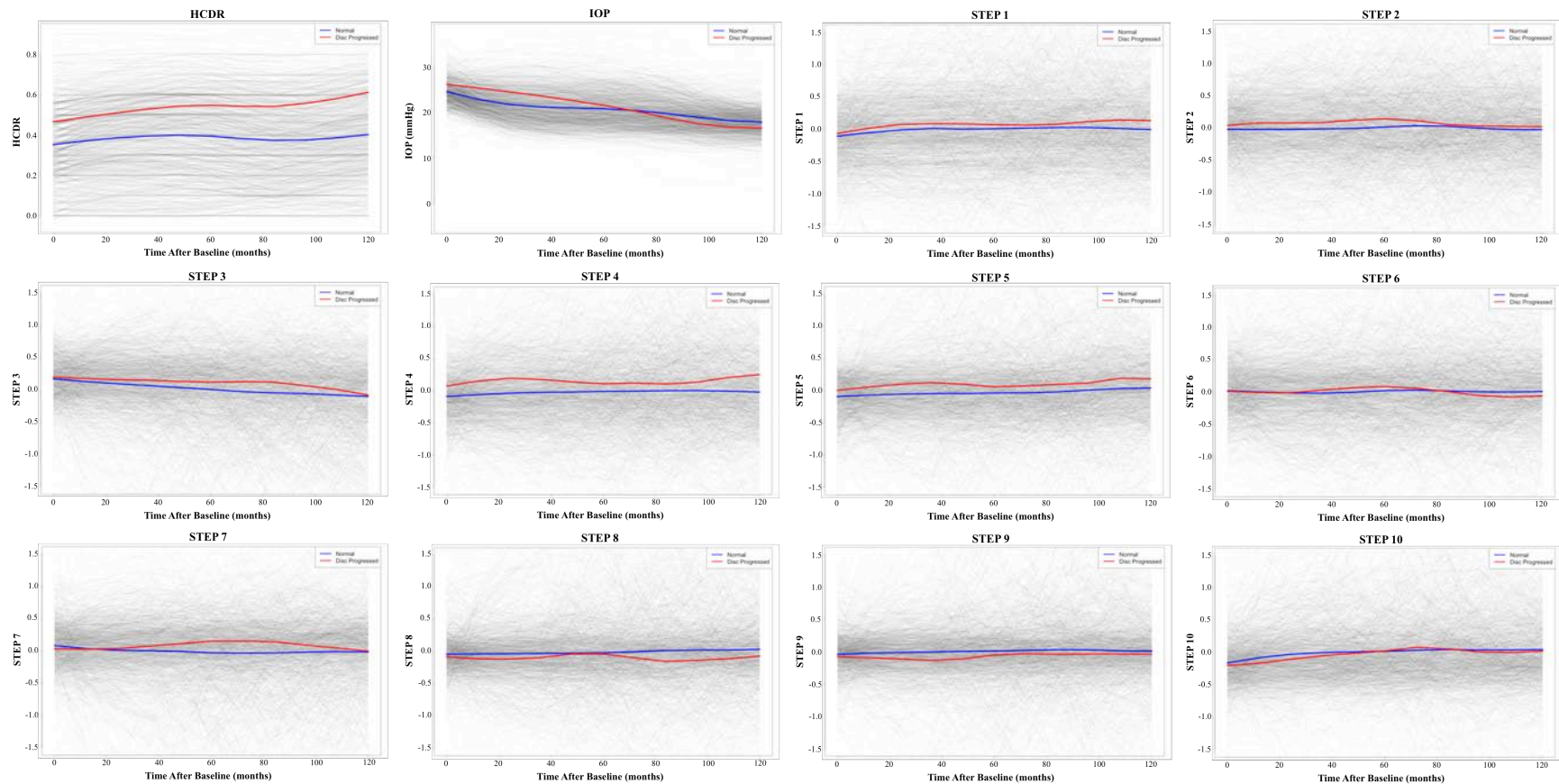


Figure 6.6: Longitudinal data collected from the OHTS cohort. Each graph shows 10 years of clinical (HCDR, IOP) or STEP measurements measured using stereo images. Each gray line represents the measurements collected from a single participant, blue lines indicate average measurements for normal participants, and red lines indicate the average of participants diagnosed with POAG based on expert review of stereo photos.

In addition to the straightforward mapping of each annual measurement to a predictive feature, a more sophisticated approach to compute predictive features from time series data was evaluated. This mapping used dynamic time warping (DTW), which is a technique commonly used in analysis of time series to help account for shifting and scaling in the time dimension when comparing two time series.[161] DTW uses a dynamic programming approach similar to alignment of biological sequences to align time series data and can be used to compute pairwise distances between aligned time series.[161] In the OHTS cohort, participants were recruited from a large range of ages (40 to 80 years) and, for those eventually progressing to POAG, time to diagnosis varied greatly (~1 to ~14 years). These large differences in age and speed of progression limit the ability of straightforward comparisons of time series to distinguish between normal and POAG individuals. DTW, however, is designed to help address such shifting, stretching, or compressing in time. In application to the OHTS data, DTW was used to quantify how similarly the measurements of a feature progressed over time across participants. For instance, to measure the similarity in IOP progression over time between two participants, DTW time warping was applied to align the two IOP time series and then quantify the similarity between the aligned time series. Figure 6.7 illustrates an example DTW alignment of STEP time series of two OHTS participants.

To compute predictive features from the OHTS time series data using DTW, it was applied to obtain pairwise distances between participants using each longitudinal measurement (HCDR, IOP, STEPs 1-10). The resulting pairwise distances were normalized to have zero mean and unit variance. To obtain a set of predictive features using these distance values, multidimensional scaling was applied. This technique computes a feature space in which the Euclidean distances between data points are equivalent to those given in an input set of pairwise distances.[162] It has been previously used in conjunction with DTW and biological sequence alignment to generate

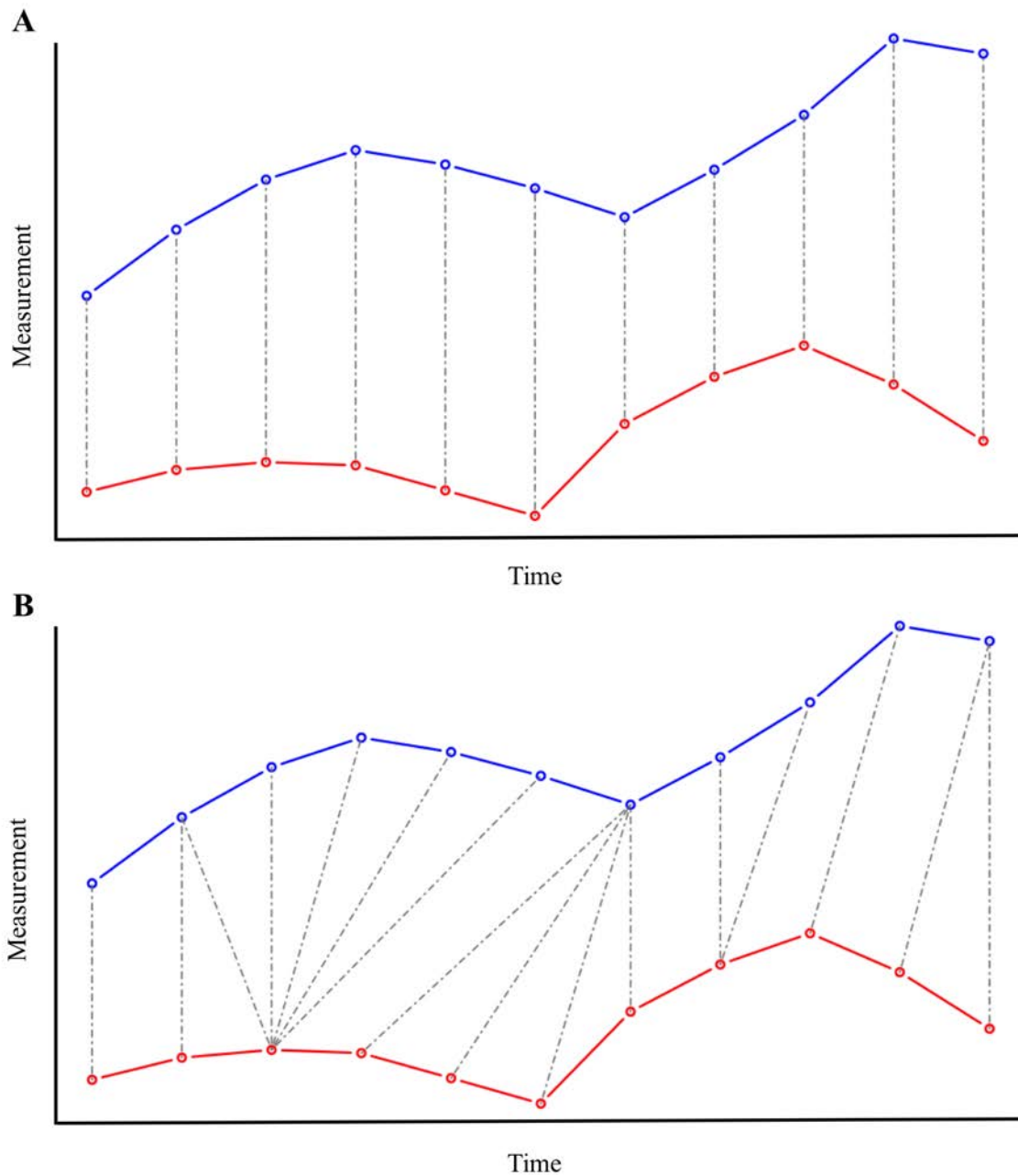


Figure 6.7: An illustration of time series alignment using dynamic time warping. **(A)** Without alignment, quantifying the similarity across time series data relies only on the comparing points captured at the same point in time and can be confounded by shifting or stretching one series with respect to another. **(B)** Alignment accounts for these differences by identifying similar regions across the series regardless of their position in time.

features used in visualization, clustering, and classification.[163, 164] For the analyses described here, R implementations of DTW and multidimensional scaling were used to extract predictive features from time series alignments.[161] The DTW-derived features were also augmented with demographic features (age, sex, ethnicity) and evaluated based on ability to detect progression to POAG.

The two feature sets described above (annually-sampled and DTW-derived features) were both incorporated into machine learning models used to identify the participants who developed POAG during the 10 year period considered here. Testing of several classification models including logistic regression,  $k$  nearest neighbor, support vector machines, and random forests was performed using AUC as the performance metric. For this task, random forest classifiers achieved the greatest accuracy. Further parameter optimization led to the use of random forests consisting of 100 trees in detecting and predicting POAG. Final performance was estimated using 10-fold cross validation testing. The annual-sampled features resulted in an AUC of 0.828 in detecting individuals that converted to POAG, while the DTW-derived features resulted an AUC of 0.845.

#### Longitudinal Features in Disease Prediction

Beyond characterizing the ability of longitudinal STEP features to detect POAG progression, these features were evaluated based on their ability to predict disease prior to any diagnosis. To perform this analysis, the subset of participants ( $n = 49$ ) that did convert to POAG and for which five or more years of data prior to conversion was available was identified. The five years of data immediately prior to POAG diagnosis was extracted for each and these time series data were used as positive examples of POAG. To provide negative examples, a set of non-glaucomatous individuals ( $n = 555$ ) was randomly selected. The time series covering a randomly selected, consecutive five-year period for each individual was then extracted. The number of individuals in each group

(49 POAG, 555 normal) was chosen to maintain the proportion of POAG participants relative to the full longitudinal sample (101 POAG, 1145 normal).

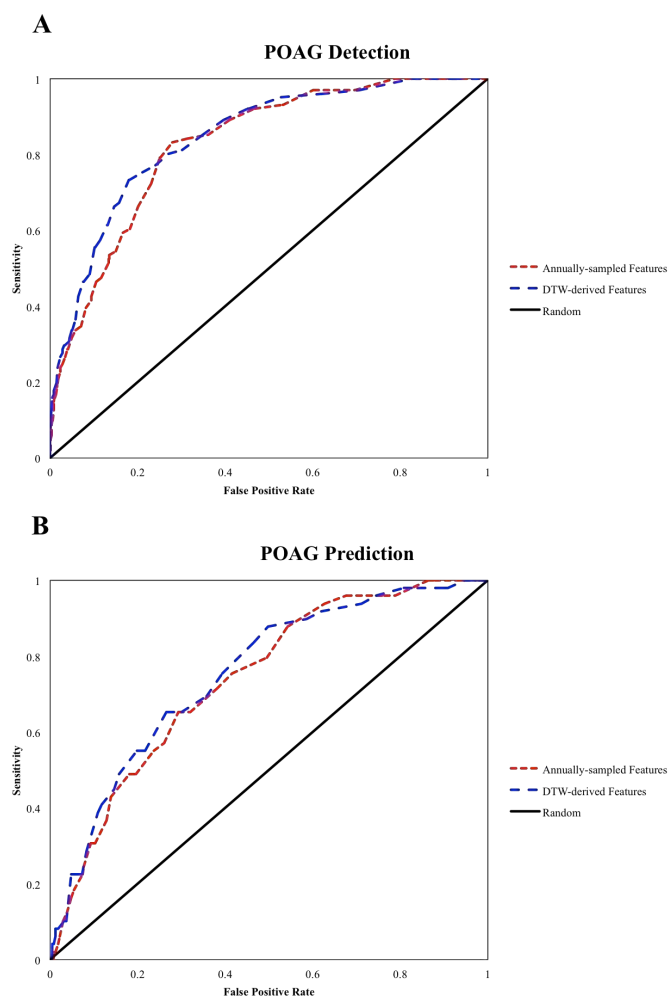


Figure 6.8: ROC curves resulting from time-series data to (A) detect progression to POAG using all longitudinal data and (B) predict POAG using only data collected prior to diagnosis.

Using this subset, the annually-sampled and DTW-derived features were computed using five years of time series data and then used to predict the POAG conversion. As in the analysis described above, random forest models were used to

perform prediction. Here, the annually-sampled features resulted in an AUC of 0.738 and DTW-derived features resulted in 0.752. Figure 6.8 shows ROC curves the results of using longitudinal features for detecting and predicting onset of POAG.

### Conclusions

Methods for identifying ONH structural features using stereo fundus images were applied to a large, longitudinal dataset. The methods presented in this chapter build upon the features identified by analysis of baseline data and show that incorporation of longitudinal measurements of ONH structural aid in the detection of POAG-related structural changes and early prediction of disease.

To enable the longitudinal analysis of ONH structure, a registration scheme that aligned fundus images taken over the course of roughly a decade was developed and evaluated. To optimize the performance of this scheme, several parameters and preprocessing steps were evaluated based on their impact on registration quality. The final methodology was able to register sequential fundus images with a mean error equivalent to 4.1% of optic diameter. This level of accuracy allowed for comparable structural measurements to be captured from longitudinal images collected over the course of more than a decade. The ability to computationally track ONH structural changes over time provides a unique opportunity to characterize the type of changes that the ONH undergoes during aging and identify those changes that are associated with glaucomatous onset and progression.

The structural measurements identified using the OHTS dataset were evaluated based on associations with demographics, clinical measurements, and disease state at the time of imaging. Supporting previous results, the STEPs were significantly associated with demographic features known to affect POAG risk (age, ethnicity) as well as clinical features used to diagnose and track POAG progression (HCDR, IOP). And, importantly, STEPs were once again shown to be associated with development on POAG.

The progression of clinical and STEP measurements over time was also investigated using the longitudinal data. Preprocessing methodologies were developed to extract measurements regularly-sampled over the course of a decade from the OHTS cohort. Using features derived from the time series data showed promising predictive power for detecting conversion to POAG (AUC = 0.845) and for predicting the onset of disease prior to diagnosis (AUC = 0.752). Unsurprisingly, the predictions based on these longitudinal features outperformed predictions based solely on baseline data (AUC = 0.722, see Chapter 4), supporting the importance of tracking the progression of ONH structural changes rather than relying on a measurements collected at a single point in time.

In conclusion, methods for processing stereo fundus images captured over several years were developed and evaluated. These methods allowed computationally-identified features of ONH structure to be captured longitudinally and used to predict conversion to POAG. The results show that quantifying changes to these features as well as standard clinical measurements increases the ability to detect POAG before functional loss has occurred.

## CHAPTER 7

### CONCLUSION

The work presented in this thesis uses a variety of computational methods to quantify ONH structure and uncover relationships that help determine this structure and how it changes over time. This included methods from the domains of image analysis, statistics, machine learning, genetics, and bioinformatics. Incorporation of such a broad array of techniques into the analysis of the uniquely rich OHTS dataset revealed novel associations between ONH structure, clinical measurements, genetics, and glaucoma.

Previous research into POAG suggests that it is a particularly difficult disease to study. This difficulty stems from the diverse ways in which this disease can present clinically as well as the complexity of the underlying genetics that play a large role in the disease. While there are clear associations between some measurable factors and POAG risk (age, IOP), these factors are not sufficient, either alone or in concert, to reliably predict the occurrence of disease. Similarly, there are known POAG causing mutations within some genes (*MYOC*, *OPTN*), but the majority of POAG heritability remains unexplained. These continuing difficulties suggest that new approaches to studying POAG may help to increase overall understanding of the disease.

Before any computational analysis of ONH structure could be performed, however, the diverse set of stereo fundus images represented within the OHTS dataset had to be processed so that consistent measurements of ONH structure could be collected. To this end, previously published methods were adapted for use on the data under consideration here. First, an automated ONH detection method was implemented to eliminate the need for human annotation in identifying the ONH region in fundus images. Evaluation of this method showed that it achieved greater than 90% accuracy in identifying the center of the optic disc, making it a useful tool for automating ONH extraction.



The second method adapted and implemented for use here was an algorithm for inferring depth information from stereo fundus images. This tool was crucial to all analyses presented in this thesis. It is by using this method that quantitative measurements of ONH structure in the form of depth maps were able to be collected. This method was inspired by general methods used to infer depth from stereo, but addresses several issues specific to fundus imaging. Previous works has shown that this method outperforms even state-of-the-art depth inference approaches when applied to fundus images. Results presented here have also shown that comparisons to OCT images, which provide a more direct measurement of ONH structure, exhibited high agreement with the measurements inferred from stereo.

With computational tools for quantifying ONH structure using stereo fundus images in hand, an analysis of a large participant cohort at-risk for developing POAG could be undertaken. Using stereo fundus images, clinical measurements, and disease outcomes, descriptive structural endophenotypes (STEPs) of ONH structure were identified and evaluated. These features explained >95% of variance observed in ONH features and were significantly associated with several clinical measurements commonly used to diagnose and monitor POAG. Further, these features increased the ability to POAG development years before diagnosis.

The quantitative STEPps identified from the OHTS cohort were then used to study the impact of genetic factors on ONH structure. In searching genome-wide associations with ONH structure, the use of STEPps revealed several novel significant associations. When considered in detail, STEPps allowed the impact of individual genetic loci on ONH structure to be estimated. The resulting features were significantly associated with both the corresponding genetic factors, but also with disease.

The longitudinal component of the OHTS dataset also allowed for the changes to ONH structure that occur within an individual over time to be quantified. A registration methodology that enabled sequential fundus images gathered from a single individual

over the course of more than decade to be aligned and comparable measurements of ONH structure to be captured was developed and evaluated. Using this methodology, the longitudinal OHTS data (~18,000 images) could be analyzed. As in the baseline analysis, a small number of STEPs were able to effectively capture a vast majority of variance observed with ONH structure. Analysis of this much larger dataset supported results obtained using on baseline data. STEP measurements computed from stereo images were significantly associated with clinical measurements and disease state at the time of imaging.

Methods for quantifying the change in both clinical measurements and STEP features occurring within individuals over time were developed and evaluated. These methods used longitudinal measurements and images collected from the OHTS cohort to describe the progressive changes to ONH structure occurring over the course of a decade. Machine learning models built using longitudinal features were able to detect conversion to POAG using the full range of available longitudinal data. Further, these models were found to be predictive of POAG even when built using only data collected prior to the onset of disease and had an increased power to predict POAG compared to models built using only baseline data.

Going beyond the analyses presented here, there are several possible directions for future work. For instance, clustering analysis of STEP features could help reveal clinically-relevant subtypes of ONH structure. Given the heterogeneity observed in POAG, clustering analysis using STEP features may to separate the complex problem of characterizing the relationship between ONH structure and POAG into a number of simpler tasks. Applying clustering techniques could be useful in identifying motifs in ONH structure both using single time-point measurements as well as in characterizing longitudinal changes to ONH structure.

Another possible direction for future work is the incorporation of longitudinal features into the identification of genetic contributors to ONH structure. These two

analyses were performed independently in Chapters 5 and 6, but a combined analysis could reveal how genetics impact the changes that occur to ONH structure over time. The results of such an analysis could have important implications for assessing risk of POAG and identifying those patients who are likely to exhibit accelerated disease progression.

The goal of the work presented here was to apply computational methods to increase understanding of ONH structure and its relationship with POAG. In applying these techniques, novel structural features were identified and used to predict the onset of disease. Additionally, the features were shown to be useful characterizing variations in ONH structure that occur over time and as a result of genetics. These results suggest that the methods presented here could be useful in both clinical settings to identify POAG before loss of vision and research settings as a tool to model the impact of related factors on ONH structure.

## REFERENCES

- [1] M. C. Leske, "The epidemiology of open-angle glaucoma: a review," *Am J Epidemiol*, vol. 118, pp. 166-91, Aug 1983.
- [2] M. Gemenetzi, Y. Yang, and A. J. Lotery, "Current concepts on primary open-angle glaucoma genetics: a contribution to disease pathophysiology and future treatment," *Eye (Lond)*, vol. 26, pp. 355-69, Mar 2012.
- [3] J. Charlesworth, P. L. Kramer, T. Dyer, V. Diego, J. R. Samples, J. E. Craig, *et al.*, "The path to open-angle glaucoma gene discovery: endophenotypic status of intraocular pressure, cup-to-disc ratio, and central corneal thickness," *Invest Ophthalmol Vis Sci*, vol. 51, pp. 3509-14, Jul 2010.
- [4] W. D. Ramdas, L. M. van Koolwijk, M. K. Ikram, N. M. Jansonius, P. T. de Jong, A. A. Bergen, *et al.*, "A genome-wide association study of optic disc parameters," *PLoS Genet*, vol. 6, p. e1000978, Jun 2010.
- [5] D. P. Dimasi, K. P. Burdon, A. W. Hewitt, J. Fitzgerald, J. J. Wang, P. R. Healey, *et al.*, "Genetic investigation into the endophenotypic status of central corneal thickness and optic disc parameters in relation to open-angle glaucoma," *Am J Ophthalmol*, vol. 154, pp. 833-842 e2, Nov 2012.
- [6] M. Christopher, L. Tang, J. H. Fingert, T. E. Scheetz, and M. D. Abramoff, "Changes in quantitative 3D shape features of the optic nerve head associated with age," *SPIE Med Imaging*, vol. 8670, 2013.
- [7] L. Tang, T. E. Scheetz, D. A. Mackey, A. W. Hewitt, J. Fingert, Y. H. Kwon, *et al.*, "Automated Quantification of Inherited Phenotypes from Color Images: a Twin Study of the Variability of the Optic Nerve Head Shape," *Invest Ophthalmol Vis Sci*, vol. 51, pp. 5870-5877, 2010.
- [8] H. A. Quigley and A. T. Broman, "The number of people with glaucoma worldwide in 2010 and 2020," *Br J Ophthalmol*, vol. 90, pp. 262-7, Mar 2006.
- [9] M. O. Gordon, J. A. Beiser, J. D. Brandt, D. K. Heuer, E. J. Higginbotham, C. A. Johnson, *et al.*, "The Ocular Hypertension Treatment Study: baseline factors that predict the onset of primary open-angle glaucoma," *Arch Ophthalmol*, vol. 120, pp. 714-20; discussion 829-30, Jun 2002.
- [10] J. M. Tielsch, A. Sommer, J. Katz, R. M. Royall, H. A. Quigley, and J. Javitt, "Racial variations in the prevalence of primary open-angle glaucoma. The Baltimore Eye Survey," *JAMA*, vol. 266, pp. 369-374, 1991.
- [11] C. Cedrone, R. Mancino, A. Cerulli, M. Cesareo, and C. Nucci, "Epidemiology of primary glaucoma: prevalence, incidence, and blinding effects," *Prog Brain Res*, vol. 173, pp. 3-14, 2008.
- [12] M. A. Kass, D. K. Heuer, E. J. Higginbotham, C. A. Johnson, J. L. Keltner, J. P. Miller, *et al.*, "The Ocular Hypertension Treatment Study: a randomized trial determines that topical ocular hypotensive medication delays or prevents the onset of primary open-angle glaucoma," *Arch. Ophthalmol*, vol. 120, pp. 701-713, 2002.
- [13] M. O. Gordon and M. A. Kass, "The Ocular Hypertension Treatment Study: design and baseline description of the participants," *Arch Ophthalmol*, vol. 117, pp. 573-83, May 1999.
- [14] A. Sommer, J. M. Tielsch, J. Katz, H. A. Quigley, J. D. Gottsch, J. Javitt, *et al.*, "Relationship between intraocular pressure and primary open angle glaucoma among white and black Americans. The Baltimore Eye Survey," *Arch Ophthalmol*, vol. 109, pp. 1090-5, Aug 1991.
- [15] B. E. Klein, R. Klein, W. E. Sponsel, T. Franke, L. B. Cantor, J. Martone, *et al.*, "Prevalence of glaucoma. The Beaver Dam Eye Study," *Ophthalmology*, vol. 99, pp. 1499-504, Oct 1992.

- [16] E. G. Society, *Terminology and Guidelines for Glaucoma*, 4th ed., 2014.
- [17] J. T. Schwartz, F. H. Reuling, and M. Feinleib, "Size of the physiologic cup of the optic nerve head. hereditary and environmental factors," *Arch Ophthalmol*, vol. 93, pp. 776-8, Sep 1975.
- [18] O. C. Holm, B. Becker, C. F. Asseff, and S. M. Podos, "Volume of the optic disk cup," *Am J Ophthalmol*, vol. 73, pp. 876-81, Jun 1972.
- [19] J. B. Jonas, G. C. Gusek, and G. O. Naumann, "Optic disc, cup and neuroretinal rim size, configuration and correlations in normal eyes," *Invest Ophthalmol Vis Sci*, vol. 29, pp. 1151-8, Jul 1988.
- [20] E. M. Hoffmann, L. M. Zangwill, J. G. Crowston, and R. N. Weinreb, "Optic disk size and glaucoma," *Surv Ophthalmol*, vol. 52, pp. 32-49, Jan-Feb 2007.
- [21] W. M. B. Jost B Jonas, Songhomitra Panda-Jonas, "Ophthalmoscopic Evaluation of the Optic Nerve Head," *Survey of Ophthalmology*, pp. 43: 293-320, 1999.
- [22] W. J. Feuer, R. K. Parrish, J. C. Schiffman, D. R. Anderson, D. L. Budenz, M. C. Wells, *et al.*, "The Ocular Hypertension Treatment Study: reproducibility of cup/disk ratio measurements over time at an optic disc reading center," *Am.J.Ophthalmol.*, vol. 133, pp. 19-28, 2002.
- [23] R. Watkins, L. Panchal, J. Uddin, and P. Gunvant, "Vertical cup-to-disc ratio: agreement between direct ophthalmoscopic estimation, fundus biomicroscopic estimation, and scanning laser ophthalmoscopic measurement," *Optom Vis Sci*, vol. 80, pp. 454-9, Jun 2003.
- [24] R. Varma, W. C. Steinmann, and I. U. Scott, "Expert agreement in evaluating the optic disc for glaucoma," *Ophthalmology*, vol. 99, pp. 215-221, 1992.
- [25] F. A. Medeiros, L. M. Zangwill, C. Bowd, R. M. Vessani, R. Susanna, Jr., and R. N. Weinreb, "Evaluation of retinal nerve fiber layer, optic nerve head, and macular thickness measurements for glaucoma detection using optical coherence tomography," *Am J Ophthalmol*, vol. 139, pp. 44-55, 2005.
- [26] H. Y. Chen and M. L. Huang, "Discrimination between normal and glaucomatous eyes using Stratus optical coherence tomography in Taiwan Chinese subjects," *Graefes Arch Clin Exp Ophthalmol*, vol. 243, pp. 894-902, Sep 2005.
- [27] J. E. Deleon-Ortega, S. N. Arthur, G. McGwin, Jr., A. Xie, B. E. Monheit, and C. A. Girkin, "Discrimination between glaucomatous and nonglaucomatous eyes using quantitative imaging devices and subjective optic nerve head assessment," *Invest Ophthalmol Vis Sci*, vol. 47, pp. 3374-80, Aug 2006.
- [28] R. Y. Abe, C. P. Gracitelli, and F. A. Medeiros, "The Use of Spectral-Domain Optical Coherence Tomography to Detect Glaucoma Progression," *Open Ophthalmol J*, vol. 9, pp. 78-88, 2015.
- [29] M. Niemeijer, M. D. Abramoff, and B. van Ginneken, "Segmentation of the optic disc, macula and vascular arch in fundus photographs," *IEEE Trans Med Imaging*, vol. 26, pp. 116-27, 2007.
- [30] J. Xu, H. Ishikawa, G. Wollstein, R. A. Bilonick, K. R. Sung, L. Kagemann, *et al.*, "Automated assessment of the optic nerve head on stereo disc photographs," *Invest Ophthalmol Vis Sci*, vol. 49, pp. 2512-7, 2008.
- [31] Y. Zheng, D. Stambolian, J. O'Brien, and J. C. Gee, "Optic disc and cup segmentation from color fundus photograph using graph cut with priors," *Med Image Comput Comput Assist Interv*, vol. 16, pp. 75-82, 2013.
- [32] E. Tay, S. K. Seah, S. P. Chan, A. T. Lim, S. J. Chew, P. J. Foster, *et al.*, "Optic disk ovality as an index of tilt and its relationship to myopia and perimetry," *Am J Ophthalmol*, vol. 139, pp. 247-52, Feb 2005.
- [33] H. Arvind, R. George, P. Raju, R. S. Ve, B. Mani, P. Kannan, *et al.*, "Neural rim characteristics of healthy South Indians: the Chennai Glaucoma Study," *Invest Ophthalmol Vis Sci*, vol. 49, pp. 3457-64, Aug 2008.

- [34] A. Garas, P. Vargha, and G. Hollo, "Diagnostic accuracy of nerve fibre layer, macular thickness and optic disc measurements made with the RTVue-100 optical coherence tomograph to detect glaucoma," *Eye*, vol. 25, pp. 57-65, Jan 2011.
- [35] S. N. Chen, J. F. Hwang, and Y. T. Chen, "Macular thickness measurements in central retinal artery occlusion by optical coherence tomography," *Retina*, vol. 31, pp. 730-7, 2011.
- [36] F. A. Folgar, E. L. Yuan, M. B. Sevilla, S. J. Chiu, S. Farsiu, E. Y. Chew, *et al.*, "Drusen Volume and Retinal Pigment Epithelium Abnormal Thinning Volume Predict 2-Year Progression of Age-Related Macular Degeneration," *Ophthalmology*, Nov 11 2015.
- [37] B. J. Antony, W. Jeong, M. D. Abramoff, J. Vance, E. H. Sohn, and M. K. Garvin, "Automated 3D Segmentation of Intraretinal Surfaces in SD-OCT Volumes in Normal and Diabetic Mice," *Transl Vis Sci Technol*, vol. 3, p. 8, Oct 2014.
- [38] B. J. Antony, M. D. Abramoff, M. M. Harper, W. Jeong, E. H. Sohn, Y. H. Kwon, *et al.*, "A combined machine-learning and graph-based framework for the segmentation of retinal surfaces in SD-OCT volumes," *Biomed Opt Express*, vol. 4, pp. 2712-28, 2013.
- [39] M. K. Garvin, K. Lee, T. L. Burns, M. D. Abramoff, M. Sonka, and Y. H. Kwon, "Reproducibility of SD-OCT-based ganglion cell-layer thickness in glaucoma using two different segmentation algorithms," *Invest Ophthalmol Vis Sci*, vol. 54, pp. 6998-7004, Oct 2013.
- [40] P. G. Sanfilippo, A. Cardini, A. W. Hewitt, J. G. Crowston, and D. A. Mackey, "Optic disc morphology--rethinking shape," *Prog Retin Eye Res*, vol. 28, pp. 227-48, Jul 2009.
- [41] B. Antony, M. D. Abramoff, L. Tang, W. D. Ramdas, J. R. Vingerling, N. M. Jansonius, *et al.*, "Automated 3-D method for the correction of axial artifacts in spectral-domain optical coherence tomography images," *Biomed Opt Express*, vol. 2, pp. 2403-16, Aug 1 2011.
- [42] T. F. Cootes, C. J. Taylor, D. Cooper, and J. Graham, "Active shape models - their training and application," *Computer Vision and Image Understanding*, vol. 61, pp. 38-59, 1995.
- [43] S. G. Mallat, "A Theory for Multiresolution Signal Decomposition: The Wavelet Representation," *IEEE Trans. Pattern Anal. Mach. Intell.*, vol. 11, pp. 674-693, 1989.
- [44] P. G. Sanfilippo, A. Cardini, I. A. Sigal, J. B. Ruddle, B. E. Chua, A. W. Hewitt, *et al.*, "A geometric morphometric assessment of the optic cup in glaucoma," *Exp Eye Res*, vol. 91, pp. 405-14, Sep 2010.
- [45] H. Zhu, A. Poostchi, S. A. Vernon, and D. P. Crabb, "Detecting abnormality in optic nerve head images using a feature extraction analysis," *Biomed Opt Express*, vol. 5, pp. 2215-30, Jul 1 2014.
- [46] H. Bogunovic, Y. H. Kwon, A. Rashid, K. Lee, D. B. Critser, M. K. Garvin, *et al.*, "Relationships of retinal structure and humphrey 24-2 visual field thresholds in patients with glaucoma," *Invest Ophthalmol Vis Sci*, vol. 56, pp. 259-71, Jan 2015.
- [47] M. K. Garvin, M. D. Abramoff, K. Lee, M. Niemeijer, M. Sonka, and Y. H. Kwon, "2-D pattern of nerve fiber bundles in glaucoma emerging from spectral-domain optical coherence tomography," *Invest Ophthalmol Vis Sci*, vol. 53, pp. 483-9, Jan 2012.
- [48] H. L. Rao, L. M. Zangwill, R. N. Weinreb, M. T. Leite, P. A. Sample, and F. A. Medeiros, "Structure-function relationship in glaucoma using spectral-domain optical coherence tomography," *Arch Ophthalmol*, vol. 129, pp. 864-71, Jul 2011.

- [49] P. G. Sanfilippo, J. L. Grimm, J. G. Flanagan, K. L. Lathrop, and I. A. Sigal, "Application of Elliptic Fourier analysis to describe the lamina cribrosa shape with age and intraocular pressure," *Exp Eye Res*, vol. 128, pp. 1-7, Nov 2014.
- [50] I. A. Sigal, B. Wang, N. G. Strouthidis, T. Akagi, and M. J. Girard, "Recent advances in OCT imaging of the lamina cribrosa," *Br J Ophthalmol*, vol. 98 Suppl 2, pp. ii34-9, Jul 2014.
- [51] K. Omodaka, T. Horii, S. Takahashi, T. Kikawa, A. Matsumoto, Y. Shiga, *et al.*, "3D evaluation of the lamina cribrosa with swept-source optical coherence tomography in normal tension glaucoma," *PLoS One*, vol. 10, p. e0122347, 2015.
- [52] F. J. Stone EM, Alward WL Nguyen TD Polansky JR Sunden SL Nishimura D Clark AF Nystuen A Nichols BE Mackey DA Ritch R Kalenak JW Craven ER Sheffield VC, "Identification of a gene that causes primary open angle glaucoma," *Science*, pp. 275(5300): 668-70, 1997.
- [53] J. H. Fingert, E. Heon, J. M. Liebmann, T. Yamamoto, J. E. Craig, J. Rait, *et al.*, "Analysis of myocilin mutations in 1703 glaucoma patients from five different populations," *Hum Mol Genet*, vol. 8, pp. 899-905, 1999.
- [54] T. Rezaie, A. Child, R. Hitchings, G. Brice, L. Miller, M. Coca-Prados, *et al.*, "Adult-onset primary open-angle glaucoma caused by mutations in optineurin," *Science*, vol. 295, pp. 1077-9, 2002.
- [55] J. M. Teikari, P. J. Airaksinen, J. Kaprio, and M. Koskenvuo, "Primary open-angle glaucoma in 2 monozygotic twin pairs," *Acta Ophthalmol (Copenh)*, vol. 65, pp. 607-11, Oct 1987.
- [56] A. L. Crombie and J. F. Cullen, "Hereditary Glaucoma Occurrence in Five Generations of an Edinburgh Family," *Br J Ophthalmol*, vol. 48, pp. 143-7, Mar 1964.
- [57] A. W. Hewitt, J. E. Craig, and D. A. Mackey, "Complex genetics of complex traits: the case of primary open-angle glaucoma," *Clin Experiment Ophthalmol*, vol. 34, pp. 472-84, Jul 2006.
- [58] R. C. Wolfs, C. C. Klaver, R. S. Ramrattan, C. M. van Duijn, A. Hofman, and P. T. de Jong, "Genetic risk of primary open-angle glaucoma. Population-based familial aggregation study," *Arch Ophthalmol*, vol. 116, pp. 1640-5, Dec 1998.
- [59] W. D. Ramdas, L. M. van Koolwijk, A. J. Cree, A. C. Janssens, N. Amin, P. T. de Jong, *et al.*, "Clinical implications of old and new genes for open-angle glaucoma," *Ophthalmology*, vol. 118, pp. 2389-97, Dec 2011.
- [60] J. H. Fingert, "Primary open-angle glaucoma genes," *Eye (Lond)*, vol. 25, pp. 587-95, May 2011.
- [61] J. H. Fingert, E. M. Stone, V. C. Sheffield, and W. L. Alward, "Myocilin glaucoma," *Surv Ophthalmol*, vol. 47, pp. 547-61, Nov-Dec 2002.
- [62] T. Aung, N. D. Ebenezer, G. Brice, A. H. Child, Q. Prescott, O. J. Lehmann, *et al.*, "Prevalence of optineurin sequence variants in adult primary open angle glaucoma: implications for diagnostic testing," *J Med Genet*, vol. 40, p. e101, Aug 2003.
- [63] S. Monemi, G. Spaeth, A. DaSilva, S. Popinchalk, E. Ilitchev, J. Liebmann, *et al.*, "Identification of a novel adult-onset primary open-angle glaucoma (POAG) gene on 5q22.1," *Hum Mol Genet*, vol. 14, pp. 725-33, Mar 15 2005.
- [64] J. H. Fingert, W. L. Alward, Y. H. Kwon, S. P. Shankar, J. L. Andorf, D. A. Mackey, *et al.*, "No association between variations in the WDR36 gene and primary open-angle glaucoma," *Arch Ophthalmol*, vol. 125, pp. 434-6, Mar 2007.
- [65] A. W. Hewitt, D. P. Dimasi, D. A. Mackey, and J. E. Craig, "A Glaucoma Case-control Study of the WDR36 Gene D658G sequence variant," *Am J Ophthalmol*, vol. 142, pp. 324-5, Aug 2006.
- [66] J. H. Fingert, A. L. Robin, J. L. Stone, B. R. Roos, L. K. Davis, T. E. Scheetz, *et al.*, "Copy number variations on chromosome 12q14 in patients with normal tension glaucoma," *Hum Mol Genet*, vol. 20, pp. 2482-94, Jun 15 2011.

- [67] G. Thorleifsson, G. B. Walters, A. W. Hewitt, G. Masson, A. Helgason, A. DeWan, *et al.*, "Common variants near CAV1 and CAV2 are associated with primary open-angle glaucoma," *Nat Genet*, vol. 42, pp. 906-9, Oct 2010.
- [68] J. L. Wiggs, J. H. Kang, B. L. Yaspan, D. B. Mirel, C. Laurie, A. Crenshaw, *et al.*, "Common variants near CAV1 and CAV2 are associated with primary open-angle glaucoma in Caucasians from the USA," *Hum Mol Genet*, vol. 20, pp. 4707-13, Dec 1 2011.
- [69] K. P. Burdon, P. Mitchell, A. Lee, P. R. Healey, A. J. White, E. Rohtchina, *et al.*, "Association of open-angle glaucoma loci with incident glaucoma in the Blue Mountains Eye Study," *Am J Ophthalmol*, vol. 159, pp. 31-6 e1, Jan 2015.
- [70] S. Writing Committee for the Normal Tension Glaucoma Genetic Study Group of Japan Glaucoma, A. Meguro, H. Inoko, M. Ota, N. Mizuki, and S. Bahram, "Genome-wide association study of normal tension glaucoma: common variants in SRBD1 and ELOVL5 contribute to disease susceptibility," *Ophthalmology*, vol. 117, pp. 1331-8 e5, Jul 2010.
- [71] K. P. Burdon, S. Macgregor, A. W. Hewitt, S. Sharma, G. Chidlow, R. A. Mills, *et al.*, "Genome-wide association study identifies susceptibility loci for open angle glaucoma at TMCO1 and CDKN2B-AS1," *Nat Genet*, vol. 43, pp. 574-8, Jun 2011.
- [72] C. J. Willer, S. Sanna, A. U. Jackson, A. Scuteri, L. L. Bonnycastle, R. Clarke, *et al.*, "Newly identified loci that influence lipid concentrations and risk of coronary artery disease," *Nat Genet*, vol. 40, pp. 161-9, Feb 2008.
- [73] S. Kathiresan, C. J. Willer, G. M. Peloso, S. Demissie, K. Musunuru, E. E. Schadt, *et al.*, "Common variants at 30 loci contribute to polygenic dyslipidemia," *Nat Genet*, vol. 41, pp. 56-65, Jan 2009.
- [74] B. D. Mitchell, S. A. Cole, R. L. Bauer, S. J. Iturria, E. A. Rodriguez, J. Blangero, *et al.*, "Genes influencing variation in serum osteocalcin concentrations are linked to markers on chromosomes 16q and 20q," *J Clin Endocrinol Metab*, vol. 85, pp. 1362-6, Apr 2000.
- [75] D. C. Glahn, J. E. Curran, A. M. Winkler, M. A. Carless, J. W. Kent, Jr., J. C. Charlesworth, *et al.*, "High dimensional endophenotype ranking in the search for major depression risk genes," *Biol Psychiatry*, vol. 71, pp. 6-14, Jan 1 2012.
- [76] S. Macgregor, A. W. Hewitt, P. G. Hysi, J. B. Ruddle, S. E. Medland, A. K. Henders, *et al.*, "Genome-wide association identifies ATOH7 as a major gene determining human optic disc size," *Hum Mol Genet*, vol. 19, pp. 2716-24, Jul 1 2010.
- [77] B. J. Fan, D. Y. Wang, L. R. Pasquale, J. L. Haines, and J. L. Wiggs, "Genetic variants associated with optic nerve vertical cup-to-disc ratio are risk factors for primary open angle glaucoma in a US Caucasian population," *Invest Ophthalmol Vis Sci*, vol. 52, pp. 1788-92, Mar 2011.
- [78] J. Gibson, H. Griffiths, G. De Salvo, M. Cole, A. Jacob, A. Macleod, *et al.*, "Genome-wide association study of primary open angle glaucoma risk and quantitative traits," *Mol Vis*, vol. 18, pp. 1083-92, 2012.
- [79] L. R. Pasquale, S. J. Loomis, J. H. Kang, B. L. Yaspan, W. Abdrabou, D. L. Budenz, *et al.*, "CDKN2B-AS1 genotype-glaucoma feature correlations in primary open-angle glaucoma patients from the United States," *Am J Ophthalmol*, vol. 155, pp. 342-353 e5, Feb 2013.
- [80] H. Springelkamp, R. Hohn, A. Mishra, P. G. Hysi, C. C. Khor, S. J. Loomis, *et al.*, "Meta-analysis of genome-wide association studies identifies novel loci that influence cupping and the glaucomatous process," *Nat Commun*, vol. 5, p. 4883, 2014.
- [81] P. G. Hysi, C. Y. Cheng, H. Springelkamp, S. Macgregor, J. N. Bailey, R. Wojciechowski, *et al.*, "Genome-wide analysis of multi-ancestry cohorts



- identifies new loci influencing intraocular pressure and susceptibility to glaucoma," *Nat Genet*, vol. 46, pp. 1126-30, Oct 2014.
- [82] F. Chen, A. P. Klein, B. E. Klein, K. E. Lee, B. Truitt, R. Klein, *et al.*, "Exome array analysis identifies CAV1/CAV2 as a susceptibility locus for intraocular pressure," *Invest Ophthalmol Vis Sci*, vol. 56, pp. 544-51, Jan 2015.
- [83] A. B. Ozel, S. E. Moroi, D. M. Reed, M. Nika, C. M. Schmidt, S. Akbari, *et al.*, "Genome-wide association study and meta-analysis of intraocular pressure," *Hum Genet*, vol. 133, pp. 41-57, Jan 2014.
- [84] X. Gao, W. J. Gauderman, Y. Liu, P. Marjoram, M. Torres, T. Haritunians, *et al.*, "A genome-wide association study of central corneal thickness in Latinos," *Invest Ophthalmol Vis Sci*, vol. 54, pp. 2435-43, Apr 2013.
- [85] Y. Lu, D. P. Dimasi, P. G. Hysi, A. W. Hewitt, K. P. Burdon, T. Toh, *et al.*, "Common genetic variants near the Brittle Cornea Syndrome locus ZNF469 influence the blinding disease risk factor central corneal thickness," *PLoS Genet*, vol. 6, p. e1000947, May 2010.
- [86] Y. Lu, V. Vitart, K. P. Burdon, C. C. Khor, Y. Bykhovskaya, A. Mirshahi, *et al.*, "Genome-wide association analyses identify multiple loci associated with central corneal thickness and keratoconus," *Nat Genet*, vol. 45, pp. 155-63, Feb 2013.
- [87] H. Springelkamp, A. Mishra, P. G. Hysi, P. Gharahkhani, R. Hohn, C. C. Khor, *et al.*, "Meta-analysis of Genome-Wide Association Studies Identifies Novel Loci Associated With Optic Disc Morphology," *Genet Epidemiol*, vol. 39, pp. 207-16, Mar 2015.
- [88] F. Carbonaro, T. Andrew, D. A. Mackey, T. D. Spector, and C. J. Hammond, "Heritability of intraocular pressure: a classical twin study," *Br J Ophthalmol*, vol. 92, pp. 1125-8, Aug 2008.
- [89] T. C. Chang, N. G. Congdon, R. Wojciechowski, B. Munoz, D. Gilbert, P. Chen, *et al.*, "Determinants and heritability of intraocular pressure and cup-to-disc ratio in a defined older population," *Ophthalmology*, vol. 112, pp. 1186-91, Jul 2005.
- [90] E. E. Freeman, M. H. Roy-Gagnon, D. Descovich, H. Masse, and M. R. Lesk, "The heritability of glaucoma-related traits corneal hysteresis, central corneal thickness, intraocular pressure, and choroidal blood flow pulsatility," *PLoS One*, vol. 8, p. e55573, 2013.
- [91] M. D. Abramoff, M. Garvin, and M. Sonka, "Retinal Imaging and Image Analysis," *IEEE Rev Biomed Engin*, pp. 169-208, 2010.
- [92] (2005, Oct 1, 2015). *MESSIDOR: Methods to evaluate segmentation and indexing techniques in the eld of retinal ophthalmology*.
- [93] M. Niemeijer, B. van Ginneken, M. Sonka, and M. D. Abramoff, "Automated classification of exudates, cottonwool spots and drusen from retinal color images for diabetic retinopathy screening," *Investigative Ophthalmology & Visual Science*, vol. 46, pp. -, 2005.
- [94] M. Niemeijer, B. van Ginneken, S. R. Russell, M. S. Suttorp-Schulten, and M. D. Abramoff, "Automated detection and differentiation of drusen, exudates, and cotton-wool spots in digital color fundus photographs for diabetic retinopathy diagnosis," *Invest Ophthalmol Vis Sci*, vol. 48, pp. 2260-7, 2007.
- [95] I. S. Clara, N. Meindert, K. Thessa, D. A. Michael, and G. Bram van, "Active learning approach for detection of hard exudates, cotton wool spots, and drusen in retinal images," ed, 2009, p. 72601I.
- [96] G. Quellec, S. R. Russell, J. M. Seddon, R. Reynolds, T. Scheetz, V. B. Mahajan, *et al.*, "Automated discovery and quantification of image-based complex phenotypes: a twin study of drusen phenotypes in age-related macular degeneration," *Investigative Ophthalmology & Visual Science*, vol. 52, pp. 9195-206, 2011.
- [97] M. D. Abramoff, B. Van Ginneken, M. S. A. Suttorp, S. R. Russell, and M. Niemeijer, "Improved Computer Aided Detection of Diabetic Retinopathy

- Evaluated on 10,000 Screening Exams," *ARVO Meeting Abstracts*, vol. 49, p. 2735, 2008.
- [98] Z. Liang, D. W. Wong, J. Liu, K. L. Chan, and T. Y. Wong, "Towards automatic detection of age-related macular degeneration in retinal fundus images," *Conf Proc IEEE Eng Med Biol Soc*, vol. 2010, pp. 4100-3, 2010.
- [99] T. Y. Wong, N. Cheung, F. M. Islam, R. Klein, M. H. Criqui, M. F. Cotch, *et al.*, "Relation of retinopathy to coronary artery calcification: the multi-ethnic study of atherosclerosis," *Am J Epidemiol*, vol. 167, pp. 51-8, Jan 1 2008.
- [100] N. Cheung, G. Liew, R. I. Lindley, E. Y. Liu, J. J. Wang, P. Hand, *et al.*, "Retinal fractals and acute lacunar stroke," *Ann Neurol*, vol. 68, pp. 107-11, Jul 2010.
- [101] T. S. Yoo, M. J. Ackerman, W. E. Lorensen, W. Schroeder, V. Chalana, S. Aylward, *et al.*, "Engineering and algorithm design for an image processing Api: a technical report on ITK--the Insight Toolkit," *Stud Health Technol Inform*, vol. 85, pp. 586-92, 2002.
- [102] M. D. Abramoff, W. L. Alward, E. C. Greenlee, L. Shuba, C. Y. Kim, J. H. Fingert, *et al.*, "Automated segmentation of the optic disc from stereo color photographs using physiologically plausible features," *Invest Ophthalmol Vis Sci*, vol. 48, pp. 1665-73, 2007.
- [103] M. Foracchia, E. Grisan, and A. Ruggeri, "Detection of optic disc in retinal images by means of a geometrical model of vessel structure," *IEEE Trans Med Imaging*, vol. 23, pp. 1189-1195, 2004.
- [104] K. W. Tobin, E. Chaum, V. P. Govindasamy, and T. P. Karnowski, "Detection of anatomic structures in human retinal imagery," *IEEE Trans Med Imaging*, vol. 26, pp. 1729-39, 2007.
- [105] A. R. Youssif, A. Z. Ghalwash, and A. R. Ghoneim, "Optic disc detection from normalized digital fundus images by means of a vessels' direction matched filter," *IEEE Trans Med Imaging*, vol. 27, pp. 11-8, Jan 2008.
- [106] S. Lu, "Accurate and efficient optic disc detection and segmentation by a circular transformation," *IEEE Trans Med Imaging*, vol. 30, pp. 2126-33, Dec 2011.
- [107] M. Niemeijer, M. D. Abramoff, and B. van Ginneken, "Fast detection of the optic disc and fovea in color fundus photographs," *Med Image Anal*, vol. 13, pp. 859-70, 2009.
- [108] J. Illingworth and J. Kittler, "The adaptive hough transform," *IEEE Trans Pattern Anal Mach Intell*, vol. 9, pp. 690-8, May 1987.
- [109] I. T. Jolliffe, *Principal Component Analysis*, 2nd ed. ed. vol. XXIX 487. NY: Springer, 2002.
- [110] D. Scharstein and R. Szeliski, "A Taxonomy and Evaluation of Dense Two-Frame Stereo Correspondence Algorithms," *ICJV*, vol. 47, pp. 7-42, 2002.
- [111] M. Z. Brown, D. Burschka, and G. D. Hager, "Advances in computational stereo," *Ieee Transactions on Pattern Analysis and Machine Intelligence*, vol. 25, pp. 993-1008, Aug 2003.
- [112] D. M. Poggio and T., "Cooperative Computation of Stereo Disparity," *Science*, pp. 194: 209-236, 1976.
- [113] S. T. Barnard and W. B. Thompson, "Disparity analysis of images," *IEEE Trans Patt Anal Mach Intell*, vol. 2, pp. 333-340, 1980.
- [114] D. Scharstein and R. Szeliski, "A Taxonomy and Evaluation of Dense Two-Frame Stereo Correspondence Algorithms," *International Journal of Computer Vision*, vol. 47, pp. 7-42, 2002/04/01 2002.
- [115] C. L. Zitnick and T. Kanade, "A cooperative algorithm for stereo matching and occlusion detection," *Ieee Transactions on Pattern Analysis and Machine Intelligence*, vol. 22, pp. 675-684, Jul 2000.
- [116] Y. Zhan, Y. Gu, K. Huang, C. Zhang, and K. Hu, "Accurate Image-guided Stereo Matching with Efficient Matching Cost and Disparity Refinement," *Circuits and Systems for Video Technology, IEEE Transactions on*, vol. PP, pp. 1-1, 2015.

- [117] D. T. Vu, B. Chidester, H. Yang, M. N. Do, and J. Lu, "Efficient hybrid tree-based stereo matching with applications to postcapture image refocusing," *IEEE Trans Image Process*, vol. 23, pp. 3428-42, Aug 2014.
- [118] P. Favaro, S. Soatto, M. Burger, and S. J. Osher, "Shape from defocus via diffusion," *IEEE Trans Pattern Anal Mach Intell*, vol. 30, pp. 518-31, Mar 2008.
- [119] M. W. Maimone and S. A. Shafer, "Modeling foreshortening in stereo vision using local spatial frequency," *Iros '95 - 1995 Ieee/Rsj International Conference on Intelligent Robots and Systems: Human Robot Interaction and Cooperative Robots, Proceedings, Vol 1*, pp. 519-524, 1995.
- [120] D. Scharstein and R. Szeliski, "High-Accuracy Stereo Depth Maps Using Structured Light," pp. 195-202.
- [121] L. Tang, M. K. Garvin, K. Lee, W. L. Alward, Y. H. Kwon, and M. D. Abramoff, "Robust multiscale stereo matching from fundus images with radiometric differences," *IEEE Trans Pattern Anal Mach Intell*, vol. 33, pp. 2245-58, Nov 2011.
- [122] T. Lindeberg, "Scale-space theory: A basic tool for analysing structures at different scales," *Journal of Applied Statistics*, vol. 21, pp. 224-270, 1994.
- [123] K. Lee, M. Niemeijer, M. K. Garvin, Y. H. Kwon, M. Sonka, and M. D. Abramoff, "Segmentation of the optic disc in 3-D OCT scans of the optic nerve head," *IEEE Trans Med Imaging*, vol. 29, pp. 159-68, 2010.
- [124] L. M. Zangwill, R. N. Weinreb, C. C. Berry, A. R. Smith, K. A. Dirkes, A. L. Coleman, *et al.*, "Racial differences in optic disc topography: baseline results from the confocal scanning laser ophthalmoscopy ancillary study to the ocular hypertension treatment study," *Arch Ophthalmol*, vol. 122, pp. 22-8, Jan 2004.
- [125] B. Polaczek-Krupa and I. Grabska-Liberek, "Evaluation of the significance of some diagnostic parameters in making an early diagnose of primary open-angle glaucoma," *Med Sci Monit*, vol. 18, pp. CR456-60, Jul 2012.
- [126] J. B. Jonas, A. Bergua, P. Schmitz-Valckenberg, K. I. Papastathopoulos, and W. M. Budde, "Ranking of optic disc variables for detection of glaucomatous optic nerve damage," *Invest Ophthalmol Vis Sci*, vol. 41, pp. 1764-73, Jun 2000.
- [127] M. Christopher, M. D. Abramoff, L. Tang, M. O. Gordon, M. A. Kass, D. L. Budenz, *et al.*, "Stereo Photo Measured ONH Shape Predicts Development of POAG in Subjects With Ocular Hypertension," *Invest Ophthalmol Vis Sci*, vol. 56, pp. 4470-9, Jul 2015.
- [128] A. M. Martinez and A. C. Kak, "PCA versus LDA," *Pattern Analysis and Machine Intelligence, IEEE Transactions on*, vol. 23, pp. 228-233, 2001.
- [129] G. Ocular Hypertension Treatment Study, G. European Glaucoma Prevention Study, M. O. Gordon, V. Torri, S. Miglior, J. A. Beiser, *et al.*, "Validated prediction model for the development of primary open-angle glaucoma in individuals with ocular hypertension," *Ophthalmology*, vol. 114, pp. 10-9, Jan 2007.
- [130] G. Ocular Hypertension Treatment Study and G. the European Glaucoma Prevention Study, "The accuracy and clinical application of predictive models for primary open-angle glaucoma in ocular hypertensive individuals," *Ophthalmology*, vol. 115, pp. 2030-6, Nov 2008.
- [131] S. S. Cross, "Kappa statistics as indicators of quality assurance in histopathology and cytopathology," *J Clin Pathol*, vol. 49, pp. 597-9, 1996.
- [132] Y. Takwoingi, A. P. Botello, J. M. Burr, A. Azuara-Blanco, D. F. Garway-Heath, H. G. Lemij, *et al.*, "External validation of the OHTS-EGPS model for predicting the 5-year risk of open-angle glaucoma in ocular hypertensives," *Br J Ophthalmol*, vol. 98, pp. 309-14, Mar 2014.
- [133] J. C. Mwanza, M. K. Durbin, D. L. Budenz, F. E. Sayyad, R. T. Chang, A. Neelakantan, *et al.*, "Glaucoma diagnostic accuracy of ganglion cell-inner

- plexiform layer thickness: comparison with nerve fiber layer and optic nerve head," *Ophthalmology*, vol. 119, pp. 1151-8, Jun 2012.
- [134] R. Lisboa, M. T. Leite, L. M. Zangwill, A. Tafreshi, R. N. Weinreb, and F. A. Medeiros, "Diagnosing preperimetric glaucoma with spectral domain optical coherence tomography," *Ophthalmology*, vol. 119, pp. 2261-9, Nov 2012.
- [135] P. Sibony, M. J. Kupersmith, and F. J. Rohlf, "Shape analysis of the peripapillary RPE layer in papilledema and ischemic optic neuropathy," *Invest Ophthalmol Vis Sci*, vol. 52, pp. 7987-95, 2011.
- [136] P. Sibony, M. Strachovsky, R. Honkanen, and M. J. Kupersmith, "Optical coherence tomography shape analysis of the peripapillary retinal pigment epithelium layer in presumed optic nerve sheath meningiomas," *J Neuroophthalmol*, vol. 34, pp. 130-6, Jun 2014.
- [137] D. F. Garway-Heath and R. A. Hitchings, "Quantitative evaluation of the optic nerve head in early glaucoma," *Br J Ophthalmol*, vol. 82, pp. 352-61, Apr 1998.
- [138] J. B. Jonas, M. C. Fernandez, and J. Sturmer, "Pattern of glaucomatous neuroretinal rim loss," *Ophthalmology*, vol. 100, pp. 63-8, Jan 1993.
- [139] N. G. Strouthidis, S. K. Gardiner, C. Sinapis, C. F. Burgoyne, and D. F. Garway-Heath, "The spatial pattern of neuroretinal rim loss in ocular hypertension," *Invest Ophthalmol Vis Sci*, vol. 50, pp. 3737-42, Aug 2009.
- [140] M. Christopher, L. Tang, J. H. Fingert, T. E. Scheetz, and M. D. Abramoff, "Automated discovery of structural features of the optic nerve head on the basis of image and genetic data," *SPIE Med Imaging*, vol. 9035, 2014.
- [141] E. M. Stone, J. H. Fingert, W. L. Alward, T. D. Nguyen, J. R. Polansky, S. L. Sunden, *et al.*, "Identification of a gene that causes primary open angle glaucoma," *Science*, vol. 275, pp. 668-70, 1997.
- [142] M. Takamoto and M. Araie, "Genetics of primary open angle glaucoma," *Jpn J Ophthalmol*, vol. 58, pp. 1-15, Jan 2014.
- [143] J. L. Wiggs, J. H. Kang, B. L. Yaspan, D. B. Mirel, C. Laurie, A. Crenshaw, *et al.*, "Common variants near CAV1 and CAV2 are associated with primary open-angle glaucoma in Caucasians from the USA," *Hum Mol Genet*, vol. 20, pp. 4707-13, Dec 1 2011.
- [144] W. D. Ramdas, L. M. van Koolwijk, H. G. Lemij, F. Pasutto, A. J. Cree, G. Thorleifsson, *et al.*, "Common genetic variants associated with open-angle glaucoma," *Hum Mol Genet*, vol. 20, pp. 2464-71, Jun 15 2011.
- [145] M. Leboyer, F. Bellivier, M. Nosten-Bertrand, R. Jouvent, D. Pauls, and J. Mallet, "Psychiatric genetics: search for phenotypes," *Trends Neurosci*, vol. 21, pp. 102-5, Mar 1998.
- [146] B. K. Cornes, C. C. Khor, M. E. Nongpiur, L. Xu, W. T. Tay, Y. Zheng, *et al.*, "Identification of four novel variants that influence central corneal thickness in multi-ethnic Asian populations," *Hum Mol Genet*, vol. 21, pp. 437-45, Jan 15 2012.
- [147] L. M. van Koolwijk, W. D. Ramdas, M. K. Ikram, N. M. Jansonius, F. Pasutto, P. G. Hysi, *et al.*, "Common genetic determinants of intraocular pressure and primary open-angle glaucoma," *PLoS Genet*, vol. 8, p. e1002611, 2012.
- [148] C. C. Khor, W. D. Ramdas, E. N. Vithana, B. K. Cornes, X. Sim, W. T. Tay, *et al.*, "Genome-wide association studies in Asians confirm the involvement of ATOH7 and TGFBR3, and further identify CARD10 as a novel locus influencing optic disc area," *Hum Mol Genet*, vol. 20, pp. 1864-72, May 1 2011.
- [149] L. Tang, T. E. Scheetz, D. A. Mackey, A. W. Hewitt, J. H. Fingert, Y. H. Kwon, *et al.*, "Automated quantification of inherited phenotypes from color images: a twin study of the variability of optic nerve head shape," *Invest Ophthalmol Vis Sci*, vol. 51, pp. 5870-7, Nov 2010.

- [150] A. W. Hewitt, J. E. Craig, and D. A. Mackey, "Complex genetics of complex traits: the case of primary open-angle glaucoma," *Clinical & experimental ophthalmology*, vol. 34, pp. 472-84, Jul 2006.
- [151] S. Turner, L. L. Armstrong, Y. Bradford, C. S. Carlson, D. C. Crawford, A. T. Crenshaw, *et al.*, "Quality control procedures for genome-wide association studies," *Curr Protoc Hum Genet*, vol. Chapter 1, p. Unit1 19, Jan 2011.
- [152] S. Purcell, B. Neale, K. Todd-Brown, L. Thomas, M. A. Ferreira, D. Bender, *et al.*, "PLINK: a tool set for whole-genome association and population-based linkage analyses," *Am J Hum Genet*, vol. 81, pp. 559-75, Sep 2007.
- [153] Y. Benjamini, D. Drai, G. Elmer, N. Kafkafi, and I. Golani, "Controlling the false discovery rate in behavior genetics research," *Behav Brain Res*, vol. 125, pp. 279-84, Nov 1 2001.
- [154] Y. Benjamini and D. Yekutieli, "Quantitative trait Loci analysis using the false discovery rate," *Genetics*, vol. 171, pp. 783-90, Oct 2005.
- [155] P. Deloukas, S. Kanoni, C. Willenborg, M. Farrall, T. L. Assimes, J. R. Thompson, *et al.*, "Large-scale association analysis identifies new risk loci for coronary artery disease," *Nat Genet*, vol. 45, pp. 25-33, Jan 2013.
- [156] J. D. Storey and R. Tibshirani, "Statistical significance for genomewide studies," *Proc Natl Acad Sci U S A*, vol. 100, pp. 9440-5, Aug 5 2003.
- [157] M. Sonka and J. M. Fitzpatrick, *Handbook of Medical Imaging - Volume 2, Medical Image Processing and Analysis*. Wellingham, WA: The International Society for Optical Engineering Press, 2000.
- [158] A. A. Goshtasby, *2-D and 3-D Image Registration: for Medical, Remote Sensing, and Industrial Applications*: Wiley-Interscience, 2005.
- [159] P. Viola and W. M. Wells, "Alignment by maximization of mutual information," *International Journal of Computer Vision*, vol. 24, pp. 137-154, Sep 1997.
- [160] W. Cleveland and E. Grosse, "Computational methods for local regression," *Statistics and Computing*, vol. 1, pp. 47-62, 1991/09/01 1991.
- [161] T. Giorgino, "Computing and Visualizing Dynamic Time Warping Alignments in R: The dtw Package," *2009*, vol. 31, p. 24, 2009-08-14 2009.
- [162] T. F. Cox and M. A. A. Cox, *Multidimensional scaling*, 2nd ed. Boca Raton: Chapman & Hall/CRC, 2001.
- [163] M. S. Rosenberg, *Sequence Alignment: Methods, Models, Concepts, and Strategies*: University of California Press, 2009.
- [164] Y. Yin and P. Shang, "Modified multidimensional scaling approach to analyze financial markets," *Chaos*, vol. 24, p. 022102, Jun 2014.